UNIVERSIDADE FEDERAL DO PARANÁ

HUGO TAMOTO

IMPACTOS DE PROCESSOS DIAGENÉTICOS NA AVALIAÇÃO DE FORMAÇÃO EM RESERVATÓRIOS CARBONÁTICOS DA FORMAÇÃO BARRA VELHA, DO PRÉ-SAL.

CURITIBA

2022

HUGO TAMOTO

IMPACTOS DE PROCESSOS DIAGENÉTICOS NA AVALIAÇÃO DE FORMAÇÃO EM RESERVATÓRIOS CARBONÁTICOS DA FORMAÇÃO BARRA VELHA, DO PRÉ-SAL.

IMPACTS OF DIAGENETIC PROCESSES IN FORMATION EVALUATION OF THE PRE-SALT CARBONATES RESERVOIRS OF BARRA VELHA FORMATION.

Dissertação apresentada ao curso de Pós-Graduação em Geologia, Setor de Ciências da Terra, Universidade Federal do Paraná, como requisito parcial à obtenção do título de Mestre em Geologia.

Orientadora: Profa. Dra. Anelize Manuela Bahniuk Rumbelsperger

Coorientador. Dr. André Luiz Silva Pestilho

CURITIBA

2022

MINISTÉRIO DA EDUCAÇÃO
SETOR DE CIENCIAS DA TERRA
UNIVERSIDADE FEDERAL DO PARANÁ
PRÓ-REITORIA DE PESQUISA E PÓS-GRADUAÇÃO
PROGRAMA DE PÓS-GRADUAÇÃO GEOLOGIA -
40001016028P5

TERMO DE APROVAÇÃO

Os membros da Banca Examinadora designada pelo Colegiado do Programa de Pós-Graduação GEOLOGIA da Universidade Federal do Paraná foram convocados para realizar a arguição da Dissertação de Mestrado de **HUGO TAMOTO** intitulada: **IMPACTOS DE PROCESSOS DIAGENÉTICOS NA AVALIAÇÃO DE FORMAÇÃO BARRA VELHA EM RESERVATÓRIO CARBONÁTICO DO PRÉ-SAL**, sob orientação da Profa. Dra. ANELIZE MANUELA BAHNIUK RUMBELSPERGER, que após terem inquirido o aluno e realizada a avaliação do trabalho, são de parecer pela sua APROVAÇÃO no rito de defesa.

A outorga do título de mestre está sujeita à homologação pelo colegiado, ao atendimento de todas as indicações e correções solicitadas pela banca e ao pleno atendimento das demandas regimentais do Programa de Pós-Graduação.

CURITIBA, 01 de Setembro de 2022.

Assinatura Eletrônica
05/09/2022 17:47:09.0
ANELIZE MANUELA BAHNIUK RUMBELSPERGER
Presidente da Banca Examinadora

Assinatura Eletrônica
02/09/2022 09:53:10.0
ALMÉRIO BARROS FRANÇA
Avaliador Interno (UNIVERSIDADE FEDERAL DO PARANÁ)

Assinatura Eletrônica
02/09/2022 10:56:46.0
FILIPE GIOVANINI VAREJÃO
Avaliador Externo (UNIVERSIDADE FEDERAL DE OURO PRETO)

DEPARTAMENTO DE GEOLOGIA-CENTRO POLITÉCNICO-UFPR - CURITIBA - Paraná - Brasil
CEP 81531-990 - Tel: (41) 3361-3365 - E-mail: posgeol@ufpr.br
Documento assinado eletronicamente de acordo com o disposto na legislação federal Decreto 8539 de 08 de outubro de 2015.
Gerado e autenticado pelo SIGA-UFPR, com a seguinte identificação única: 219580
**Para autenticar este documento/assinatura, acesse https://www.prppg.ufpr.br/siga/visitante/autenticacaoassinaturas.jsp
e insira o codigo 219580**

D E C L A R A Ç Ã O

Declaramos para os devidos fins que **HUGO TAMOTO** realizou sua defesa de dissertação intitulada "**IMPACTOS DE PROCESSOS DIAGENÉTICOS NA AVALIAÇÃO DE FORMAÇÃO BARRA VELHA EM RESERVATÓRIOS CARBONÁTICOS DO PRÉ-SAL**" em 01 de setembro de 2022, no Programa de Pós-Graduação em Geologia da Universidade Federal do Paraná, área Geologia Exploratória, nível Mestrado, e que por sugestão da banca examinadora, o título foi alterado para "**IMPACTOS DE PROCESSOS DIAGENÉTICOS NA AVALIAÇÃO DE FORMAÇÃO DE RESERVATÓRIOS CARBONÁTICOS DA FORMAÇÃO BARRA-VELHA, DO PRÉ-SAL**".

Curitiba, 10 de outubro de 2022.

Carlos Conforti Ferreira Guedes
Coordenador do Programa
Pós-Graduação em Geologia

Dedico esta dissertação ao meu bebê Ravi.

AGRADECIMENTOS

RESUMO

O Pré-Sal brasileiro, localizado na Bacia de Santos constitui uma das mais importantes províncias de hidrocarbonetos do mundo. Os hidrocarbonetos estão armazenados em reservatórios carbonáticos, responsáveis por aproximadamente 75% da produção brasileira de petróleo. Apesar das boas qualidades petrofísicas do reservatório do Pré-Sal (atingindo porosidades > 15 % e permeabilidade > 100 mD), ainda existem desafios relacionados à falta de entendimento sobre os controles petrofísicos resultantes de uma complexa história deposicional e diagenética. A fim de melhor compreender essa problemática, esse estudo provê uma avaliação petrofísica geral dos reservatórios carbonáticos da Formação Barra Velha no campo de Sapinhoá, localizado na Bacia de Santos, utilizando um extenso conjunto de dados, que incluem informações de perfilagem de poços, petrofísica e difração de raios X. Os resultados permitiram a identificação de heterogeneidades de fácies, distribuição petrofísica variada, e identificação de cinco unidades de fluxo. De modo geral, os melhores intervalos de porosidade e permeabilidade encontram-se nos poços localizados no alto estrutural e compreendem as unidades de fluxo 4 e 5, compostas principalmente de litofácies *Shrubs* e *grainstones*. Além disso, a unidade de fluxo 3, composta por de *Shrubs*, esferulititos, *grainstones*, *packstones* e laminitos, apresenta características intermediárias de porosidade e permeabilidade, sendo encontrada em todos os poços. Por fim, dentre todas as unidades, as unidades de fluxo 1 e 2, compostas por todas as fácies apresentaram valores de porosidade e permeabilidade mais baixas características petrofísicas mais baixas e são encontradas principalmente nos poços fora do alto estrutural. Por fim, os resultados indicam que processos diagenéticos, como a dissolução de minerais argilosos e a dolomitização, são elementos notáveis que comumente aprimoram as propriedades petrofísicas; e a silicificação pervasiva diminui a qualidade petrofísica do reservatório. Essas características são frequentemente encontradas nos poços localizados no alto estrutural, e nos poços localizados nos flancos do alto estrutural do campo de Sapinhoá.

Palavras-chave: Pré-Sal. Petrofísica de carbonatos. Avaliação de formação. Bacia de Santos.

ABSTRACT

The Pre–Salt succession located at the marginal basins of Brazil are one among the most important hydrocarbon reservoirs found worldwide. These reservoirs are responsible for approximately 75% of the Brazilian offshore oil production. Despite the excellent reservoir qualities (reaching porosities > 15 % and permeability > 100 mD) found in the Pre–Salt reservoirs, there are still challenges related to the lack of understanding on the petrophysical controls. This situation is resultant from a complex depositional and diagenetic history of the carbonate rocks. To address such problems, an overall petrophysical evaluation of the carbonate section of the Aptian Barra Velha Formation in the Sapinhoá field, Santos Basin is provided. This way done by using an extensive dataset of well–logging, petrophysics, and X–ray diffraction. The results allowed the identification of facies heterogeneities and variated petrophysical distribution, which characterizes five hydraulic flow units. Overall, the best petrophysical intervals (i.e., highest porosity and permeability) are found in the wells located at the structural high and comprise the flow units 4 and 5 that and mostly consist of Shrub-rich facies and grainstones. These are followed by the intermediary flow unit 3 found in all wells, comprised of shrub-rich facies, spherulitites–rich facies, grainstones, packstones, and laminites. Moreover, among all units, the flow units 1 and 2 presented the lowest petrophysical features and are mainly found in wells located at the basinward area of the Sapinhoá field. Finally, the results indicate that key diagenetic features such as the dissolution of clay mineral, and dolomitization are notable elements that commonly enhanced the petrophysical properties. Additionally, the pervasive silicification process decrease the reservoir quality. These processes are often found in the wells located at both the structural high and the basinward area of the Sapinhoá field.

Keywords: Pre-salt. Carbonate petrophysics. Formation evaluation. Santos Basin.

LISTA DE FIGURAS

LISTA DE TABELAS

LISTA DE ABREVIATURAS OU SIGLAS

ANP	- Agência Nacional do Petróleo, Gás Natural e Biocombustíveis
APT	- Apatita (*Apatite*)
BAR	- Barita (*Barite*)
BHI	- Perfil de imagem do poço (*Borehole image log*)
BVF	- Formação Barra Velha (*Barra Velha Formation*)
CAL	- Calcita (*Calcite*)
Claymin	- Minerais de argila (*Clay minerals*)
DAW	- Dawsonita (*Dawsonite*)
CBW	- Perfil ressonância magnética nuclear *Clay bound water*
CDA	- Ca-dolomita/Ankerita (*Ca-dolomite/Ankerite*)
CMG	- Calcita magnesiana (*Mg-calcite*)
COR	- Coríndon (*Corundum*)
CRT	- Cristolabita (*Cristobalite*)
DOL	- Dolomita (*Dolomite*)
DCD	- Dolomita/Ca-dolomita (*Dolomite/Ca-dolomite*)
DRX	- Difratometria de raios-X (*X-ray difratometry*)
DTC	- Perfil vagarosidade acústica compressional (*compressional slowness*)
FF	- Perfil ressonância magnética nuclear fluido livre (*Free fluid*)
FLU	- Fluorita (*Fluorite*)
FZI	- Indicador de zona de fluxo (*Flow zone indicador*)
FWL	- Zona de transição base coluna hidrocarboneto-água (*Free water level*)
GR	- Perfil raios gama (*Gamma Ray*)
GRKT	- Perfil raios gama espectral, fração potássio
GRKUT	- Perfil raios gama espectral, fração urânio
GRTH	- Perfil raios gama espectral, fração tório
HAL	- Halita (*Halite*)
HFU	- Unidade de zona de fluxo (*Hydraulic flow units*)
IAU	- Discordância Intra-Alagoas (*Intra-Alagoas unconformity*)
KFD	- Feldspato potássico (*K-Feldspar*)
LBVF	- Formação Barra Velha inferior (*Lower Barra Velha Formation*)
LWD	- *Logging while drilling*
MAG	- Magnesita (*Magnesite*)

NMR   - Perfil ressonância magnética nuclear (*Nuclear magnetic resonance*)

NPHI   - Perfil porosidade nêutron (*Neutron porosity*)

NPI   - Índice de porosidade normalizada (*Normalized porosity index*)

PCA   - Análise de componentes principais (*Principal componente analysis*)

PE   - Perfil fator fotoelétrico (*photoeletric fator log*)

PIR   - Pirita (*Pyrite*)

PLG   - Plagioclásio (*Plagioclase*)

QTZ   - Quartzo (*Quartz*)

RCAL   - Petrofísica de rotina laboratorial (*Routine core analyisis*)

RHOB   - Perfil densidade (*Density log*)

RQI   - Índice de qualidade de rocha (*Rock quality index*)

RT20   - Perfil resistividade rasa (*Shallow resistivity log*)

RT90   - Perfil resistividade profunda (*Deep resistivity log*)

SBU   - Discordância camada da base do sal (*Salt-base unconformity*)

SGO   - Svanbergita/Goyazita (*Svanbergite/Goyazite*)

SPH   - Sapinhoá

SWC   - Amostra lateral (*side-wall core*)

TUN   - Tunisita *(Tunisite)*

TVDSS   - *True Vertical Depth Sub Sea*

UBVF   - Formação Barra Velha superior *(Upper Barra Velha Formation)*

WSI   - Interface água-sedimento (*Water-sediment interface*)

WL   - Perfilagem a cabo (*Wireline logging*)

XRD   - *X-ray difratometry*

LISTA DE SÍMBOLOS

$\varnothing$	- Porosidade
$\varnothing_{gas}$	- Porosidade tipo gás para ensaio de petrofísica laboratorial
ΔP	- Diferencial de pressão
μ	- Viscosidade dinâmica
A	- Area da seção transversal
K	- Permeabilidade
K_{abs}	- Permeabilidade absoluta para ensaio de petrofísica laboratorial
L	- Comprimento da amostra
V_{bulk}	- Volume da amostra (*bulk volume*)
V_{final}	- Volume final
$V_{inicial}$	- Volume inicial
V_{pore}	- Volume de poros (*pore volume*)
V_{solid}	- Volume dos sólidos (*solid volume*)
P_{final}	- Pressão final
$P_{inicial}$	- Pressão inicial
Q	- Vazão
wt	- Peso total (*weight total*)

SUMÁRIO

1 ESTRUTURA DA DISSERTAÇÃO

De acordo com as Normas Complementares 01/21 do Programa de Pós-Graduação em Geologia da Universidade Federal do Paraná, a presente dissertação está dividida nos tópicos principais INTRODUÇÃO, RESULTADOS E DISCUSSÃO e CONSIDERAÇÕES FINAIS. Os resultados são apresentados na forma de manuscrito de artigo científico com os principais resultados da pesquisa os quais são integrados em CONSIDERAÇÕES FINAIS.

2 INTRODUÇÃO

Do ponto de vista histórico e econômico, a partir dos anos 2000 a Bacia de Santos passou a apresentar sucessos exploratórios, com destaque para a descoberta dos campos de Lula, Búzios, Libra entre outros. Os reservatórios Aptianos da Bacia de Santos compõem um super *play* petrolífero responsável pelas maiores reservas de óleo e gás do Pré-Sal brasileiro.

Assim, os reservatórios explorados na Bacia de Santos são ideais para teste de novas ferramentas e metodologias que possam ser estudadas e validadas para a aplicação prática na prestação de serviços à exploração e produção de petróleo e gás, bem como trazer novas informações que possam refinar o conhecimento sobre a gênese e evolução da bacia.

Nesse contexto, um dos métodos mais importantes na caracterização de reservatórios é a Avaliação de Formação (*Formation Evaluation*) feita a partir da correlação entre propriedades de rochas e perfis geofísicos. Essa avaliação consiste na identificação de fácies e suas características geoquímicas, mineralógicas, petrofísicas (e.g., porosidade e permeabilidade), bem como a investigação de sua relação com a saturação de fluidos, conectividade/barreiras de fluxo, propriedades acústicas, elétricas e elásticas.

Na avaliação de rochas em cenários de campos petrolíferos, as observações convencionais diretas via descrição de rochas dependem essencialmente da coleta de amostras em subsuperfície, como testemunhos, amostras laterais da parede do poço e amostras de cascalhos em peneiras. Em adição, petrografia, medições em laboratório de porosidade e permeabilidade de plugues testemunhados, avaliação

geoquímica por difratometria de raios-X, e análise isotópica permitem caracterizar os carbonatos nessa seção quando coletadas.

Em contrapartida, dados de perfilagem de poços (*well-logging*), possuem a capacidade de medições diretas e indiretas de registros de várias propriedades das rochas em profundidade que permitem caracterizar toda a seção perfurada do poço. O método reúne a aquisição de dados relacionados às propriedades petrofísicas, geoquímicas, identificações de estratos rochosos, e presença de hidrocarbonetos, realizadas a partir de ferramentas a cabo (*wireline*) (Rider, 2011).

Assim, a integração rocha e perfis geofísicos é essencial para um melhor entendimento e caracterização dos reservatórios, permitindo melhor compreender o ambiente deposicional, diagênese e suas implicações nas características dos reservatórios carbonáticos Aptianos do Pré-Sal na Bacia de Santos.

2.1 JUSTIFICATIVA

A heterogeneidade e alta complexidade faciológica existente nos carbonatos lacustres da Formação Barra Velha do Pré-Sal brasileiro, representam um enorme desafio na caracterização de suas propriedades petrofísicas (e.g., Terra *et al*., 2010; Wright & Barnett, 2015; Farias *et al*., 2019; Lima & De Ros, 2019; Wright, 2020).

O reconhecimento de eventos cíclicos e deposicionais, e suas implicações na petrofísica dos carbonatos do Pré-Sal ainda não é totalmente compreendido no contexto geológico da abertura do Oceano Atlântico Sul.

Estudos recentemente publicados propõem modelos genéticos sobre a alternância nas condições paleoclimáticas do lago, baseados em estudos sísmicos para a evolução em plataformas carbonáticas (Faria *et al*., 2017). Além disso, estudos de ciclos hidroquímicos (únicos e estacionários) para lagos alcalinos com atividade vulcânica em diferentes taxas de evaporação (Mercedes-Martín *et al*., 2019), bem como variações paleo-hidrológicas descritas com base em geoquímica isotópica, corroboram e indicam mudanças ambientais durante a gênese dos carbonatos (Saller et al., 2016; Sabato Ceraldi & Green, 2017; Farias *et al*., 2019; Pietzsch *et al*., 2018, 2020).

Os padrões cíclicos criam sucessões verticais de fácies carbonáticas bem definidas e impactam na qualidade petrofísica dos carbonatos do Pré-Sal. Estudos na Bacia de Campos (Herlinger *et al*., 2017; Muniz & Bosence, 2015, 2018) mostram

correlações importantes entre as fácies descritas e a distribuição da porosidade e da permeabilidade das rochas. Os reservatórios carbonáticos podem estar hidrotermalizados, e as rochas parcialmente dolomitizadas e silicificadas; modificando essas características petrofísicas da rocha reservatório. Esses processos podem impactar na qualidade do reservatório, causando tanto aumento ou a diminuição da porosidade e permeabilidade (Lima *et al*., 2020).

Apesar da relevância do tema, poucos estudos mostraram correlações das propriedades de rocha (petrofísicas) e perfis geofísicos para a avaliação da Formação Barra Velha, na Bacia de Santos (Boyd *et al*., 2015; Brelaz *et al*., 2019). Comumente os trabalhos dedicam-se à identificação de perfis de elementos químicos, ou a calcular porosidade e saturação de fluidos no reservatório sem o prévio reconhecimento de processos diagenéticos, como a dissolução de argilas magnesianas, silicificação e dolomitização que impactam na qualidade do reservatório.

Dessa forma, para melhor avaliação dos reservatórios carbonáticos aptianos do Pré-Sal brasileiro, uma abordagem interessante é a utilização combinada de dados de rochas e perfis a fim de identificar a ciclicidade das fácies, em contexto estratigráfico de alta resolução (testemunho-perfis geofísicos) e a influência das propriedades petrofísicas na avaliação de formação.

2.2 OBJETIVOS

O objetivo desse estudo é a caracterização petrofísica dos carbonatos da Formação Barra Velha no campo de Sapinhoá (FIGURA 1), localizado na Bacia de Santos, mediante o uso integrado de dados de rocha e perfilagem, mostrando as implicações para a caracterização de reservatórios carbonáticos atualmente explorados.

2.3 ÁREA DE ESTUDO

A área de estudo situa-se a sul da Bacia de Santos, no campo de Sapinhoá (FIGURA 1), em estrutura alongada na direção NE-SW. O campo possui aproximadamente 230 km² e reservas estimadas em 3,311 milhões de barris de óleo e 99,307 milhões de m³ de gás natural em volume original *in situ* (ANP, 2017).

Os poços estão situados abaixo do nível do mar, em lâmina de água aproximadamente a 2140 metros, com intervalo aproximadamente perfurado de 500 metros de rochas carbonáticas abaixo da base do sal.

FIGURA 1 – LOCALIZAÇÃO DO CAMPO DE SAPINHOÁ (SPH) COM OS POÇOS ESTUDADOS, NA BACIA DE SANTOS
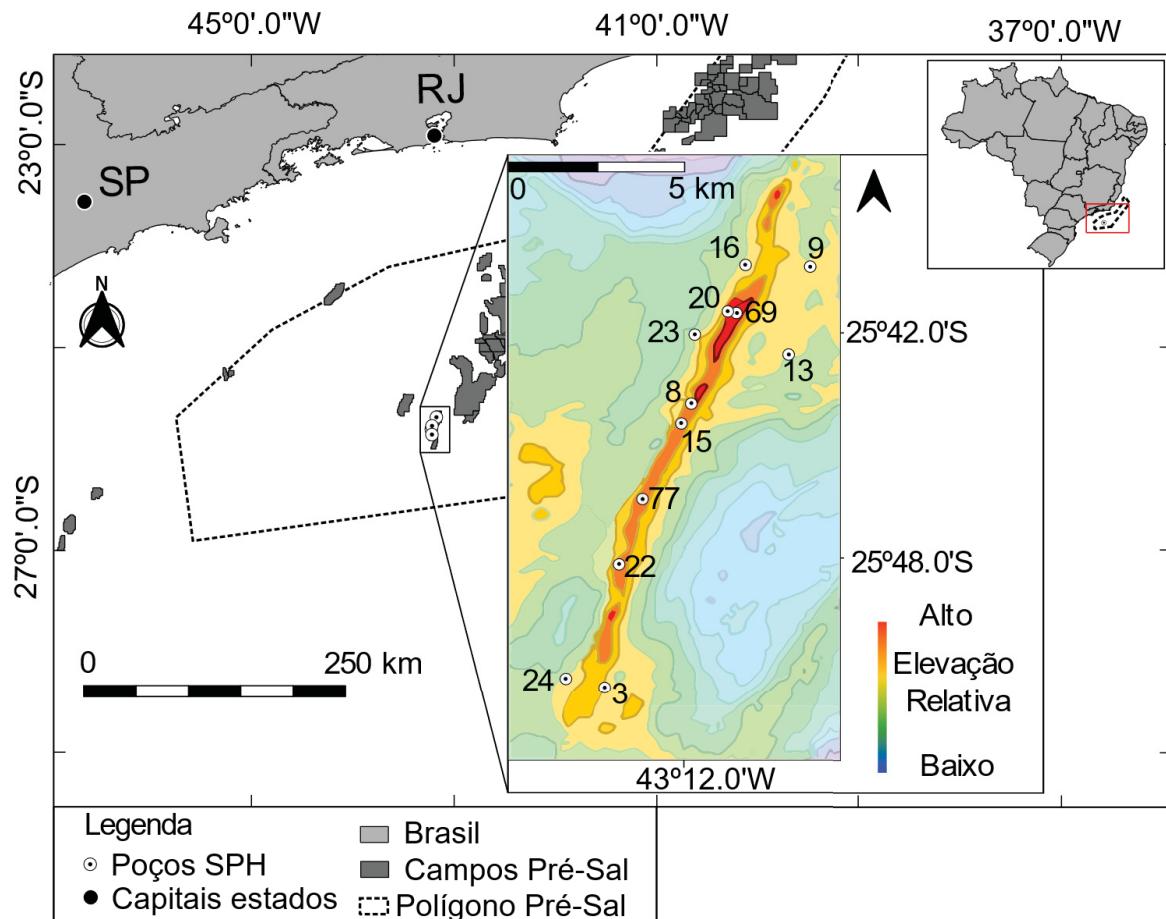
FONTE: O autor (2021). Modificado de GeoANP (2021).

2.4 REVISÃO DE LITERATURA

2.4.1 Contexto geológico

A Bacia de Santos é uma bacia costeira do sudeste brasileiro, geograficamente situada entre os paralelos 23º e 28º Sul, ocupando cerca de 350.000 km², abrangendo o litoral dos estados de Rio de Janeiro, São Paulo, Paraná e Santa Catarina. A bacia é limitada ao norte pelo Alto de Cabo Frio com a Bacia de Campos e ao sul pela plataforma de Florianópolis com a Bacia de Pelotas (Moreira *et al*., 2007).

A origem e evolução da Bacia de Santos estão relacionadas ao evento de ruptura do Supercontinente Gondwana, iniciado no Neocomiano, que culminou com a abertura do Oceano Atlântico Sul e a implantação das bacias marginais brasileiras ao longo do chamado Sistema de Riftes do Leste Brasileiro (Chang *et al*., 1992).

No arcabouço tectônico-estratigráfico da bacia (FIGURA 2) é encontrado o embasamento cristalino de idade pré-cambriana, discordantes com a Formação Camboriú (130-120 Ma), constituída de basalto cinza-escuro, holocristalino, granulação média, textura ofítica (diabásio), tendo por constituintes principais o plagioclásio e o piroxênio (augita), comumente pouco alterados (Moreira *et al*., 2007).

A sequência rifte lacustre da Formação Piçarras, Grupo Guaratiba (Barremiano), é delimitada por discordância no topo dos basaltos da Formação Camboriú (limite inferior), e pela discordância superior Pré-Alagoas (superior) (FIGURA 2). A Formação Piçarras corresponde a conglomerados e arenitos polimíticos constituídos de fragmentos de basaltos, quartzo e feldspato, depositado por leques aluviais nas porções proximais, e por arenitos, siltitos e folhelhos de composição talco estevensítica nas porções lacustres (Moreira *et al*., 2007).

A Formação Itapema, corresponde à sequência K38, é caracterizada por apresentar intercalações de calcirruditos e folhelhos escuros. Os calcirruditos são constituídos por fragmentos de conchas de bivalves que frequentemente encontram-se dolomitizados e/ou silicificados, muitas vezes formando e o acumulações de empacotamento denso, conhecidos como coquinas. Nas porções mais distais da margem costeira ocorrem folhelhos escuros, ricos em matéria orgânica.

Conglomerados e arenitos, depositados em leques aluviais, representam as fácies proximais desta unidade (Moreira *et al.*, 2007).

Os carbonatos da área de estudo estão inseridos no contexto das sequências K44 e K46-48 (Moreira *et al.*, 2007). A sequência K44 corresponde à porção inferior da Formação Barra Velha (Eo-Aptiana), equivalente ao andar local Alagoas inferior. Tem seu limite inferior representado pela discordância Pré-Alagoas (123 Ma), e superior pela discordância Intra-Alagoas (117 Ma) que corresponde a um refletor sísmico de forte impedância acústica positiva de caráter regional (Moreira *et al.*, 2007). O ambiente deposicional desta sequência é marcado por um ambiente lacustre, bastante estressante, com a deposição de calcários microbiais, incluindo estromatólitos e laminitos (Terra *et al.*, 2010), nas porções proximais, e folhelhos nas porções distais (Moreira *et al.*, 2007).

Recentemente foram publicados estudos sobre a contribuição quimiogênica na deposição e precipitação dos carbonatos da Formação Barra Velha (Bacia de Santos) e Formação Macabú (Bacia de Campos) (Wright & Barnett, 2015; Herlinger *et al.*, 2017; Farias *et al.*, 2019; Lima & De Ros, 2019; Gomes *et al.*, 2020; Wright, 2020).

FIGURA 2 – CARTA ESTRATIGRÁFICA DA BACIA DE SANTOS
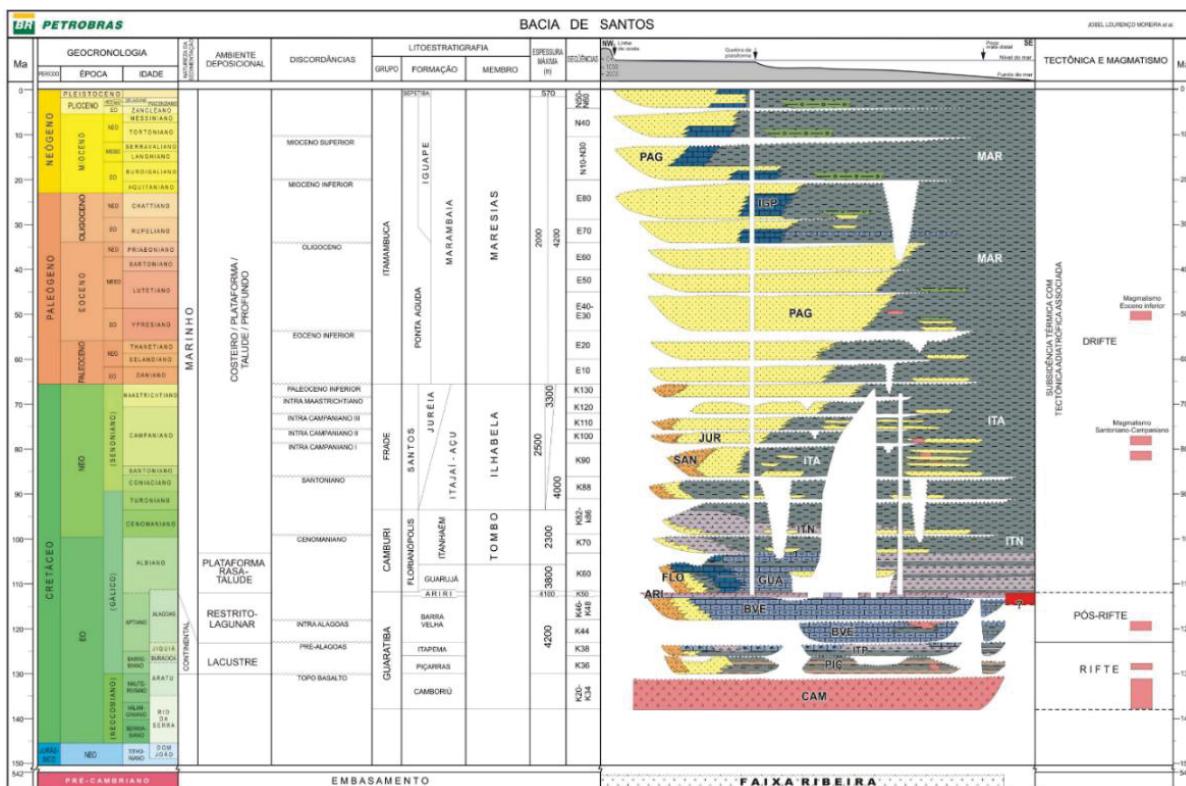
FONTE: Moreira *et al.*, (2007).

Tais estudos sobre os carbonatos da Formação Barra Velha caracterizam o paleoambiente deposicional de lago alcalino em condições de clima árido. A gênese dos carbonatos está associada com a precipitação química de argilas magnesianas, formação *in situ* de calcitas de forma esferoidal e de crostas de calcita fascicular com hábito radial fibroso (*Shrubs*). Tais fácies sedimentares apontam para a formação e precipitação abiótica desses carbonatos do Pré-Sal, das Bacia de Santos e da Bacia de Campos (Wright & Barnett, 2015; Tosca & Wright, 2018; Farias *et al.*, 2019; Lima & De Ros, 2019; Lima *et al.*, 2020; e Wright, 2020).

As fácies descritas incluem carbonatos sustentados pela matriz (*Mudstone, Wackestones e Lamintos*), carbonatos sustentados por grãos (*Grainstone, Rudstones e Packstone*), carbonatos ricos em *shrubs (shrub–rich)* (Wright & Barnett, 2015; Herlinger *et al.*, 2017; Farias *et al.*, 2019; Lima & De Ros, 2019; Gomes *et al.*, 2020; Wright, 2020), estromatólitos (Moreira *et al.*, 2007) e esferulititos (*spherulite–rich*) (Wright & Barnett, 2015; Herlinger *et al.*, 2017; Farias *et al.*, 2019; Lima & De Ros, 2019; Gomes *et al.*, 2020; Wright, 2020).

Adicionalmente são descritas a presença de retrabalhamento de carbonatos ricos em *shrubs*, esferulitos e dos carbonatos grãos sustentados (Wright & Barnett, 2015; Herlinger *et al.*, 2017; Farias *et al.*, 2019; Lima & De Ros, 2019; Gomes *et al.*, 2020; Wright, 2020). Por fim, é comum encontrar a presença parcial ou total de dolomitização e/ou silicificação na Formação Barra Velha (Wright & Barnett, 2015; Herlinger *et al.*, 2017; Farias *et al.*, 2019; Lima & De Ros, 2019; Gomes *et al.*, 2020; Wright, 2020).

As porções proximais do lago da Formação Barra Velha são descritas como depositados em leques aluviais (Moreira *et al.*, 2007). Adicionalmente, a superior da Formação Barra Velha (K46-K48), de idade neoaptiana (andar local Alagoas superior), possui limite inferior marcado pela discordância Intra-Alagoas e limite superior correspondente à base dos evaporitos da Formação Ariri (113 Ma), que marcam a passagem da sequência sedimentar clástica/carbonática para um ambiente evaporítico (Moreira *et al.*, 2007).

Os carbonatos da Formação Barra Velha estão sobrepostos pela Formação Ariri, constituída por uma espessa acumulação de evaporitos (idade Alagoas Superior) tais como anidrita, halita, silvita e carnalita, em um contexto de clima árido (Moreira *et al.*, 2007). Esses evaporitos atuaram como selos estratigráficos para a acumulação dos hidrocarbonetos da Bacia de Santos (Moreira *et al.*, 2007).

Por fim, a Supersequência Drifte é constituída de sedimentos marinhos acumulados durante a subsidência térmica e tectônica adiastrófica da Bacia de Santos (Moreira *et al*., 2007). Nessa sequência encontraram-se o Grupo Camburi (entre Albiano e o Cenomaniano), Grupo Frade (compreendendo o Turoniano ao Maastrichtiano) e do Grupo Itamambuca (Paleógeno ao Recente).

2.4.2 Litofácies carbonáticas da Formação Barra Velha

Nessa seção é feita uma breve revisão das principais litofácies reconhecidas nos carbonatos aptianos do Pré-Sal, recentemente descritas nas bacias de Santos e Campos (Wright & Barnett, 2015; Herlinger *et al*., 2017; Farias *et al*., 2019; Lima & De Ros, 2019; Gomes *et al*., 2020; Wright, 2020), e utilizadas nesse trabalho. A classificação dos carbonatos do Pré-Sal ainda é amplamente discutida.

Na seção ANEXOS encontram-se as classificações de rochas carbonáticas de Dunham (1962), Embry e Klovan (1971) e Terra *et al*., (2010), para revisão e fácil consulta do leitor, uma vez que são também utilizadas em outros trabalhos científicos.

2.4.2.1 Carbonatos matriz sustentada

Estudos recentemente publicados no Pré-Sal da Bacia de Santos (Gomes *et al*., 2020 e Wright., 2020) classificam os carbonatos matriz sustentada, predominantemente compostos de fração lama carbonática (m*ud*), constituídas de minerais de argila, calcita, dolomita e sílica. Outros estudos referem-se a esses carbonatos como *mudstone*, *wackestones* e laminitos (*laminites*), com base nas texturas das rochas, a presença de laminações e a porcentagem de componentes do arcabouço (Terra *et al*., 2010; Faria *et al*., 2017; e Farias *et al*., 2019). O presente trabalho, reconhece a diferença de textura deposicional desses carbonatos individualmente (*mudstones, wackestones* e laminitos), somente agrupando-os como carbonatos matriz sustentada (*matrix–supported*) quando as fácies são referidas em conjunto.

Em escala de testemunho, plugues e amostras laterais, essas litofácies apresentam cor marrom claro a escuro e mostram laminação do tipo plano-paralela horizontal, com espessuras variando de milímetros a centímetros (Gomes *et al*.,

2020). Segundo Gomes *et al*. (2020) as argilas encontradas estão intercaladas entre camadas maciças ou apresentam-se dispostas em laminações em escala milimétrica.

Ao microscópio petrográfico de luz transmitida em seção delgada as argilas constituem-se de grãos opticamente transparentes de agregados de argilominerais (FIGURA 3). Em geral, os minerais de argila podem apresentar certo grau de substituição por dolomita microcristalina e sílica microcristalina. Em outros casos, substituição por micrita, mas podendo apresentar certo grau de substituição por dolomita e sílica. Parte da dolomita/sílica pode ser primária, mas provavelmente formada por meio de um precursor metaestável (Gomes *et al*., 2020).

FIGURA 3 – EXEMPLOS DE CARBONATOS MATRIZ SUPORTADA
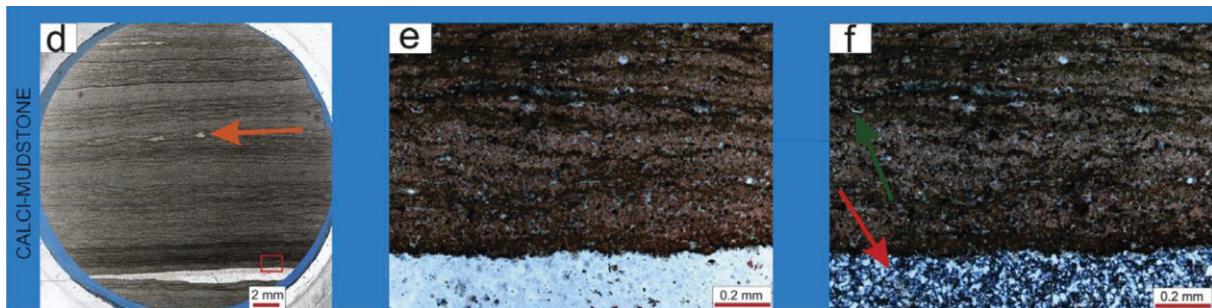
FONTE: Gomes *et al*., (2020).

LEGENDA: Exemplo de laminitos em fotomicrografias em luz transmitida. Segundo os autores. d) A seta laranja indica partícula de fosfato, polarizador paralelo, e) Laminito parcialmente silicificado em polarizador cruzado, f) A seta verde aponta quartzo microcristalino, e a seta vermelha aponta a substituição de calcita por calcedônia, polarizador cruzado.

Ainda em escala de microscopia óptica, as amostras apresentam lâminas compostas por calcitas claras compostas por calcita microcristalina, enquanto as lâminas com minerais de aparência escura, são compostas por dolomita microcristalina e romboédrica, podendo apresentar matéria orgânica. Algumas amostras descritas por Gomes *et al*. (2020) apresentam finos grãos de tamanho silte geralmente, ostracodes e partículas fosfáticas.

Por fim, os principais minerais de argila presentes nessas litofácies, são kerolita, estevensita, saponita, sepiolita, illita e esmectita (Madrucci *et al*., 2013; Souza *et al*., 2018).

2.4.2.2 Esferulititos

Esses carbonatos são constituídos de calcitas de formato esférico a subesférico. Conforme descrito por Gomes *et al*. (2020), a vista macroscópica, em escala de testemunho, plugues e amostras laterais; essas litofácies apresentam calcitas esferulíticas de formato assimétrico, com crescimento preferencial em uma direção particular. Gomes *et al*. (2020) indicam que na maioria dos casos, os esferulitos tendem a apresentar sobrecrescimento em direção ascendente, enquanto em algumas camadas os esferulitos crescem paralelamente ao acamamento.

Adicionalmente, em escala microscópica, alguns esferulitos são encontrados misturados às calcitas de formato fascicular (*shrubs*), segundo a descrição de Lima & De Ros (2019); retendo textura fibrorradial característica (Gomes *et al*., 2020). Em tais situações, a composição dominante entre as calcitas fasciculares e esferoidais é usada para determinar o nome das litofácies (Gomes *et al*., 2020).

As calcitas esferoidais apresentam extinção radial (FIGURA 4), sendo comumente encontras dolomitizadas ou recristalizadas, com diâmetro de ordem milimétrica, com valor de referência 0,1 mm a 4 mm (Gomes *et al*., 2020). Em alguns casos, podem ser reconhecidos núcleos compostos por micrita criptocristalina, argilominerais e, mais raramente, fragmentos de ostracodes (Gomes *et al*., 2020). Ainda é possível encontrar a substituição de calcita por minerais de calcedônia e de microquartzo; resultando localmente na perda da textura original (Gomes *et al*., 2020).

FIGURA 4 – EXEMPLOS DE CARBONATOS ESFERULITITOS
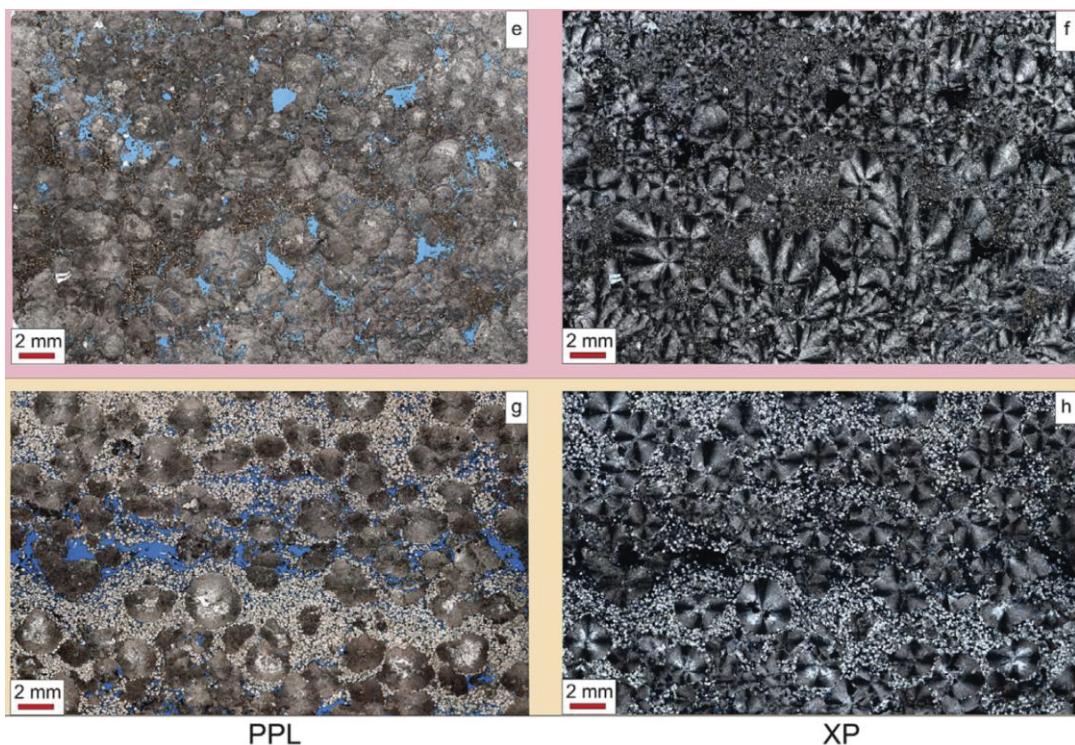
FONTE: Gomes *et al*., (2020).

LEGENDA: Exemplo de fotomicrografias de esferulititos em luz transmitida. Segundo os autores, PPL – polarizador paralelo, e XP – polarizador cruzado, ilustrando as calcitas de formato esférico.

Por fim, Wright & Barnett (2015) propuseram que os esferulitos encontrados na Formação Barra Velha são de origem quimiogênica. Com base em estudos experimentais, esses autores descrevem que os esferulitos são o produto de rápido crescimento de cristais em soluções alcalinas e viscosas, altamente enriquecidas em magnésio e sílica que fornecia o suporte para o crescimento dessas calcitas.

2.4.2.3 Carbonatos ricos em shrubs

A litofácies carbonáticas ricas em *shrubs* (Wright & Barnett, 2019; Wright, 2020) são carbonatos predominantemente compostos de calcita e formam estruturas sedimentares de formato arborescente, arbustiforme, pluma, dômico e convexo. Esses carbonatos ricos em *shrubs* ocorrem predominantemente em camadas horizontais, ou sobrepostas, e localmente podem apresentar tamanho entre centimétrico, podendo chegar a 5 metros de altura (Wright & Barnett, 2015; Farias *et al*., 2019; Gomes *et al*., 2020).

Microscopicamente, as calcitas apresentam formato fascicular (Herlinger *et al*., 2017; Lima & De Ros, 2019; Lima *et al*., 2020) com o longo eixo de sua estrutura em forma de leque variando de 0,15 a 6,5 mm de comprimento (valor de referência, Gomes *et al*., 2020) (FIGURA 5).

FIGURA 5 – EXEMPLOS DE CARBONATOS SHRUBS
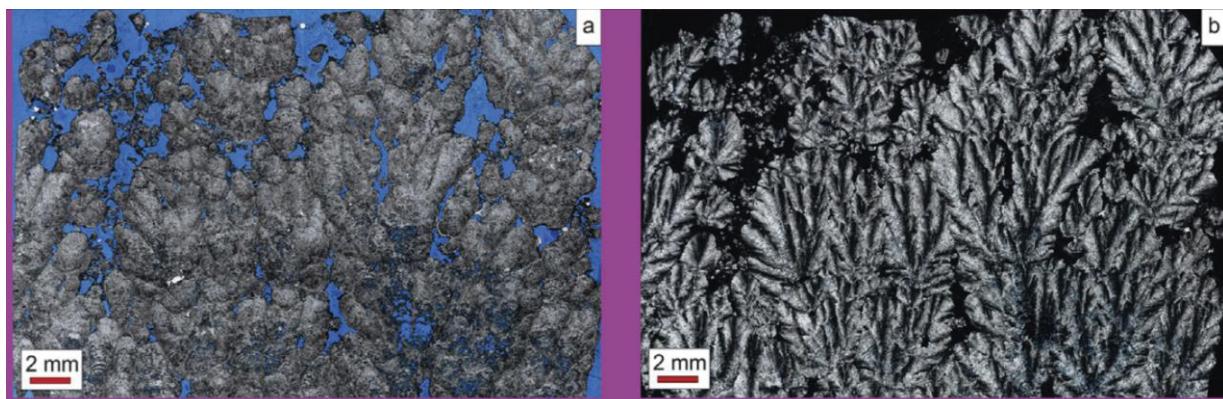
FONTE: Gomes *et al*., (2020).

LEGENDA: Exemplo calcitas em formato fascicular, segundo os autores. Fotomicrografias em luz transmitida. a) Polarizador paralelo, b) Polarizador cruzado.

De acordo com Gomes *et al*. (2020), alguns *shrubs* incorporam grãos detríticos finos aleatórios ou, raramente, biogrãos em sua estrutura, localmente apresentando mais de uma forma de sobrecrescimento. Conforme descrito pelos autores, dentro de uma camada individual, os *shrubs* são orientados paralelamente uns aos outros, variando de densamente compactados (0,2 mm entre os eixos centrais) a amplamente espaçados (espaçamento de 4 mm).

De acordo com Wright (2020), as calcitas tipo *shrubs in situ* são separadas por poros abertos ou preenchidos com silicatos de magnésio, ou cimento de sílica ou dolomita. O autor reporta ainda que em alguns casos, dolomitas romboédricas são encontradas entre o espaço poroso, predominantemente abertos.

2.4.2.4 Microbialitos

Estudos publicados reportam carbonatos de origem microbial nos reservatórios aptianos das rochas das bacias de Campos (Terra *et al*., 2010; Rezende e Pope, 2015, Muniz & Bosence, 2015, 2018), Santos (Kaczmarek &

Hasiuk, 2015; Pietzsch *et al*., 2020), e também encontradas na bacia de Kwanza, África (Sabato Ceraldi & Green, 2017).

Conforme publicado por Wright (2020) os carbonatos de origem microbial, como os estromatólitos e dendrólitos são normalmente encontrados nos 20 a 30 metros superiores da Formação Barra Velha, no marco estratigráfico conhecido na indústria como *Lula fingers.* De acordo com Wright & Barnett (2015), as macroestruturas microbianas encontradas não representam mais do que 1% da espessura dos testemunhos recuperados área do campo de Lula, na Bacia de Santos. Adicionalmente, Wright (2020) salienta que evidências microbianas em lâminas delgadas são baixas, na ordem de 0,05%.

2.4.2.5 Carbonatos grãos sustentados

As litofácies descritas como *grainstones, packstones e rudstones* encontradas no Pré-Sal são comumente descritas seguindo a classificação de Dunham (1962); Embry & Klovan (1971) e Terra *et al*., (2010). Esses carbonatos apresentam textura deposicional reconhecíveis, sustentada por grãos de diferentes tamanhos (FIGURA 6).

FIGURA 6 – EXEMPLOS DE CARBONATOS TIPO *GRAINSTONES, PACKSTONES E RUDSTONES*
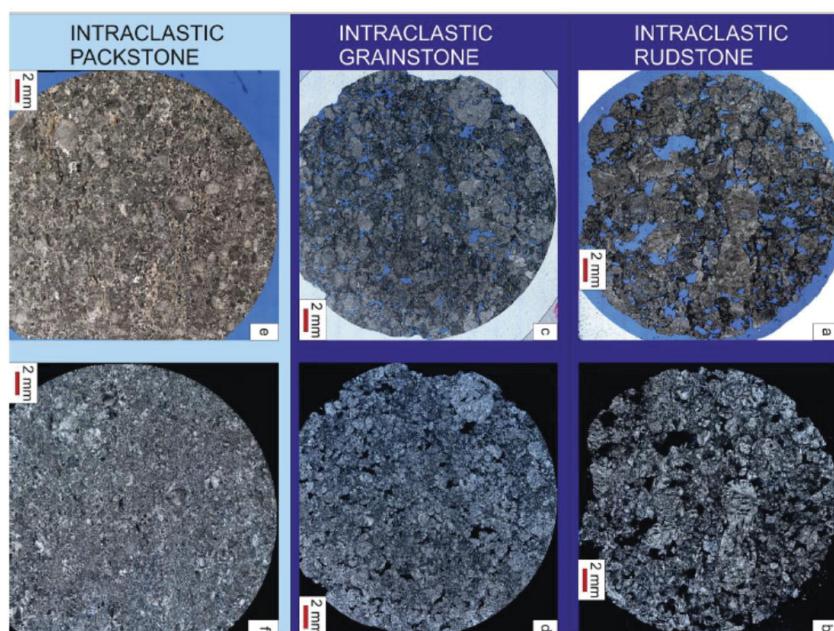
FONTE: Gomes *et al*., (2020).

LEGENDA: Classificação de fácies carbonáticas grão-suportado e retrabalhadas, segundo os autores. Fotomicrografias em luz transmitida, em pares respectivos, polarizador paralelo e polarizador cruzado. a) e b) *Rudstone* intraclástico, c) e d) G*rainstone* intraclástico, e) e f) *Packstone* intraclástico.

Essas litofácies são interpretadas como o produto do retrabalhamento de fácies carbonáticas previamente depositadas (e.g., carbonatos ricos em *shrubs*, esferulitos e laminitos) (Gomes *et al*., 2020). O presente trabalho, reconhece a diferença de textura deposicional desses carbonatos individualmente (*grainstones, packstones* e *rudstones*) e os agrupa como fácies sustentada por grãos (*grain–supported facies*), quando são referidos em conjunto.

Essas fácies são constituídas principalmente de fragmentos de crostas de calcita fascicular (Lima & De Ros, 2019; Lima *et al*., 2020 e Wright, 2020), esferulitos, agregados laminados de argila magnesiana e carbonatos laminados, majoritariamente retrabalhadas na Bacia de Santos (Gomes *et al*., 2020). Os *grainstones* intraclásticos encontrados nas bacias de Santos e Campos podem apresentar estratificação ou estrutura maciça (sem estrutura visível). Por fim, *rudstones* ocorrem localmente compactados e cimentados (Lima & De Ros, 2019; Gomes *et al*., 2020).

Grainstones texturalmente maduros e os *rudstones* ocorrem em sucessões sedimentares decamétrica compostas de grãos bem selecionados e arredondados de calcitas *shrubs*, esferulitos, intragrãos e, em alguns casos, pelóides e fragmentos vulcânicos (Barnett *et al*., 2018; Wright, 2020). Os *grainstones* e *rudstones* conformam camadas de escala decimétrica a métrica, apresentando estratificação horizontal, de baixo ângulo e subordinadamente laminação cruzada e estratificação cruzada planar (Wright, 2020).

Segundo Lima & De Ros (2019) o tamanho dos grãos variam entre 0,06 e 4,1 mm, com tamanho modal de 0,8 mm (Lima & De Ros, 2019). De acordo com Herlinger *et al*. (2017), é possível encontrar a presença de matriz argilosa nessas fácies, em amostras coletadas em poços na bacia de Campos; e, portanto, para os autores consideradas como rochas híbridas.

Os principais tipos de porosidade encontrados em seção delgada nos *grainstones* e *rudstones* intraclásticos são do tipo interpartícula primária e secundária; além disso, são encontrados as do tipo intracristalina e intrapartícula, associadas à porosidade vugular e fraturas (Lima & De Ros, 2019).

Esses carbonatos podem estar associados ao estreitamento acentuado da Formação Barra Velha, em torno das margens falhadas de blocos inclinados, e potencialmente representando depósitos sedimentares de deltas dominados por ondas (Barnett *et al*., 2018).

2.4.2.6 Dolomitos

Os dolomitos (*dolostones*) são carbonatos descritos em diversos estudos nos carbonatos do Pré-Sal (e.g., Saller *et al*., 2016; Sabato Ceraldi & Green, 2017; Herlinger *et al*., 2017; Farias *et al*., 2019; Lima & De Ros, 2019; Wright & Barnett, 2015, 2019; Pietzsch *et al*., 2020; Lima *et al*., 2020).

Em geral, essas fácies apresentam-se totalmente ou parcialmente dolomitizadas, com grau de dolomitização incipiente a muito intensa, de forma pervasiva, e observadas principalmente em camadas centimétricas a métricas nos testemunhos, plugues e amostras laterais. Adicionalmente, a dolomita é o principal mineral que substitui as principais componentes preexistentes da rocha.

Nos dolomitos encontrados na Formação Macabú (Aptiano) da Bacia de Campos (Lima & De Ros, 2019) há preenchimento de espaço entre os poros por minerais como: dolomitas em blocos (mosaico fino), dolomita em sela, calcita fibrosa e laminada (mosaico) a calcedônia (botróidal), quartzo drusiforme e sílica (FIGURA 7).

FIGURA 7 - EXEMPLO DE DOLOMITOS
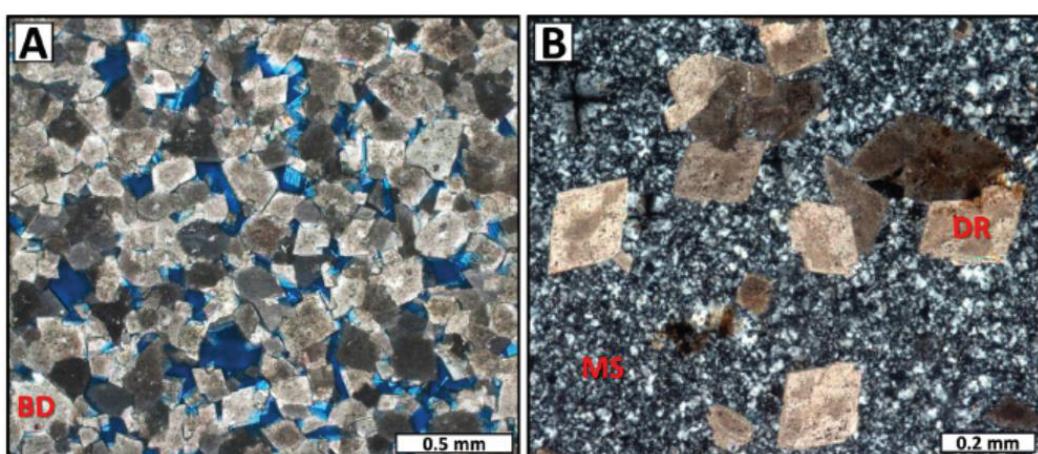
FONTE: Lima & De Ros (2019).

LEGENDA: Segundo os autores, exemplos fotomicrografias em luz transmitida de dolomitos encontrado em camadas dolomitizadas. a) polarizador cruzado, dolomitos apresentando dolomita tipo

bloco (BD), e b) polarizador cruzado, dolomita romboédrica (DR) intensamente substituída por quartzo microcristalino (MS), conforme a descrição dos autores.

Secundariamente, os componentes primários são substituídos por barita, celestina, sulfetos, svanbergita e betume. Essas fases preenchem os agregados intracristalino, com dissolução da matriz de argila, laminar, intercristalina, porosidade móldica, vugular e porosidade secundária de fratura (Lima & De Ros, 2019). Por fim, o tamanho dos minerais variam entre 0,01 (microcristalina) e 3,27 mm, com um tamanho modal de 0,09 mm (Lima & De Ros, 2019).

Em relação às dolomitas, elas apresentam hábitos microcristalinos e em blocos, e substituem a matriz de argila magnesiana, calcitas esferulíticas e agregados fasciculares, de forma ainda parcial a e heterogênea. Lima & De Ros (2019) reportam ainda que em muitas amostras coletadas nos poços, a dolomita substitui seletivamente as argilas estevensíticas, enquanto os *shrubs* e esferulitos são marginalmente dolomitizados.

2.4.2.7 Silexitos

Assim como os dolomitos, os silexitos foram reportados em diversos estudos nos carbonatos do Pré-Sal das bacias de Campos, Santos e Kwanza (e.g., Saller *et al*., 2016; Sabato Ceraldi & Green, 2017; Herlinger *et al*., 2017; Farias *et al*., 2019; Lima & De Ros, 2019; Wright & Barnett, 2015, 2019; Pietzsch *et al*., 2020; Lima *et al*., 2020), juntamente com carbonatos parcialmente silicificadas (Saller *et al*., 2016; Teboul *et al*., 2016; Viera de Luca *et al*., 2017; Lima & De Ros, 2019). Esta fácies encontra-se organizada em camadas centimétricas a métricas nos testemunhos, plugues e em amostras laterais; em ambas com características de silicificação pervasiva.

Microscopicamente, os principais tipos de sílica, são micro a macrocristalina, sobrecrescimento de quartzo, quartzo em formato mosaico, e calcedônia. Esses minerais encontram-se substituindo totalmente ou parcialmente os principais componentes diagenéticos preexistentes, além de preencher a porosidade secundária (FIGURA 8) (Lima & De Ros, 2019; Lima *et al*., 2020).

FIGURA 8 – EXEMPLOS DE SILEXITOS
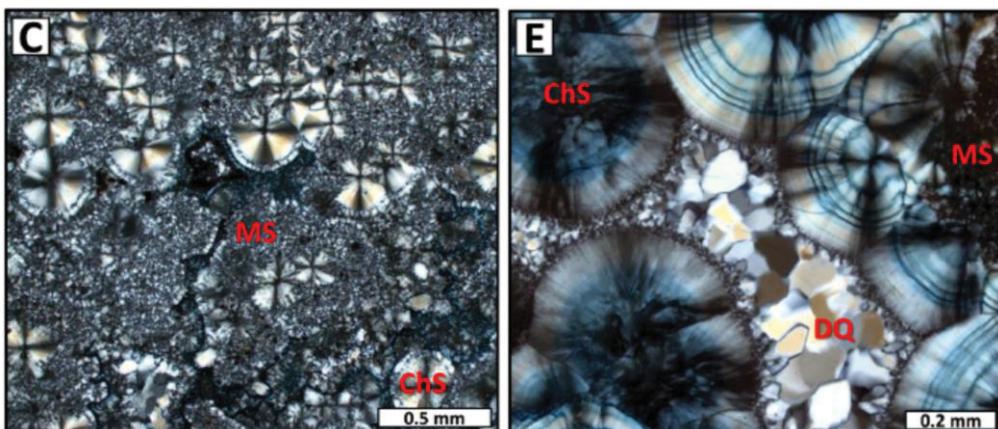
FONTE: Lima & De Ros (2019).

LEGENDA: Exemplo de fotomicrografias de silexitos. Segundo os autores, fotomicrografias em luz transmitida de silexitos encontrado em camadas parcialmente silicificadas. c) polarizador cruzado, sílica microcristalina (MS) e calcitas esferoidais envoltas de calcedônia (ChS), e) polarizador cruzado, quartzo drusiforme (DQ) e calcitas esferoidais envoltas de calcedônia (ChS) conforme a descrição dos autores.

De acordo com Lima & De Ros (2019), há amostras com presença de polimorfos de quartzo microcristalinos, como moganita, tridimita, cristobalita e svanbergita que foram constatados por meio de análises de difração de raios-X e estão associadas às fases silicosas de quartzo e calcedônia. De acordo com os mesmos autores a variação do tamanho dos cristais é 0,01 e 2,94 mm (moda 0,11 mm).

Lima & De Ros (2019) constataram também associação comum das fácies silicificadas com presença de dolomita microcristalina, dolomita em blocos e dolomita em sela, em seção delgada; com substituição dos constituintes primários, singenéticos e diagenéticos (argilas magnesianas, intragrãos e crostas de calcita e esferulitos), que comumente representam relíquias da fase de dolomitização pretérita à silicificação.

Ao microscópio petrográfico, os tipos de poros encontrados nessas amostras são secundários, principalmente intercristalinos e intra-agregado, com intenso fraturamento e dissolução após a silicificação, e formação de porosidade vugular. Muitos *vugs* e fraturas são parcialmente ou completamente preenchidos por: sílica microcristalina, quartzo tipo mosaico, quartzo sobrecrescimento, calcedônia, calcita, dolomita em bloco e em sela, sulfatos, sulfetos, svanbergita, rutilo, e betume (Lima & De Ros, 2019).

Segundo Lima & De Ros (2019), a maior parte da silicificação observada ocorreu claramente após a dolomitização, conforme indicado por restos de constituintes dolomitizados que são preservados dentro das áreas silicificadas. Para esses autores algumas amostras mostram silicificação generalizada de intragrãos dolomitizados e agregados fasciculares (*shrubs*) e de esferulitos, com escassos remanescentes de constituintes primários dolomitizados. Os restos da matriz argilosa singenética foram preferencialmente silicificados em relação aos agregados esferulitos e fasciculares de calcita (Lima & De Ros, 2019).

2.4.2.8 *Carbonatos cristalinos*

Os carbonatos cristalinos (*Crystalline*) são carbonatos de textura deposicional não reconhecíveis devido à intensa e recristalização (Dunham., 1962; Embry e Klovan 1971; Terra *et al*., 2010).

2.4.3 Ciclicidade de litofácies

Os carbonatos do Pré-Sal estão organizados em ciclos de alta frequência, consistindo de repetição regular de litofácies (Wright & Barnett, 2015; Muniz & Bosence, 2015; Faria *et al*., 2017; Lima & De Ros, 2019; Farias *et al*., 2019; Wright, 2020).

A associação é tipicamente composta de carbonatos laminados de granulação fina (*mudstones*-laminitos), seguidos por esferulititos,e carbonatos ricos em *shrubs* de altura milimétrica a centimétrica (Wright & Barnett, 2015; Farias *et al*., 2019; Lima & De Ros, 2019; Gomes *et al*., 2020; Wright, 2020). Adicionalmente encontram-se carbonatos grão-sustentados, em maioria *grainstone*, com a presença de retrabalhamento (*reworking*), (Gomes *et al*., 2020). Em geral os ciclos básicos identificados apresentam espessura de 1–2 metros, embora os exemplos variem de 0,75 a 5 metros, (FIGURA 9 e FIGURA 10) (Wright & Barnett, 2015; Wright, 2020).

FIGURA 9 – REPRESENTAÇÃO ESQUEMÁTICA DO CICLOTEMA (*CYCLOTHEM*) PROPOSTO PARA A FORMAÇÃO BARRA VELHA, NA BACIA DE SANTOS. (WRIGHT & BARNETT, 2015 E BARNETT *et al*., 2018)
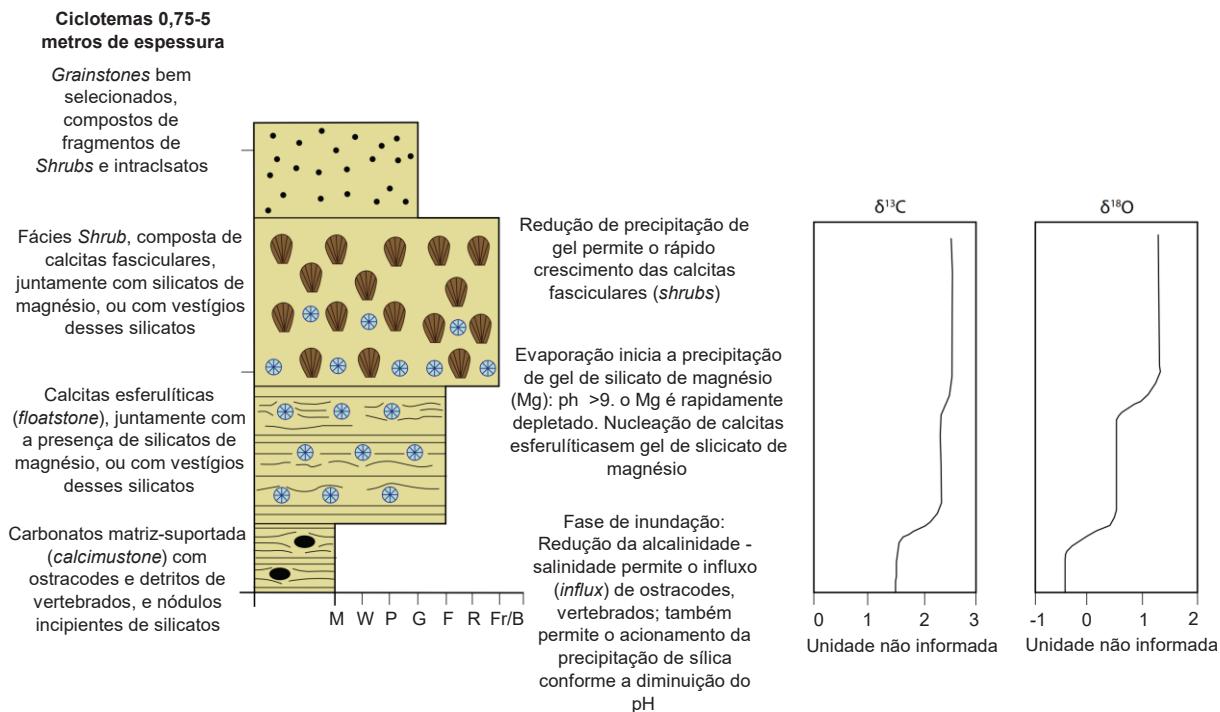
FONTE: Modificado de Wright (2020).

LEGENDA: Representação esquemática do ciclotema (*cyclothem*) proposto por para a Formação Barra Velha, na Bacia de Santos, segundo Wright (2020). Base para o topo: litofácies matriz-suportada laminadas, laminitos (*calcimudstone* laminados), esferulitos (*spherulite–rich*), *Shrub*s (*shrub–rich*) e carbonatos grão-sutentado. Os *grainstones, packstones e rudstones* são formados de fragmentos de calcitas esferoidais, calcitas fasciculares e intragrãos. Ao lado do ciclotema, Wright (2020) ilustra um perfil esquemático da variação de δ¹³C e δ¹⁸O, baseado em Barnett *et al*. (2018).

Para Wright (2020), as fácies de carbonatos finos laminados matriz-sustentada (e.g., *calcimudstones, mudstones-laminitos*) formaram-se na parte de águas relativamente profundas do lago. Ainda de acordo com o autor, os *shrubs* formados no substrato do lago, podem ter tido influência de exposição subaérea, durante o rebaixamento do lago.

FIGURA 10 – EXEMPLO DA ALTERNÂNCIA DE LITOFÁCIES EM TESTEMUNHO
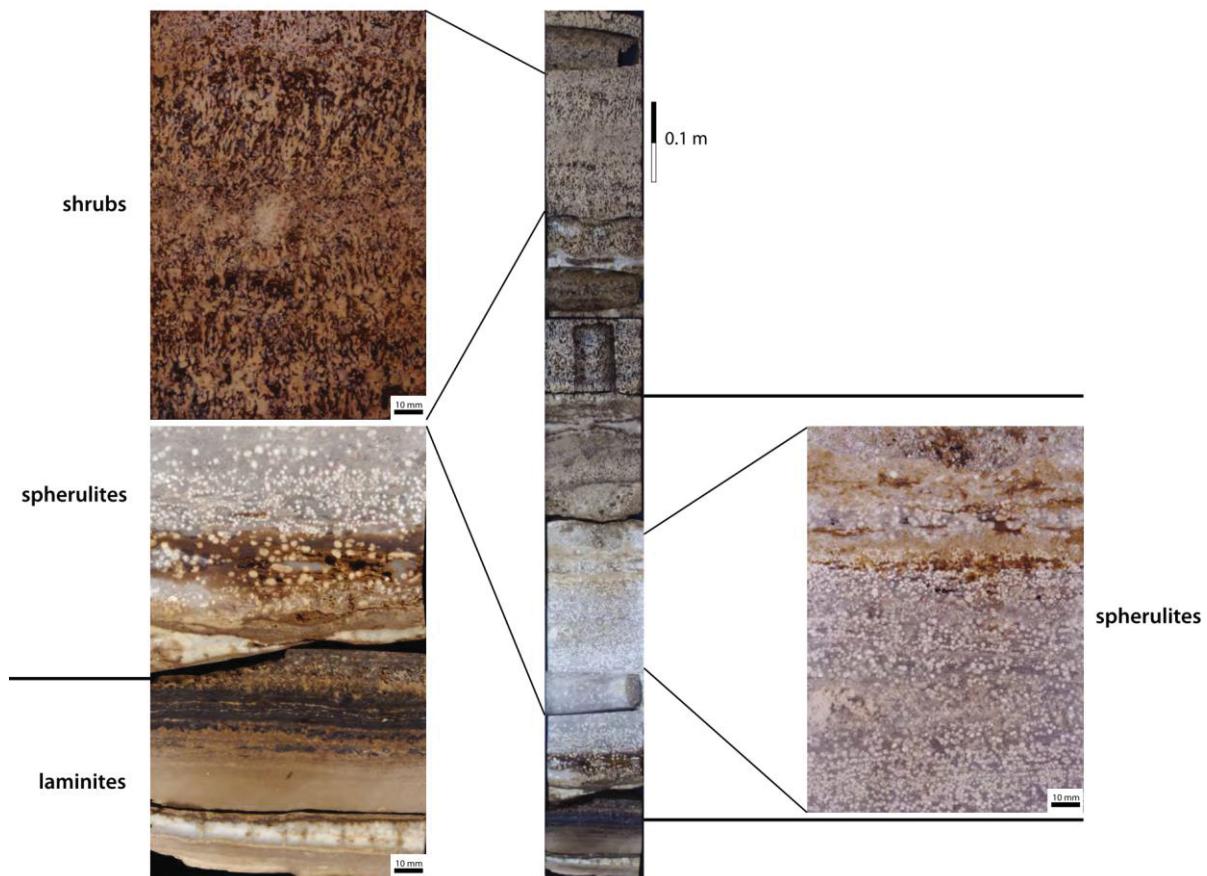
FONTE: Wright (2020).

LEGENDA: Representação esquemática em escala macroscópica da alternância de litofácies em testemunho dos carbonatos do Pré-Sal da Bacia de Santos.

De acordo com Lima & De Ros (2019), carbonatos laminados são compostos de argilas magnesianas singenéticas, peloides dispersos e grãos siliciclásticos, substituídos parcialmente. Nestas fácies, a matriz de argila magnesiana ocorre deformada pelo crescimento diagenético de calcitas esferulíticas. Os esferulitos assimétricos são formados mais próximos da interface água-sedimento (*water-sediment interface WSI*).

Por fim, os agregados de calcita fasciculares (*Shrubs*) não coalescidos e precipitados na interface água-sedimento, apresentam espaço poroso entre as calcitas fasciculares. Além disso, pode ocorrer a presença de peloides e grãos siliciclásticos entre os agregados de calcita fasciculares (Lima & De Ros, 2019). Para esses autores, o ciclo característico encontrado no Pré-Sal é representado por agregados de calcita fasciculares coalescidos no topo (calcitas singenéticas); e

matriz singenética argila magnesiana, encontrada parcialmente substituída e deslocada por calcita esferoidais e preservados na base do ciclo (FIGURA 11).

FIGURA 11– REPRESENTAÇÃO ESQUEMÁTICA DA GÊNESE DE DEPÓSITOS TÍPICOS DO PRÉ-SAL APTIANO
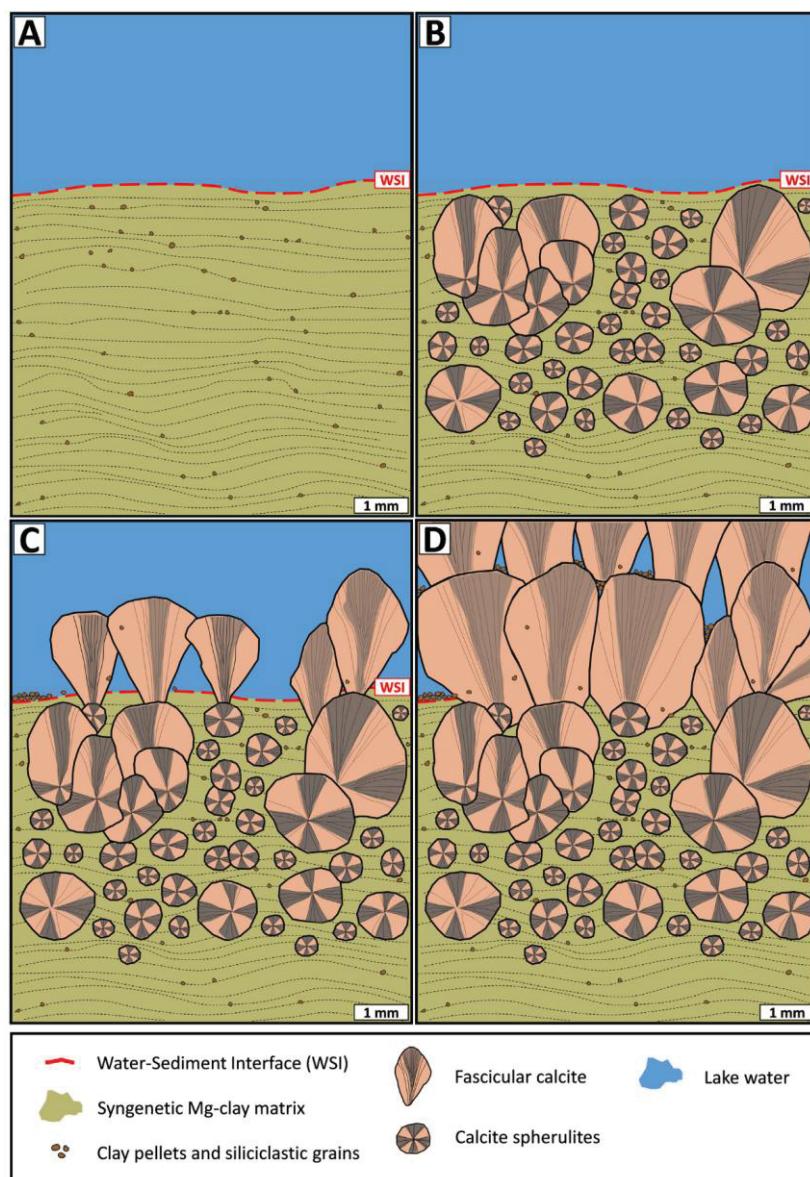
FONTE: Lima & De Ros (2019).

LEGENDA: A) Carbonatos laminados compostos de argilas magnesianas singenéticas, e presença de argila peloidal dispersas, juntamente com grãos siliciclásticos; B) Substituição parcial e deformação da matriz de argila magnesiana por calcitas esferulítica. Esferulitos assimétricos formados mais próximos da interface água-sedimento (*water-sediment interface* WSI); C) Agregados de calcita fascicular não coalescidos precipitados na interface água-sedimento, apresentando espaço poroso entre o crescimento das calcitas fasciculares. Argila peloidal e grãos siliciclásticos incluídos em alguns agregados fasciculares; D) Ciclo característico proposto, por Lima & De Ros (2019) mostrando agregados de calcita fasciculares (singenéticas) coalescidos no topo, e matriz argila magnesiana (singenética) parcialmente substituída e deslocada por esferulitos de calcita, preservados na base do ciclo (Lima & De Ros, 2019).

As recentes publicações mencionadas apontam para um consenso quanto à alternância de repetibilidade de fácies carbonáticas encontradas nas Bacias de Santos, Campos e Kwanza. No entanto, ainda há um intenso debate sobre a influência e gênese desses rochas, principalmente quanto a contribuição biogênica (Terra *et al*., 2010) e/ou quimiogênica (Wright & Barnett, 2015; Lima & De Ros, 2019; Wright, 2020) nos carbonatos do Pré-Sal.

2.5 MATERIAIS E MÉTODOS

Para esse estudo foram selecionados dados de doze poços do campo Sapinhoá, Bacia de Santos, pertencentes ao acervo de dados da Agência Nacional do Petróleo, Gás Natural e Biocombustíveis (ANP). Nesses poços foram analisados dados de perfilagem geofísica, petrofísica de laboratório (porosidade e permeabilidade), e composição mineral das rochas por difratometria de raios-X, da Formação Barra Velha.

As litofácies foram descritas com base em testemunhos (*cores*), plugues dos testemunhos (*core plugs*), amostras laterais (*side-wall cores samples*) e caracterização petrográfica por meio de fotomicrografias disponíveis no material fornecido pela ANP.

A integração entre dados de rocha e perfis foi feita a partir da amarração por profundidade, com base no ajuste dos dados de perfis de raios gama (GR) dos testemunhos, utilizando os perfis de raios gama dos perfis a cabo como referência. Posteriormente, a profundidade os dados provenientes de instrumentalização laboratorial foram ajustados à mesma referência. Por fim, para cada poço toda a informação utilizada foi individualmente referenciada ao trajeto (*survey*) e a mesa rotativa, de cada poço (*True Vertical Depth Sub Sea* - TVDSS).

Os dados de perfis geofísicos abrangem a base da camada do sal (Formação Ariri) até a profundidade final da perfilagem em poço aberto. Os perfis utilizados para a caracterização do reservatório, a avaliação da petrofísica (porosidade e permeabilidade) e caracterização de fluidos presentes no intervalo da Formação Barra Velha, foram: raios gama, espectroscopia de raios gama e de frações elementais Potássio, Tório e Urânio (K-U-Th), perfil de densidade (*density*), porosidade neutrôn (*neutron porosity*), resistividade (*resistivity*), e ressonância nuclear magnética (*Nuclear magnetic ressonance*, NMR). Por fim, os perfis de

imagem acústica e resistiva (*borehole image logs*) foram utilizados para a individualização de feições e estruturas nos carbonatos, delimitação de laminações e a orientação de camadas e fraturas, bem como a identificação de processos de criação de porosidade secundária nos carbonatos.

Os dados de petrofísica de rotina de laboratório (*routine core analysis, RCAL*) compreendem densidade do grão (*grain density*), porosidade e permeabilidade obtidas com porosímetro e permeâmetro, respectivamente.

A determinação das fácies sedimentares em escala de perfil (*log facies*), foi feita a partir da correlação entre as características encontradas nos perfis de imagem e a descrição de litofácies obtidas na descrição das rochas (testemunhos, plugues, amostras laterais). Adicionalmente foi utilizada a descrição das amostras de calhas fornecida nos relatórios e perfis compostos da ANP, quando coerentes com as descrições dos demais dados de rochas, e com correto posicionamento considerando a diferença de entre a profundidade *logging while drilling* (LWD) com a profundidade de referência a cabo (*wireline*)

Por fim, a interpretação dos resultados foi suportada por correlações com estudos análogos realizados na Bacia de Santos (e.g., Faria *et al*., 2017; Farias *et al*., 2019; Gomes *et al*., 2020; Valle *et al*., 2021).

Nas próximas seções são descritos os métodos utilizados para o estudo realizado.

2.5.1 Difração de raios-X

A caracterização da mineralógica dos principais constituintes de rochas carbonáticas nessa pesquisa foi realizada por meio de dados de difração de raios-X.

O princípio do método baseia-se no fato de que cada substância cristalina possui sua estrutura atômica própria, a qual difrata raios-X emitidos na amostra analisada (total ou em uma fração granulométrica).

A difração de raios-X pelos cristais resulta de um processo em que os raios são espalhados pelos elétrons dos átomos da estrutura cristalina, sem mudanças de comprimento de onda. Um feixe difratado é produzido por espalhamento em condições geométricas de interferência construtiva, expressas pela lei de Bragg (Jenkins e Snyder, 2012; Dowsett *et al*., 2021). Após a colisão há mudança da direção de propagação dos raio-X, mas com a conservação do comprimento de onda incidente (Jenkins e Snyder, 2012).

A expressão matemática da lei de Bragg é descrita:

$$n\lambda = 2dsen\theta$$

Onde n é um número inteiro, λ é o comprimento de onda, d é a distância entre os planos paralelos sucessivos na estrutura cristalina, e ∅ representa o ângulo de incidência e difração de um feixe de raios-X relativamente a um dado plano atômico (Jenkins e Snyder, 2012; Dowsett *et al*., 2021).

O resultado deste tipo de análise é apresentado sob a forma gráfica, chamado de difratograma (FIGURA 12), cujas variáveis são o ângulo 2θ (eixo horizontal) e a intensidade dos picos difratados (eixo vertical). Os picos do difratograma são produzidos quando, para um dado valor de θ, um dado plano atômico possui distância interplanar (d) que satisfaz a lei de Bragg.

FIGURA 12 – REPRESENTAÇÃO DO DIFRATOGRAMA
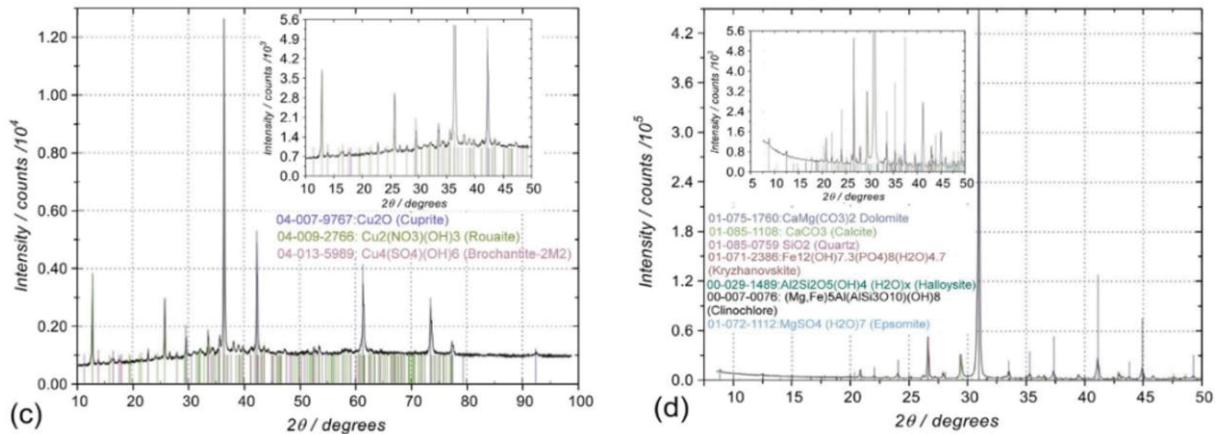
FONTE: Dowsett *et al*., (2021).

Por fim, as alturas dos picos são proporcionais às intensidades dos efeitos da difração, de forma semi-quantitativa para a estimativa volumétrica dos diferentes minerais nas amostras avaliadas.

2.5.2 Petrofísica de rotina de laboratório

A petrofísica de rotina de laboratório compreende ensaios laboratoriais para a determinação das propriedades de densidade do grão (*grain density*), porosidade e permeabilidade obtidas com porosímetro e permeâmetro, respectivamente.

Primeiramente os materiais rochosos são limpos para garantir a remoção completa dos fluidos do reservatório (e.g., hidrocarbonetos, sais, fluidos de perfuração), o processo de limpeza é realizado com solventes, podendo ser feito pela extração contínua, e desassistida empregando extratores Soxhlet, método Dean Stark ou limpeza de fluxo (Rios *et al.,* 2012). A água conata é extraída com metanol e os hidrocarbonetos são removidos com produtos como o tolueno ou clorofórmio (API., 1998; Rios *et al*., 2012). A total remoção de resíduos salinos é confirmada através de teste químico com nitrato de prata quando não há ocorrência de precipitação de cloreto de prata (API., 1998).

Após a limpeza, os plugues e amostras laterais são colocados em estufas especiais até que estejam totalmente secos. Caso esses, possuam argilominerais, mais comum em arenitos, são submetidos a estufas especiais com umidade

controlada, isso para que a água estrutural da argila não seque e danifique sua estrutura laminar (API., 1998). Por fim, as amostras submetidas a esse processo são resfriadas sob vácuo em secadores para evitar absorção de umidade do ar. Os ensaios de petrofísica básica ocorrem nos equipamentos porosímetro e permeâmetro de expansão a gás hélio ou gás nitrogênio.

Conforme descrito por Schön (2015), a porosidade (∅) é calculada pela razão do volume de poros (V_{pore}) pelo volume da amostra (V_{bulk}) medidos, aplicação direta da lei de Boyle. O volume de poros é o volume da amostra, desconsiderando o dos componentes minerais sólidos (V_{solid}).

$$\emptyset = \frac{Vpore}{Vbulk} = \frac{Vbulk - Vsolid}{Vbulk}$$

No porosímetro, o gás preenche a linha do equipamento e uma pequena câmara interna de referência, cuja soma dos volumes iniciais ($V_{inicial}$) e a pressão inicial (Pi_{nicial}). De acordo com Rios *et al.* (2012), assim que a pressão se estabiliza, o gás se expande isotermicamente para uma segunda câmara de volume conhecido, dentro da qual a amostra se encontra. A pressão final (P_{final}) do sistema é reduzida na mesma proporção em que o volume ocupado pelo gás aumenta (V_{final}).

A densidade de grãos ou massa específica (ρ_m) é obtido pela razão entre a massa seca e volume de sólidos (Schön, 2015; Tiab e Donaldson, 2016). O porosímetro mede somente a porosidade efetiva uma vez que o gás não atinge os poros não conectados (Rios *et al.*, 2012).

No permeâmetro, o gás atravessa a amostra confinada no equipamento. Para a realização do experimento, o controle da vazão do gás é realizado manualmente por válvulas de alta e baixa pressão contidas no módulo do equipamento (FIGURA 13).

FIGURA 13 – REPRESENTAÇÃO ESQUEMÁTICA DE UM PERMEÂMETRO
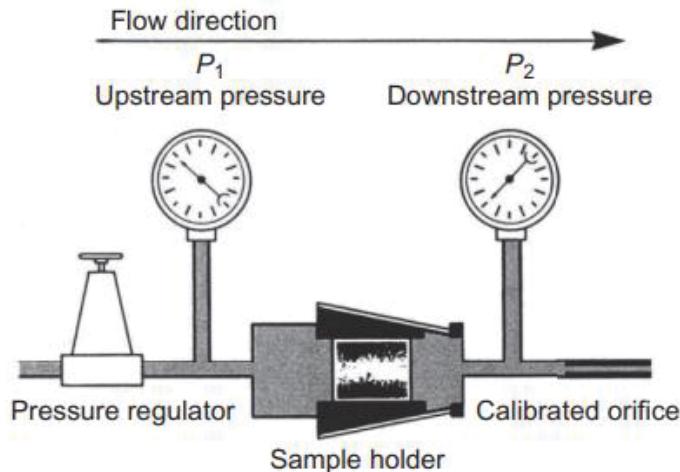
FONTE: Tiab e Donaldson (2016).

Conforme descrito por Tiab e Donaldson (2016), os fluxômetros e transdutores de pressão são calibrados, e a vazão (Q) e o diferencial de pressão do gás (ΔP) são quantificados durante um fluxo estável e não compressível. Dessa forma, emprega-se a lei de Darcy para o cálculo da permeabilidade absoluta ao gás, tal que:

$$K = \frac{-\mu Q L}{A \Delta P}$$

Em que μ é a viscosidade dinâmica; L o comprimento e A, a área da seção transversal do plugue (Tiab & Donaldson, 2016).

As medidas de rotina são realizadas em todos os plugues, e as informações são imediatamente utilizadas para uma primeira determinação da qualidade da rocha reservatório, verificação ou calibração de alguns perfis e para seleção de amostras para petrofísica especial (Rios *et al.*, 2012; Tiab & Donaldson, 2016).

Segundo Rios *et al.* (2012), os resultados de petrofísica básica são geralmente disponibilizados a tempo de serem considerados para tomada de decisão de testes de formação com coluna, completação, canhoneio ou abandono de poço.

2.5.3 Perfilagem

Os dados de perfis dos poços são uma das maiores fontes de informações geológicas usadas para reduzir as incertezas na caracterização geológica e petrofísica de reservatórios em subsuperfície, e auxiliam a avaliação de formação. Esses perfis registram informações dos reservatórios de forma indireta, sem a dependência da coleta de amostras de rochas.

Uma avaliação completa dos carbonatos do Pré-Sal inclui registros como raios gama, raios gama espectral, densidade, porosidade de nêutrons, ressonância magnética nuclear, perfil sônico (vagarosidade acústica), registro de imagem de poço (acústica e resistiva) e testadores de formação a cabo (Alabi *et al.*, 2014; Chitale *et al.*, 2014 e Boyd *et al.*, 2015). A aquisição dos perfis pode ser feita a partir de perfilagem a cabo ou durante a perfuração. Nos reservatórios carbonáticos do Pré-Sal são normalmente adquiridas ambas as informações, sendo os registros a cabo mais completos, compreendendo toda a seção entre base da Formação Ariri até o fundo do poço.

Os perfis de raios gama naturais e os espectrais exploram a interação da colisão de nêutrons e átomos para construir um espectro de energia. O perfil de raios gama espectral, possui um espectro resultante que é então decomposto em frações de potássio (GRKT), tório (GRTH) e urânio (GRKUT) em frações elementares (geoquímicas), registrados por sensores das ferramentas a cabo (Ellis & Singer, 2007; Rider, 2011). Dentre os principais usos, destacam-se as correlações estratigráficas, quantificação do conteúdo de potássio, tório e urânio, e frações elementar de elementos químicos (e.g., cálcio, silício, magnésio) para construção de modelos mineralógicos (e.g., calcita, quartzo e dolomita) a partir da fração elementar.

Dentre o conjunto de perfis mais frequentemente adquiridos em perfilagem de poço aberto, destacam-se os do conjunto básico, que compreendem os perfis de resistividade, densidade (RHOB), porosidade nêutron (NPHI), fator fotoelétrico (PE) e perfil sônico (vagarosidade acústica compressional, DTC).

Os dados de resistividade profunda e rasa são adquiridos a partir de ferramentas *dual-laterolog*, com um sistema de foco duplo que permite que a corrente elétrica penetre a formação superficial (RT20) e profundamente (RT90)

(Ellis & Singer, 2007; Rider, 2011) geralmente usadas em poços com fluido de perfuração a base água. Adicionalmente as ferramentas de resistividade de indução *multi-array* (Ellis & Singer, 2007; Rider, 2011), comumente usados em fluido de perfuração base óleo.

A ferramenta de densidade mede a dispersão/espalhamento Compton e a absorção de colisões de elétrons, cujos resultados são valores de densidade e o fator fotoelétrico (Ellis & Singer, 2007; Rider, 2011). Adicionalmente, a porosidade do neutrôn, medida pela fonte de energia térmica / nêutrons rápidos (*fast neutron*).

Os perfis acústicos são registros que medem a vagarosidade das ondas de compresionais (primeira chegada*, compressional wave*), cisalhamento (segunda chegada, *shear wave*) e stoneley (terceira chegada) (Ellis & Singer, 2007).

O perfil de ressonância magnética nuclear oferece informações sobre o preenchimento do espaço poroso independentemente da constituição mineral da rocha (Coates *et al*., 1999). As porosidades medidas são divididas em partições de porosidade definidas como *bound* (capilar e argila), fluido livre, e porosidade total, a partir da distribuição T2 e/ou T1. Os dados utilizados nessa pesquisa foram adquiridos a partir da ativação simultânea T1-T2 da aquisição do perfil de NMR, que fornece informações valiosas sobre a difusão de fluidos móveis encontrados no reservatório. (Coates *et al*., 1999). O perfil de permeabilidade pode ser extraído pela equação de Timur-Coates, a partir da distribuição T2 (Coates *et al*., 1999). Por fim, o perfil de NMR permite cálculo de saturação de água, em que as medidas de resistividade da formação é necessária (Coates *et al*., 1999 e Ehigie, 2010).

O registro de perfis de imagem do poço (BHI) apresenta a imagem da parede do poço aberto, sendo utilizado principalmente para a identificação de litofácies, delimitação e orientação de estruturas geológicas (camadas, limite de sequências, fraturas naturais ou induzidas), informações petrofísicas e diagenéticas (porosidade vugular, zonas fechadas), e correlação estratigráfica conforme a FIGURA 14 (Muniz & Bosence, 2015, 2018; Lai *et al*., 2017, 2018; Li *et al*., 2020; Makeen *et al*., 2021; Fan *et al*., 2021). Os perfis de parede de imagem de poço são reconstruídos pelo contraste de resistividade (imagem resistiva), ou amplitude de tempo de trânsito (imagem acústica) de uma fonte de onda acústica (Lai *et al*., 2018).

FIGURA 14 – PERFIL COMPOSTO DO POÇO 20, BACIA DE CAMPOS
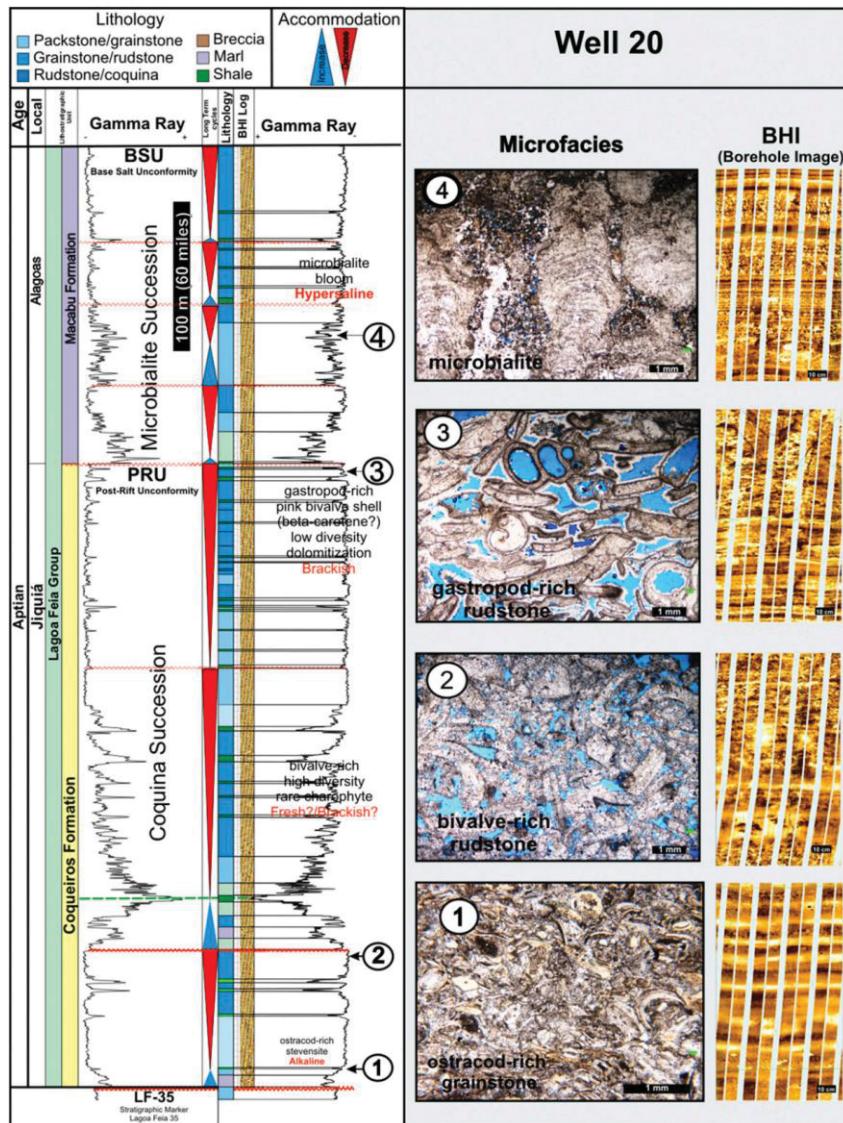
FONTE: Muniz e Bosence (2018).

LEGENDA: Perfil composto com raio gama, fotomicrografias e perfil de imagem (BHI) resistiva, das Formações Coqueiros e Macabú, Pré-Sal da Bacia de Campos, mostrando a correlação dessas informações. A Formação Macabú da Bacia de Campos é análoga a Formação Barra Velha da Bacia de Santos.

2.5.4 Avaliação petrofísica nos carbonatos do Pré-Sal

Poucos estudos e exemplos sobre a avaliação petrofísica baseadas em perfilagem foram publicados e divulgados sobre os carbonatos do Pré-Sal. Petersohn & Abelha (2013) em relatório técnico da ANP mostraram um exemplo de perfil composto para o poço 2-ANP-2A-RJS (FIGURA 15), no campo de Libra na

Bacia de Santos, no qual é possível identificar a delimitação da camada base do sal da Formação Ariri (*Base of Salt*), topo da seção rifte (*top of upper rift*), topo da camada das coquinas (*top of coquinas*) e contato óleo-água (*oil/water contact*), juntamente com os perfis de raios gama, resistividade, densidade, porosidade nêutron, vagarosidade compresional, ressonância nuclear magnética e distribuição T2, os triângulos vermelhos não foram identificados pelas autoras. Segundo esse relatório, o poço apresenta saturação de óleo de 82.7%.

FIGURA 15 – PERFIL COMPOSTO DO POÇO 2-ANP-2A-RJS. CAMPO DE LIBRA, BACIA DE SANTOS
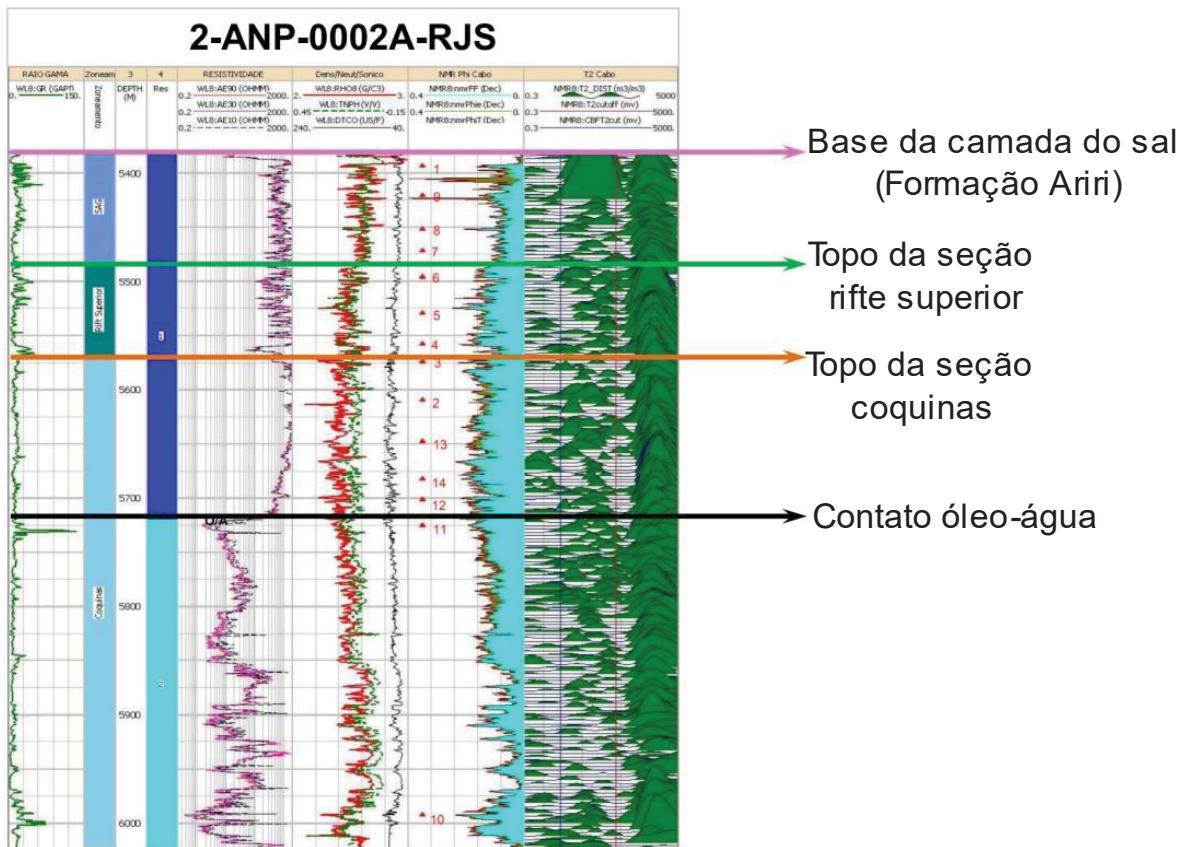
FONTE: Petersohn e Abelha (2013).

LEGENDA: Perfil composto com curvas de raio gama, resistividade, densidade, porosidade nêutron, vagarosidade compresional, ressonância nuclear magnética e distribuição T2. Na figura são mostradas a delimitação da base da camada do sal, Formação Ariri (*Base of Salt*), topo da seção rifte (*top of upper rift*), topo da camada das coquinas (*top of coquinas*) e contato óleo-água (*oil/water contact*) foram identificados (Petersohn e Abelha, 2013), os triângulos vermelhos não foram identificados pelas autoras.

Boyd *et al.* (2015) propuseram um fluxograma de avaliação baseado em 3 principais etapas:

1. determinação de litologia e porosidade, a partir do uso de perfis de densidade, fator fotoelétrico, porosidade nêutron, NMR e espectroscopia de raios gama;

2. partição de porosidade de determinação de permeabilidade, a partir dos perfis de NMR, imagem de poço, perfil sônico e testadores de formação a cabo;

3. análise de saturação de fluido, como o uso integrado de perfis de resistividade, NMR e dielétrico (se disponível).

Brelaz *et al*. (2019) publicaram a avaliação de parâmetros petrofísicos de um poço exploratório 1-RJS-628 (1-BRSA-369A-RJS), situado no Campo de Lula, na sucessão pós-rifte transicional da Bacia de Santos, com base na interpretação do perfil do poço que inclui perfis básicos de poço (gama, caliper, porosidade nêutron, densidade, resistividade e perfil acústico) e registros especiais (ressonância nuclear magnética) (FIGURA 16). Segundo o estudo, a porosidade média encontrada foi de 6% a 7% atingindo até 23%, a resistividade profunda foi superior a 100 ohm.m com um perfil de invasão expressivo. A saturação da água encontrada foi inferior a 45% e a saturação irredutível da água, inferior a 1%. A permeabilidade estimada foi considerada alta pelas autoras, com valores médios superiores a 3 mD atingindo até 1,7 D nas camadas vugulares e fraturadas.

FIGURA 16 – EXEMPLO PERFIS DE RESSONÂNCIA NUCLEAR MAGNÉTICA E DISTRIBUIÇÃO
T2 E CURVAS DE POROSIDADE
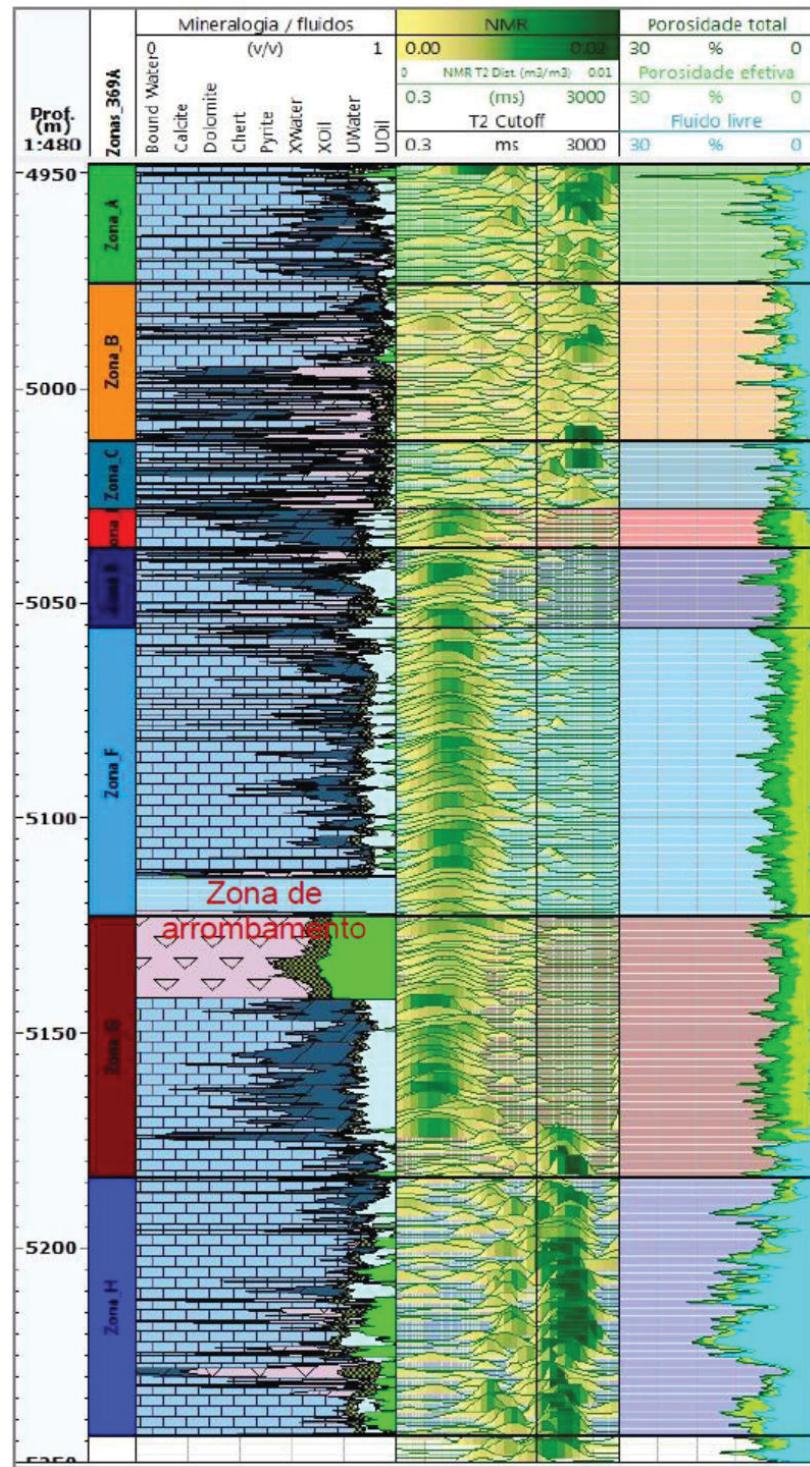
FONTE: Brelaz *et al*., (2019).

LEGENDA: Perfil composto do poço 1-RJS-628, campo de Lula, Bacia de Santos. No perfil composto
encontra-se as informações de profundidade, zonas, mineralogia/fluidos, distribuição T2 e curvas de
porosidade, definidos com essa nomenclatura pelas autoras.

3 RESULTADOS E DISCUSSÕES

Os resultados obtidos nessa pesquisa foram submetidos ao *journal AAPG Bulletin*.

M Gmail

Hugo Tamoto <hugotamoto@gmail.com>

A manuscript number has been assigned to Impacts of dissolution and diagenetic processes in formation evaluation of the Aptian Pre–Salt carbonates of the Santos Basin, Brazil.

1 mensagem

AAPG Bulletin <em@editorialmanager.com>
Responder a: AAPG Bulletin <bulletin@aapg.org>
Para: Hugo Tamoto <hugotamoto@gmail.com>

2 de abril de 2022 18:09

CC: "André Luiz Silva Pestilho" andre.pestilho@gmail.com, "Anelize Manuela Bahniuk Rumbelsperger" anelize.bahniuk@ufpr.br

Dear Tamoto,

Your submission entitled "Impacts of dissolution and diagenetic processes in formation evaluation of the Aptian Pre–Salt carbonates of the Santos Basin, Brazil." has been been assigned the following manuscript number: BLTN22-046.

You will be able to check on the progress of your paper by logging on to Editorial Manager as an author. The URL is https://www.editorialmanager.com/bltn/.

Thank you for submitting your work to this journal.

Kind regards,

AAPG Bulletin

In compliance with data protection regulations, you may request that we remove your personal registration details at any time. (Use the following URL: https://www.editorialmanager.com/bltn/login.asp?a=r). Please contact the publication office if you have any questions.

AAPG Bulletin

Impacts of dissolution and diagenetic processes in formation evaluation of the Aptian Pre–Salt carbonates of the Santos Basin, Brazil.

--Manuscript Draft--

Manuscript Number:	
Full Title:	Impacts of dissolution and diagenetic processes in formation evaluation of the Aptian Pre–Salt carbonates of the Santos Basin, Brazil.
Article Type:	Article
Manuscript Classifications:	Carbonates; Diagenesis; Log Analysis; Petrophysics; Porosity; Reservoir Characterization/Appraisal
Author Comments:	
Corresponding Author:	Hugo Tamoto
	Rio de Janeiro, Rio de Janeiro BRAZIL
Corresponding Author Secondary Information:	
Corresponding Author's Institution:	
Corresponding Author's Secondary Institution:	
First Author:	Hugo Tamoto
First Author Secondary Information:	
Order of Authors:	Hugo Tamoto
	André Luiz Silva Pestilho, Dsc.
	Anelize Manuela Bahniuk Rumbelsperger, Dsc.

3.1 MANUSCRITO (MANUSCRIPT)

Impacts of diagenetic processes in formation evaluation of the Pre–Salt carbonates reservoir of the Barra Velha Formation

Abstract

The Pre–Salt succession located at the marginal basins of Brazil are one among the most important hydrocarbon reservoirs found worldwide. These reservoirs are responsible for approximately 75% of the Brazilian offshore oil production. Despite the excellent reservoir qualities (reaching porosities > 15 % and permeability > 100 mD) found in the Pre–Salt reservoirs, there are still challenges related to the lack of understanding on the petrophysical controls. This situation is resultant from a complex depositional and diagenetic history of the carbonate rocks. To address such problems, an overall petrophysical evaluation of the carbonate section of the Aptian Barra Velha Formation in the Sapinhoá field, Santos Basin is provided. This was done by using an extensive dataset of well–logging, petrophysics, and X–ray diffraction. The results allowed the identification of facies heterogeneities and variated petrophysical distribution, which characterizes five hydraulic flow units. Overall, the best petrophysical intervals (i.e., highest porosity and permeability) are found in the wells located at the structural high and comprise the flow units 4 and 5, that mostly consist of Shrub-rich facies and grainstones. These are followed by the intermediary flow unit 3 found in all wells, comprised of shrubs–rich facies, spherulitite–rich facies, grainstones, packstones, and laminites. Moreover, among all units, the flow units 1 and 2 presented the lowest petrophysical features and are mainly found in wells located at the basinward area of the Sapinhoá field. Finally, the results indicate that key diagenetic features, such as the dissolution of clay mineral, and dolomitization, are notable elements that commonly enhanced the petrophysical properties. Additionally, the pervasive silicification process decrease the reservoir quality. These processes are often found in the wells located at both the structural high and the basinward area of the Sapinhoá field.

Keywords: Pre–Salt; Carbonate petrophysics; Formation evaluation; Santos Basin.

3.2 INTRODUCTION

The Santos Basin (FIGURE 17) host some of the giant oil fields of the Brazilian Pre–Salt (Carminatti et al., 2008). The Pre–Salt comprises carbonate reservoirs located on top of structural highs (Zalán et al., 2019) and underneath an extensive sequence of evaporites (Moreira et al., 2007). Despite these reservoirs have been under exploration for more than a decade, its complex depositional and diagenetic history (Rezende & Pope, 2015) still challenges both exploration and production forecast due to its complex and heterogeneous network of pores and flow regimes (Mohriak et al., 2015). One key problem arises from the lack of understanding of the impact of the diagenesis on the reservoir quality and in the petrophysical evaluation of the carbonates facies (Worden et al., 2018). Therefore, in this article, we evaluate the impact of silicification, dolomitization and dissolution effects in the main reservoir interval of the Pre–Salt, the Aptian Barra Velha Formation, at the Sapinhoá field.

The Pre–Salt carbonates encompasses the Barremian–Aptian Itapema Formation and the Aptian Barra Velha Formation (Moreira et al., 2007). The sedimentary facies of the Barra Velha Formation (BVF) can be divided into two major groups, such as the depositional in situ carbonates, and carbonates from the reworking of previous depositional components (Gomes et al., 2020), which have been interpreted as deposited in a lacustrine system (Wright & Barnett, 2015; Tosca & Wright, 2018; Farias et al., 2019; Gomes et al., 2020; Wright, 2020). Carbonate facies are composed of heterogeneous textures, differing in grain size, sorting, packing and morphology. Its pore system is the product of a long depositional and diagenetic history (Rezende & Pope 2015).

Although several studies have described the BVF's facies (Wright & Barnett, 2015; Tosca and Wright, 2018; Farias et al., 2019; Gomes et al., 2020; Wright, 2020) at thin section scale, few publications explored the effects of dissolution, silicification and dolomitization processes in petrophysics characterization (Rezende & Pope, 2015; Herlinger et al., 2017; Lima & De Ros, 2019; Herlinger et al., 2020), mostly limited to petrography characterization; and these studies have not addressed the petrophysical impacts at formation evaluation in well–logging scale. Therefore, to better describe how this heterogeneous type of features impacts the reservoir quality,

an integrated multiscale overview is presented, which allow us to characterize the key features that impact the porosity and permeability properties.

Aiming to assess the quantitative and qualitative impact of diagenetic processes at field scale, we selected a set of wells, positioned along the main SW–NE structure of the reservoir, correspondent to the structural high and basinward area (Zalán et al., 2019), within the Sapinhoá field (FIGURE 17A).

FIGURE 17 – LOCATION OF THE SAPINHOÁ FIELD AND THE STUDIED WELLS WITHIN THE SANTOS BASIN, BRAZIL, AND SIMPLIFIED STRATIGRAPHIC CHART OF THE SANTOS BASIN
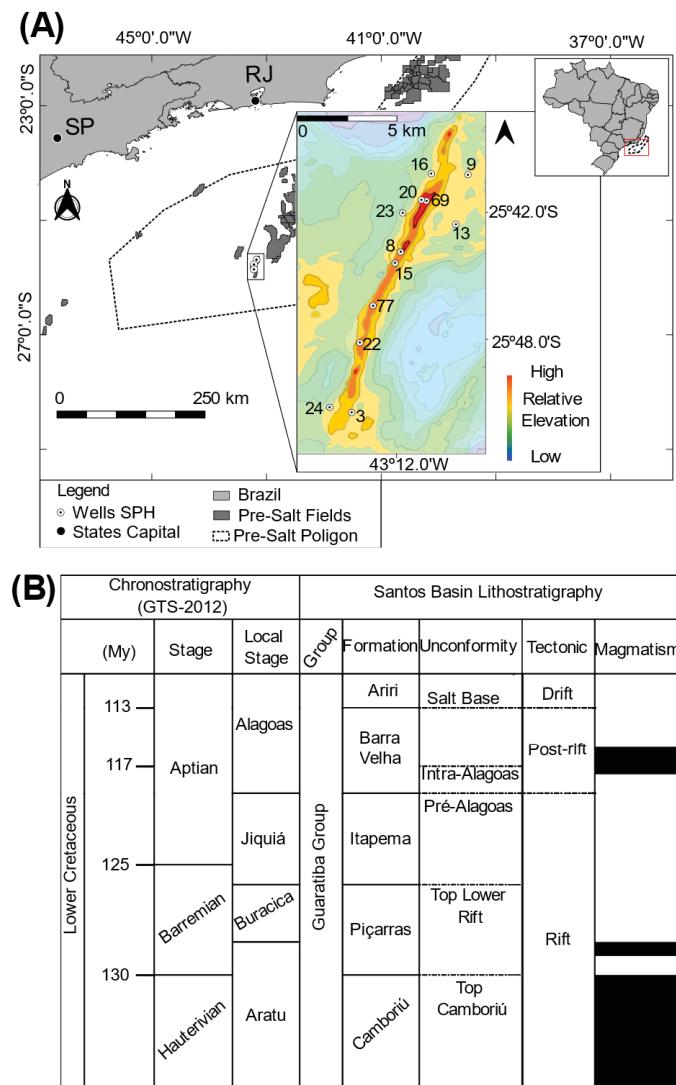
Source: The author (2022).

Caption: A) Location of the Sapinhoá field and the studied wells within the Santos Basin, Brazil; B) Simplified stratigraphic chart of the Lower Cretaceous geological units in the Santos Basin. The Barra Velha Formation is limited by both the Pre–Alagoas and the Salt Base unconformities, and it is divided by the Intra–Alagoas Unconformity in two different intervals: the Lower and Upper Barra Velha Formation. Based in Moreira et al., (2007) and Wright (2020).

3.3 GEOLOGICAL SETTING

The Santos Basin is an offshore sedimentary basin located in southeastern Brazil, with an area of about 352,000 km^2, limited between the Campos Basin at North and the Pelotas Basin at South (Moreira et al., 2007). The Santos Basin is part of the East Brazil Rift System and was originated during the Lower Cretaceous tectonic break–up of the Gondwana Supercontinent and the opening of the South Atlantic Ocean (Chang et al., 1992). The sedimentary succession of the Santos Basin lies over the Precambrian basement, and is divided into three super–sequences: Rift, Post–Rift, and Drift (FIGURE 17B) (Moreira et al., 2007).

During the early rifting process a sequence of tholeiitic flood basalts of the Camboriú Formation was formed. These were followed by the deposition of siliciclastic facies (conglomerate, sandstone, and shale) of the Piçarras Formation (Moreira et al., 2007), and by interbedded lacustrine coquina and organic-rich limestones from the Itapema Formation (Moreira et al., 2007).

The Aptian Post–Rift sedimentary succession includes the carbonates of the BVF and the evaporites of the Ariri Formation (Moreira et al., 2007). The carbonate of BVF are composed of fine–grained components as microcrystalline calcite and clay minerals, spherulite calcites and fascicular optic calcite (shrubs) (Wright & Barnett, 2015 and Gomes et al., 2020). Recently, the shrub–rich carbonate facies were interpreted to have formed by chemical precipitation processes, with low microbial contribution (Wright & Barnett, 2015; Farias et al., 2019; Gomes et al., 2020).

Carbonate facies also comprehends packstones, grainstones and rudstones, composed of reworked shrubs and spherulites. These carbonates have been reported in previous publications in the Pre-Salt area (e.g., Faria et al., 2017; Lima and De Ros 2019., Gomes et al., 2020). These rocks are described based on Dunham (1962), Embry and Klovan (1971), and Terra et al., (2010) classifications.

Gomes et al. (2020) highlighted three major unconformities in the BVF. The first one is found at top of coquinas succession, the Pre–Alagoas Unconformity (PAU); the second is recognized within the BVF, called the Intra–Alagoas Unconformity (IAU) (Wright & Barnett, 2015; Gomes et al., 2020); and, the last is the Salt–Base Unconformity (SBU), above the Upper Barra Velha Formation (UBVF).

After the Post–Rift phase, the Santos Basin evolved into a passive–margin basin. The Drift succession is represented by the early shallow–marine carbonate

platform of the Guarujá Formation, followed by marine transgression and deposition of the deep–water sediments of the Itanhaém Formation (Moreira et al., 2007; Gomes et al., 2020).

3.4 MATERIALS AND METHODS

Dataset of 12 wells of the Sapinhoá field were obtained through the request 48610.207805/2021–63 of the 757/2018 resolution, provided by the National Agency of Petroleum, Natural Gas and Biofuels (Agência Nacional do Petróleo, Gás Natural e Biocombustíveis – ANP). The study focused only in the BVF, limited to the stratigraphical interval below the base of the Ariri Formation and above the Pre–Alagoas unconformity (FIGURE 18). The data includes well–logging, cores, core–plugs, side–wall cores (SWC) and thin sections. Lastly, the whole–core gamma–ray log was used for correlation with well–logs.

Two wells in the structure high (SPS–69 and SPS–77) have the complete dataset available, including well–logs, cores, core–plugs, and SWC samples. The remaining ten wells only had data from well–logging and SWC samples, from which three wells (SPH–9, SPH–16, and SPH–22) had only well–logging data.

FIGURE 18 – DATASET DISTRIBUTION WITHIN THE BARRA VELHA FORMATION
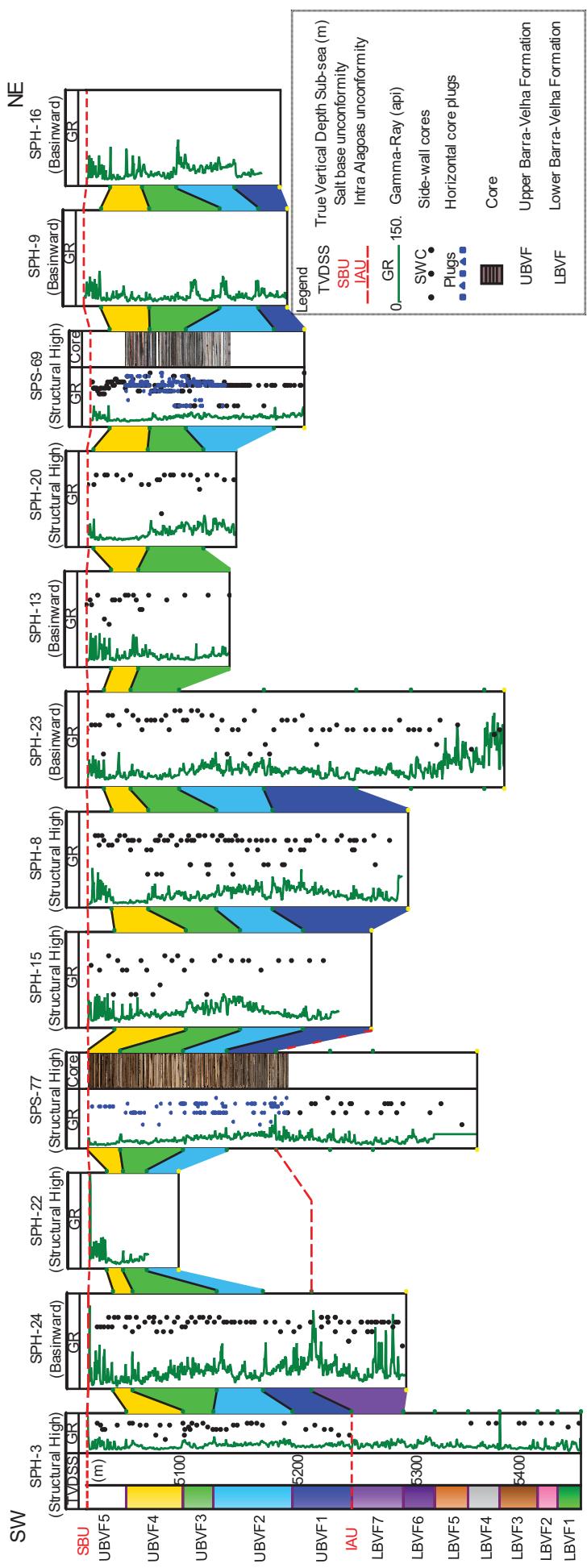
Caption: Dataset distribution within the Barra Velha Formation (BVF) for the well located at the structural high and basinward area, following the SW–NE direction of the Sapinhoá field. The Gamma–ray (GR) logs are plotted as a reference to the general well–logging data, and the correlations between the 12 wells are displayed within and the Upper and Lower BVF. The position of cores, core–plugs, and side–wall cores (SWC) are indicated alongside the GR logs to cross–references.

Source: The author (2022).

3.4.1 Well–logging and formation evaluation

A complete well–logging profile was used to perform the petrophysical analyses and facies correlation between whole–cores, core–plugs and SWC samples along the borehole wall extension. Initially, the data quality control was performed for each well–log. Noise readings mainly caused by wellbore rugosity and/or washout intervals were excluded from the petrophysical evaluation.

The spectral Gamma–ray (potassium, uranium, and thorium composition), neutron, density, photoelectric factor (PE), and resistivity well–logs were used for well correlations and to support petrophysical interpretations.

The borehole image wall logs (BHI), reconstructed by either the contrast of resistivity or amplitude of travel time from an acoustic wave source (Lai et al., 2018), allowed the identification of usual geological features as beddings, textures, natural fractures, discontinuities (e.g., induced fractures and borehole breakouts) and to compute the orientation of these imaged features (Lai et al., 2018; Williams et al., 2000). A complete quality control of resistivity and acoustic BHI logs was performed for all studied wells, including the navigation reconstruction, accelerometer and magnetometer quality check, and speed correction. The intervals with non–geological features, such as artifacts, wireline stretching, and data with issues of tools centralization were excluded from the analyses.

In addition, the BHI logs are used to constrain facies distribution of rock material and create representative log facies of borehole extension (Lai et al., 2018; Fan et al., 2021). In this study, the acoustic image also aid to identify the degree of dissolution features, quantify vug density laminations and to evaluate the reservoir petrophysical quality in broad and narrow porosity zones in carbonates, as discussed by Bigelow (1993) and Lai et al., (2019).

The Nuclear Magnetic Resonance log (NMR) evaluation is an important tool to perform petrophysical analysis in carbonates (e.g., Boyd et al., 2015; Herlinger et al., 2020; Valle et al., 2021), due to the independence of influence from lithology composition. According to Coates et al. (1999), the NMR well–log T2 distribution enables to classify the pore size distribution and to quantify porosities fractions in effective, capillary water, and bound fluid porosities. Other applications of NMR data lie on the correlation and the calibration of permeability and porosity of well–logs with

petrophysical measurements of core–plugs (Coates et al., 1999), and with water saturation calculations, in which resistivity input is needed (Coates et al., 1999; Ehigie, 2010).

The NMR log porosities were computed through process inversion of T2 distribution spectrum (Coates et al., 1999). In the absence of the NMR rock samples to calibrate cut–offs, we choose to apply cut–offs from 3 and 100ms from clay bound and free fluid respectively, supported by previous NMR studies discussed for the Pre–Salt carbonates (Boyd et al., 2015; Herlinger & Dos Santos, 2018; Brelaz et al., 2019; Belila et al., 2020). Finally, NMR calculations as permeability and fluid saturation were performed through Magnetic Resonance Imaging Analysis (Coates et al., 1999) and by dual water model (Ehigie, 2010), respectively.

3.4.2 Petrographical review and X–ray diffraction

We evaluated the mineral composition and identified the Pre–Salt main facies through the review of 355 thin section microphotographies, available for horizontal core–plugs in the SPS–77A well, which is located in the first 200 m of UBVF. The XRD analyses information provided by ANP encompasses horizontal core–plugs of this well. These integrated analyses allowed to recognize the main and trace mineral assemblages and correlate them with mineral proportions of XRD results. In addition, this review allowed us to observe microfacies associations with minerals filling the pore spaces in the analyzed samples.

3.4.3 Routine core analysis

According to the ANP reports, the samples were cleaned through solvent extraction with toluene to complete removal of oil and residual organic matter from the porous media prior to the porosimeter and permeameter analyses. The Routine core analysis (RCAL) included grain density, gas porosity ($\emptyset_{gas}$), and absolute permeability (K_{abs}) measurements from 758 SWC.

To evaluate the contribution of each facies in rock–typing analysis, hydraulic flow units (HFU) were calculated using the methodology presented by Amaefule et al.

(1993), where flow zone indicator (FZI), normalized porosity index (NPI), and reservoir quality index (RQI) are used:

$$FZI = \frac{RQI}{NPI} \qquad (1)$$

$$NPI = \frac{Øgas}{1-Øgas} \qquad (2)$$

$$RQI = 0.0314 \sqrt{Kabs/Øgas} \qquad (3)$$

The FZI is a standard methodology used in petrophysical evaluation to classify and correlate flow behavior with petrophysical properties (e.g., Baouche et al., 2021; Penna and Lupinacci, 2020; Radwan et al., 2021), and additionally incorporates geological features (i.e., mineralogy) in the partition of distinct pore geometrical facies, described as hydraulic flow units (Amaefule et al., 1993).

3.4.4   Principal components analysis

The normalized Principal Component Analysis (PCA) were performed using XRD and RCAL dataset to investigate linear relations of the mineral assemblies with the petrophysical properties at core–plugs scale. The results were visualized using linear transformation proposed by Koren and Carmel (2003), applied to multivariate data in low dimensional space, which allowed us to set statistical mineral associations with petrophysical properties. The benefit of using the normalized PCA is that there is an incorporation of the dissimilarity relationships between analyzed elements, and also the preservation of the best overall structure of the data set in the projection (Koren and Carmel, 2003). The normalized PCA was implemented through python language using orange library (Demšar et al., 2013) and scikit–learn package (Pedregosa et al., 2011).

The results of PCA workflow provide the principal components (PC), which describe the variance of the dataset. An additional result obtained, is the correlation coefficient between the used data and the principal components (loadings) that can

be used to quantitatively describe the relationship between variables analyzed and the total variance in the dataset (Hemenway & Kaczmarek, 2021).

3.5 RESULTS

3.5.1 Well–log characteristics

The BVF was divided into two major intervals, the lower Barra Velha (LBVF) and the upper Barra Velha (UBVF). The BVF is bounded by the Pre-Alagoas unconformity at base and the base of the salt succession at top. The boundary between the LBVF and the UBVF contains the Intra-Alagoas unconformity. We individualized zones in the BVF according to distinctive well–logging patterns presenting the main features of each zone (FIGURE 18 and FIGURE 19). The main characteristics of the BVF succession and the identified zones are as follow:

(i)   We identified the LBVF only in the SPS–77, SPH–3, SPH–24 and SPH–23 wells. Seven zones (LBVF1–7) were defined based on the GR, GRKUT, RHOB, NPHI, PE, NMR and BHI logs. In addition, the LBVF well-log patterns resemble the UBVF–1 until it reaches the Pre–Alagoas unconformity.

(ii)   The first zone of the UBVF interval is the UBVF–1. In general, this zone presents bound fluid porosities 10% higher than the readings found in UBVF 2–3. Additionally, we noticed the presence of a minor proportion of the clay bound fluid porosity, reaching maximum of 2% of total NMR. Finally, at the bottom of this zone, we interpreted the Intra–Alagoas unconformity, based in gamma–ray log spike (FIGURE 19), similar as published by Gomes et al. (2020).

(iii)   The UBVF–2 zone present significant increase of bound porosity as observed in the NMR, usually reaching 6% more than the other zones UBVF interval. Despite that, this zone presented 10–20% of free fluid porosity. In addition, we observed similar vug porosity distribution as that found in the UBVF–4.

(iv)   The UBVF–3 zone presented a similar pattern of well–log readings found in the UBVF–2. However, we choose to individualize in different zones due to a distinct

pattern consistently found in the NMR porosities and PE well–logs. In these features, reduction of values in NMR and PE logs are noticed, which is opposite to the density log behavior observed in FIGURE 19 (i.e., red shading cross over between RHOB and PE curves).

(v)   In general, the UBVF–4 zone presents a flat format in the gamma, resistivity, and density matrix well–logs are noticed. This interval also shows significant porosity readings, in which the total NMR log easily reaches 15–20% and free fluid porosity 10–15%. Additionally, it is observed that from this zone, the bound fluid porosity values started to increase towards to the bottom of the well. The bedding features seen in the acoustic BHI logs showed isolated and connected vug features, alternating with high and low values of impedance.

(vi)   The UBVF–5 is characterized by a distinguished gamma–ray log pattern of seven to nine spikes, below the Salt–base unconformity, known as Lula's fingers, (i.e., an important and regional stratigraphic marker found in the Santos Basin). In addition, the UBVF–5 also presents spike patterns in the resistivity, density, photoelectric factor, and NMR well–logs. Lasty, in this zone the bedding features seen in BHI logs commonly presented contrasting features, alternating between high and low values of resistivities and acoustic impedance.

FIGURE 19 – COMPOSITE WELL–LOG CORRELATION OF SPH20–SPS69 WELLS
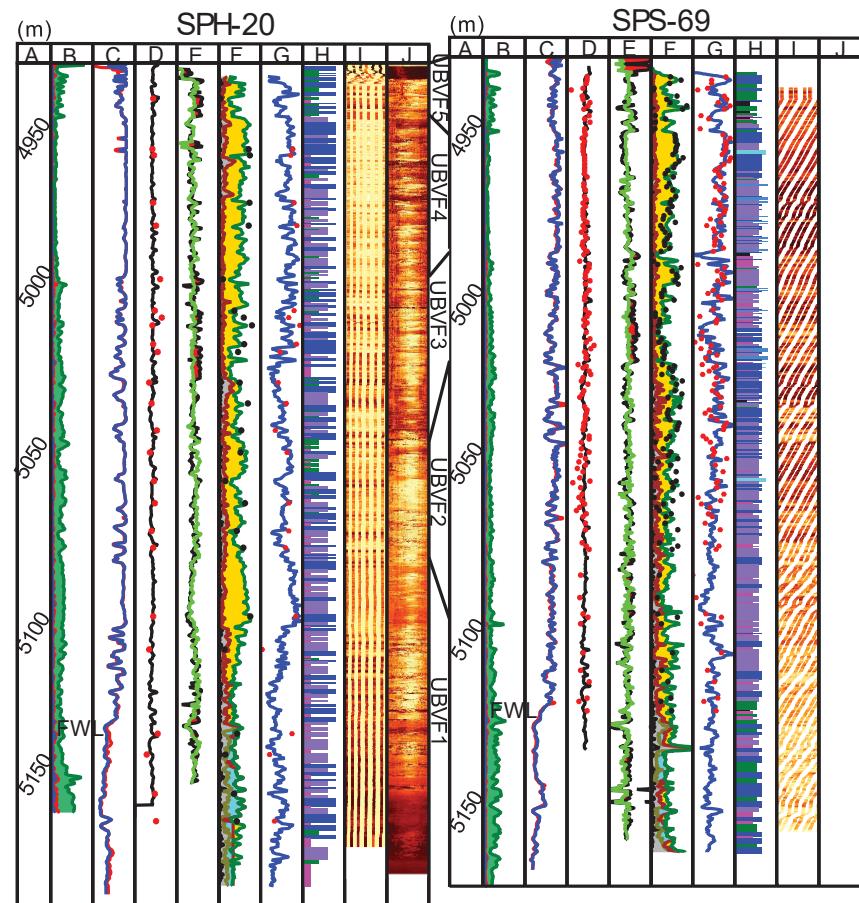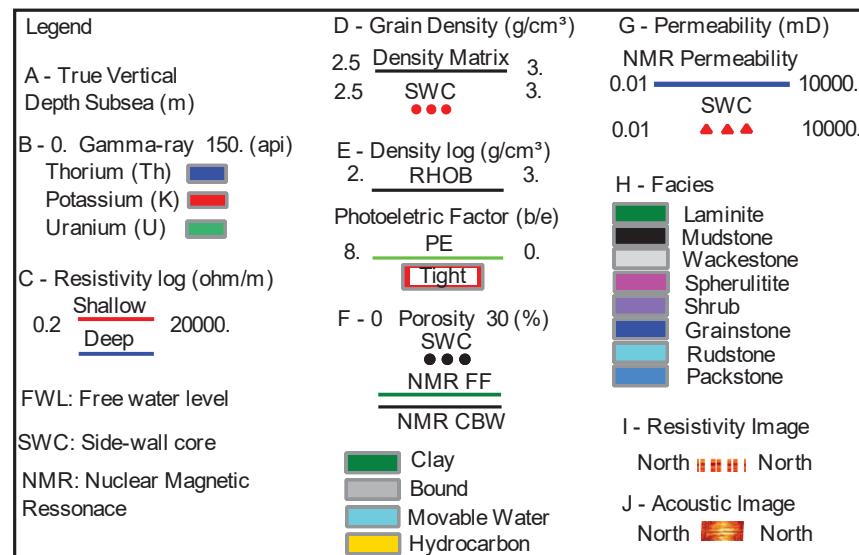
Source: The author (2022).

Caption: Well–logging correlation of the Barra Velha Formation units for SPH20–SPS69 wells, presenting the spectral gamma–ray (KUT). Resistivity well-logs and the free water level (FWL). Density grain (Density) of side–wall cores (SWC) and density matrix from logs (ROMA). Density–log (RHOB) and photoelectric (PE). Nuclear magnetic resonance (NMR) well-logs for free fluid (FF), clay-bound water (CBW), total porosity, and gas porosity ($\varnothing_{gas}$) of sidewall cores (SWC) black circles. NMR

Timur permeability log (NMRPerm) and the absolute permeability measurements (K_{abs}) from SWC as red triangle. Well–log facies. Acoustic and resistivity borehole image logs, respectively.

3.5.2 The Pre–Salt facies in multiscale

Millimeter to meter scale alternations between shrub-rich facies, spherulitites, laminites and coarse-grained facies product of reworking dominates in the BVF. (Wright & Barnett, 2015; Farias et al., 2019; Lima & De Ros, 2019). This association is also described in the African Pre–Salt carbonates (Sabato Ceraldi & Green, 2017). These facies examples are summarized in micrographies (FIGURE 20 and FIGURE 21), cores and SWC photographies, and BHI logs (FIGURE 21 and FIGURE 22). The comparison between these data allowed us to create a representative log–facies framework, constrained by BHI logs, capable of integrating the facies information reaching the well–log scale.

FIGURE 20 – EXEMPLE OF THE MAIN CARBONATE FACIES
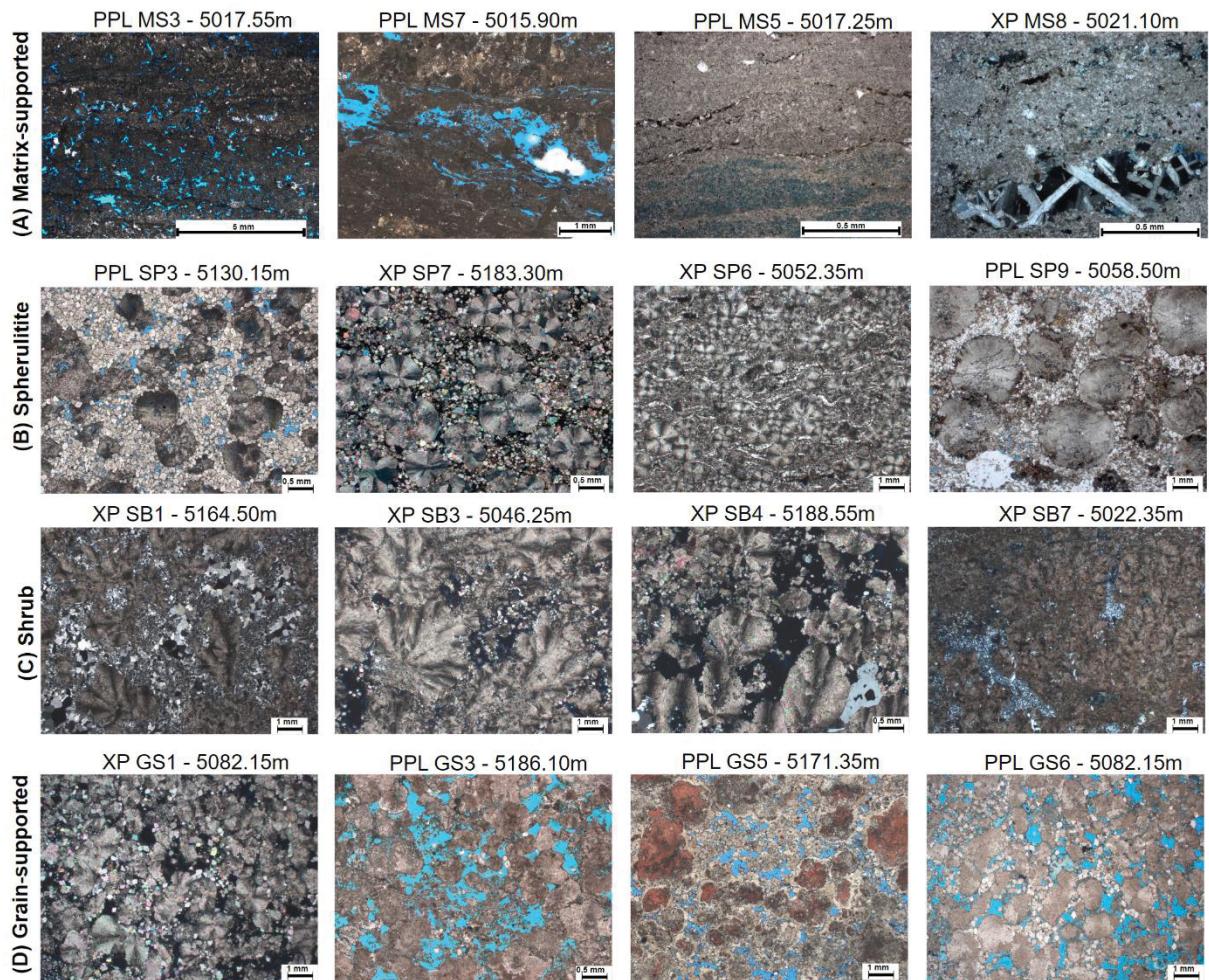
Source: The author (2022).

Caption: Photomicrographs of the main carbonate facies. Images are displayed in plane-polarized light with uncrossed polarizers (PPL) or crossed polarizers (XP). (A) matrix–supported facies presenting fine grain minerals as calcite-dolomite-silica (PPL MS3–5–7), as well as traces minerals as barite (XP MS8). In general, these images show pores generated by clay dissolution, and poor to moderate interpore connection. (B) Spherulitite examples, showing spherulite calcites. Open pore spaces can be partially or totally filled with rhombohedral dolomite (PPL SP3) and microcrystalline silica (XP SP7, PPL SP9); low permeability is found in these examples. (C) Shrub facies, presenting fascicular calcites, closed pore space filled by macro quartz (XP SB1) and microcrystalline quartz (XP SB7) generating poor permeability. Moreover, samples with open pores partially filled with dolomite and silica (XP SB3–SB4) presenting low to high permeability. (D) Examples of grain–supported carbonates presenting reworking of spherulitite and fascicular calcites, and grain–supported features (grainstone PPL GS3), and also open pore spaces partially filled with quartz and dolomite (XP GS1), dolomite (PPL GS5 and GS6).

FIGURE 21 – EXAMPLES OF THE ADDITIONAL CARBONATE FACIES
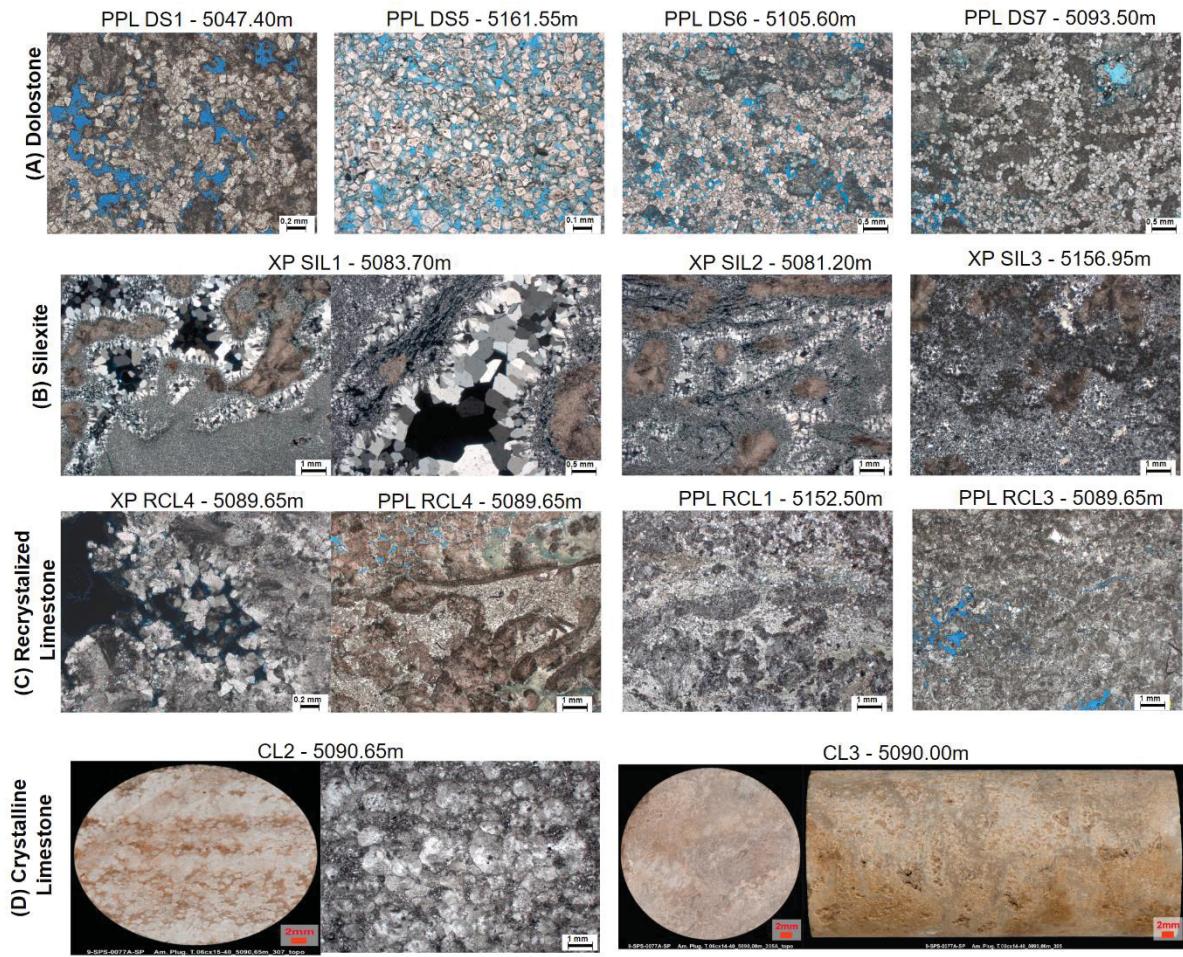
Source: The author (2022).

Caption: Examples of additional carbonates facies. Images are displayed in plane-polarized light with uncrossed polarizers (PPL) or crossed polarizers (XP). (A) Dolostones presenting dolomitized carbonates richer in rhombohedral dolomite (PPL DS5) and few spherulitite calcites (PPL DS1, DS6 and DS7); with partial porosity, and closed pores features in these carbonates, as well as poor connection between open pores. (B) Silexite showing high composition of pervasive quartz of variated size (XP SIL1–2–3); note closed pores presenting poor porosity and permeability features, with few spherulite calcites are observed. (C) Recrystallized limestones examples presenting, dolomites (XP, PPL RCL4), calcites and microcrystalline quartz minerals (PPL RCL1 and RCL3). (H) Crystalline limestones core-plug samples (CL2–CL3), in which depositional elements are not clearly differentiated.

FIGURE 22 – FACIES IN MULTISCALE VARYING FROM METERS TO MILLIMETER SCALE.
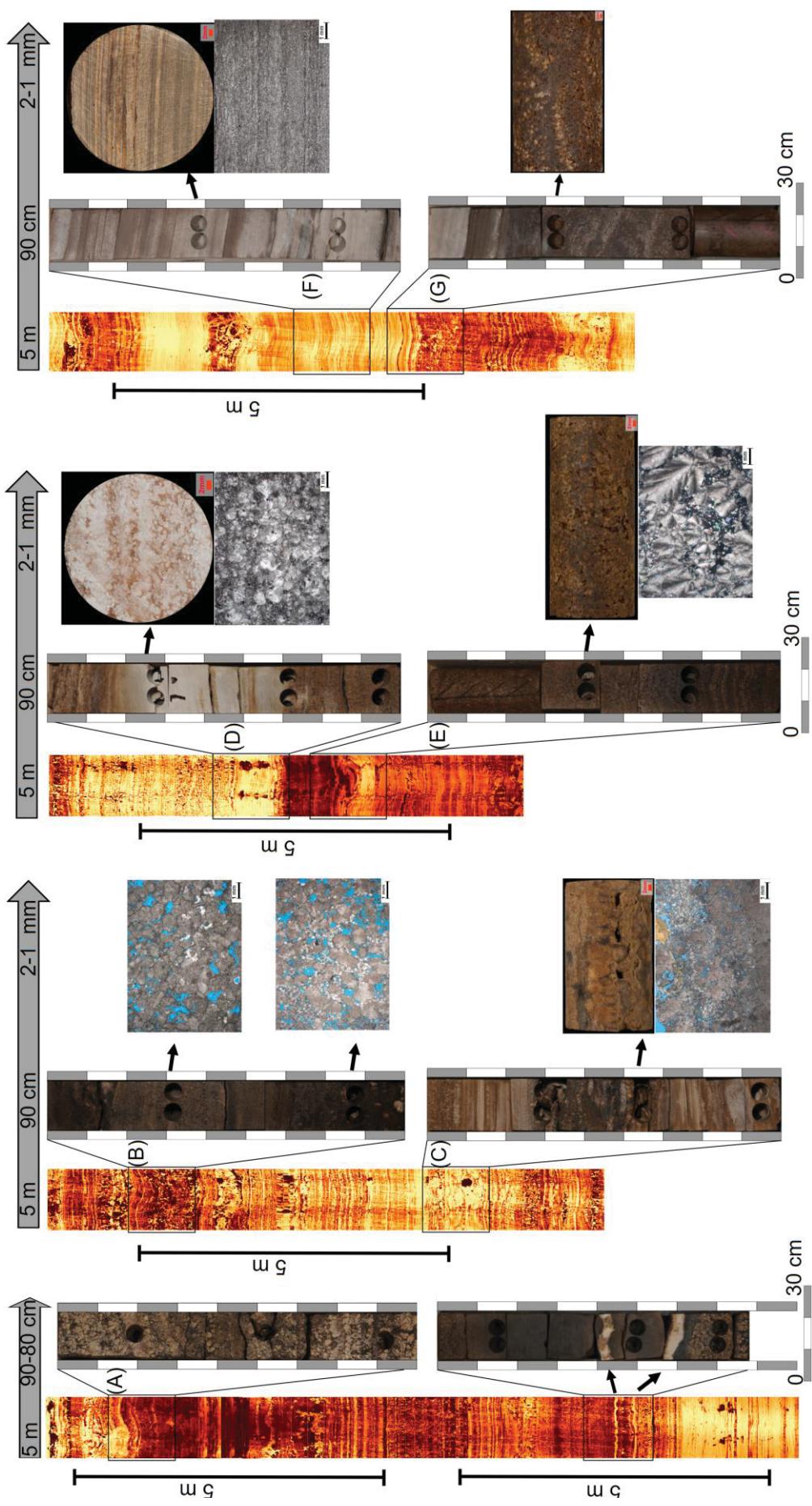
Source: The author (2022).

Caption: The Pre–Salt facies multiscale correlation. (A) Shrub log–core facies. (B) Porous grain–supported log–facies associated to shrub and spherulitites, thin section photomicrography: porous grainstone with reworked spherulitites, dolomite inter–particle. (C) Facies cyclicity in core facies scale. Bottom to top: laminites, spherulitites, shrub–spherulitites and laminites; thin section photomicrograph: inter–particle porosity partially filled with calcite and dolomite. (D) Crystalized limestone log–facies showing high amplitude pattern and in the core is observed lighter color carbonate; thin section photomicrograph shows obliterated porosity. (E) Alternation of shrub and spherulitites beddings. Dissolution process is seen in the core–plug, and in thin section the fascicular shrub calcite is partially filled with fine quartz crystals. (F) Dolomitized matrix–supported log–core facies. In thin section is observed finer laminations. (G) Several facies from top to bottom: laminites, spherulitites, and shrub–like, this association is also seen in the log–facies.

The finer–grained lithofacies reported as mudstones, wackestones, and laminites were grouped into the matrix–supported log–facies to allow the upscaling of lithological information. This merge was performed due to the limited number of samples found for these facies. In addition, for the grain–supported log–facies we merged packstones, grainstones and rudstones samples (cf. Farias et al., 2019; Lima & De Ros, 2019; Gomes et al., 2020).

3.5.2.1 Matrix–supported facies

The matrix–supported facies found within the reservoir dominate in the UBVF–5 zone, beneath the base of the salt (Ariri Formation). These are mainly composed of clay minerals, calcite, dolomite, and silica, as well as traces minerals, such as barite (FIGURE 20A).

Clay dissolution generates secondary porosity presenting open pores, and it is possible to observe microcrystalline dolomite and quartz replacing the microcalcite, which can close the pore space. In several locations of the core sections and core plugs samples, we noticed parallel and wavy laminated structures. At log scale, matrix–supported facies presented small laminations varying between 30–50 centimeters, with no apparent porosity in the BHI log resolution. In addition, at log scale the dip laminations typically found are below 10 degrees (FIGURE 22C and FIGURE 22G).

3.5.2.2 Spherulitite facies

The spherulitite facies comprehends spherical calcite elements reaching 1–5 millimeters in diameter. Spherulites present fibro–radial texture and are preserved in clay matrix, with microcrystalline quartz and dolomite material filling the inter–particle pore space between the spherical calcites (FIGURE 20B). We also identified these spherulitites in both cores and SWC samples, distributed BVF zones. Finally, we observed spherulites associated with the shrub–rich and grain–supported facies (FIGURE 22B), as reported as well in previous studies of the Santos Basin (Wright and Barnett, 2015; Gomes et al., 2020).

However, the clear observation of spherulites is limited in the image logs scale. Its presence can be inferred by the observation of minor rounded features displaced against the homogeneous BHI log amplitude. Similar features were observed by Bize–Forest et al (2018) on ultrasonic borehole images. In addition, the spherulitite log–facies are found interspersed between shrub–rich or grain–supported facies, when adding enhancement filters to contrast matrix and these round elements. Lastly, our observations showed that spherulitite log–facies occur in 0.5 meters thick layers on average.

3.5.2.3 Shrub–rich facies

The shrub–rich facies present fascicular–optic calcite crystals, mostly elongated with inter-particle open porosity. The pores may appear partially or entirely filled by microcrystalline dolomite and quartz (FIGURE 20C). The well–formed shrub shapes are similar to the arborescent and/or plum structures described in previous studies of the Pre–Salt (e.g., Farias et al., 2019; Wright, 2020). These features are also observed in cores and plugs.

The shrub log–facies observed present elongate layers and beds with upward growth from a bed substrate, mostly forming convex structures (FIGURE 22A) seen in the borehole image. The imaged shrubs in core and BHI log may reach a maximum of 5 meters in length, with lamination dipping more than 30 degrees. Additionally, minor shrub layers (30–40 centimeters thick) presenting similar arbustiform shape on cores as seen in Farias et al. (2019); and these feaatures are found in the BHI log and core section.

We observed the shrub log–facies in all the BVF zones, where it usually presents significant free fluid porosity, reaching 10–15% in the NMR log. The vug porosity varies from centimeter to decimeter scale and are usually identified in the BHI logs (FIGURE 19), which appears mostly connected in stratabound laminations and beddings. In addition, isolated vugs may appear, but are uncommon in this log–facies. Lastly, dissolution porosity is observed in BHI logs, which is limited to the vertical resolution of the ultrasonic image tool reaching 5 millimeters (Bize–Forest et al., 2014). Such situation prevents the correct evaluation of dissolution porosity below this resolution.

3.5.2.4 Grain–supported facies

The grain–supported facies (grainstones, packstones and rudstones), encompass fragments of shrubs, spherulites, which in general present broad grain size variation in photomicrographs (FIGURE 20D).

The grain–supported carbonates commonly present pore connection, and the inter–particle porosity may be partially or entirely filled with rhombohedral dolomites and microcrystalline quartz. Furthermore, the presence of calcite cements is uncommon in the available petrographic images (FIGURE 20D).

In general, grainstones and rudstones may present clear massive appearance or stratification on core sections. Moreover, the beds of these facies occur in intervals ranging between millimeters to a few meters, appearing intercalated with shrub-rich and/or spherulite-rich facies (FIGURE 22B).

Overall, the grain–supported log–facies signature in the BHI log analysis either lacks internal stratification (i.e., structureless) or it shows cross–stratification. The stratification presented dip orientation ranging between 20–30 degrees. In addition, the frequency of vugs is smaller than the shrub log facies. Furthermore, the NMR porosity measurements, on average, showed the free fluid porosity between 10–15%, and a low range of capillary and clay–bound water porosities, which in average is around 1–3%.

3.5.2.5 Dolostones, silexite, recrystallized limestone, and crystalline limestones

Other carbonate facies were found in the samples analyzed such as dolostones, silexite, recrystallized limestone, and crystalline limestones. These comprise subordinate facies on the wells exanimated.

Dolostones and silexite samples were usually found in the cores, core–plugs and SWC. These samples are usually found associated with the presence of pervasive dolomitization and silicification (e.g., FIGURE 21A dolostone–DS6, and FIGURE 21B silexite samples). Moreover, the silicified and dolomitized zones reached intervals up to 5 meters in thickness (e.g., FIGURE 22D and F). The SWC samples present the same pervasive textures in both structural high and basinward wells (Table 1).

The analysis of these pervasive features along the borehole wall at well–logging scale indicated locations with high amplitude travel time (acoustic BHI) and resistivity (resistivity BHI and resistivity well–logs) patterns (FIGURE 19), as well as the increase of density–log and PE well–logs readings for such intervals (FIGURE 19). In addition, the NMR porosities measurements are irregular where these features are found, with intervals alternating between high and low porosity values. This porosity distribution is also supported by the laboratory measurements of core–plug and SWC petrophysical data.

The recrystallized limestones usually presented recrystallization of calcites, dolomites, and microcrystalline quartz minerals (FIGURE 21C), and in few thin–sections we found crystalline carbonates with high degree of recrystallization which did not present distinguished depositional elements or resemble the depositional rock fabric (FIGURE 21D).

3.5.3 XRD analysis

Results of XRD for core–plugs and SWC samples show that the main mineral composition of the facies are calcite (median CAL 35.5 wt.%), dolomite (median DOL 23 wt.%) and quartz (median QTZ 12.72 wt.%) along all the UBVF zones. In addition, fractions of magnesium–rich calcite (median CMG 18 wt.%), and undifferentiated minerals reported as Ca–dolomite/ankerite (median CDA 24 wt.%) and dolomite/Ca–

Dolomite (median DCD 33 wt.%) occur as subordinate minerals. All of these minerals are found along the UBVF1–5 and found in all of the facies (TABLE 1). The boxplot and violin plot of the mineral composition of the XRD samples are displayed in the FIGURE 23.

TABLE 1 – SPS77 WELL SUMMARIZED RESULTS OF THE X–RAY DIFFRACTION FOR THE MAIN MINERAL PARAGENESIS

Weight Total wt. (%)	Quartz	Calcite	Dolomite	Ca-Dolomite /Ankerite	Mg-Calcite
	QTZ	CAL	DOL	CDA	CMG
Samples	1797.00	1782.00	1758.00	725.00	702.00
Min	1.00	1.00	1.00	1.00	1.00
Max	98.90	90.28	90.00	86.00	74.00
Sum	29861.06	68814.49	46139.73	19306.00	14311.00
Mean	16.62	38.62	26.25	26.63	20.39
Std. error	0.37	0.47	0.44	0.55	0.48
Variance	241.11	401.88	343.70	219.95	162.58
Stand. dev	15.53	20.05	18.54	14.83	12.75
Median	12.72	35.55	23.00	24.00	18.00
25th percentile	7.89	24.00	10.00	16.00	12.00
75th percentile	19.00	52.83	39.65	33.50	27.00

Source: The author (2022).

FIGURE 23 – X–RAY DIFFRACTION FOR SPS77, BOXPLOT AND VIOLIN PLOTS

Legend
CAL - Calcite
CDA - Ca-dolomite/Ankerite
CMG - Magnesium calcite
DOL - Dolomite
HAL - Halite
QTZ - Quartz
BAR - Barite
PIR - Pyrite
DAW - Dawsonite
MAG - Magnesite
KFD - KFeldspar
PLG - Plagioclase
DCD - Dolomite/Ca-dolomite
APT - Apatite
FLU - Fluorite
ClayMin - Clay Minerals
CRT - Cristobalite
COR - Corundum
TUN - Tunisite
SGO - Svanbergite/Goyazite
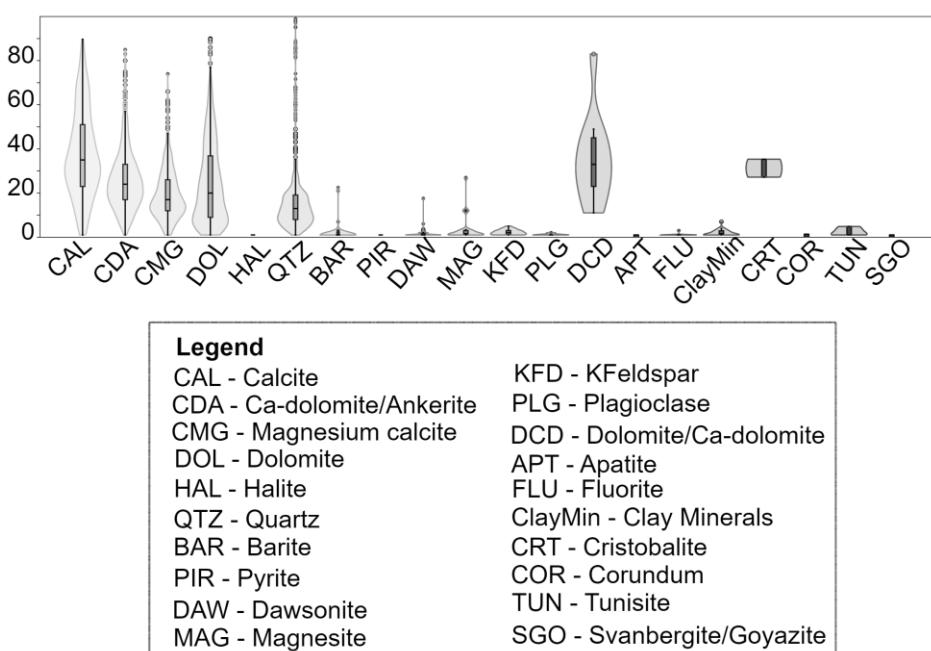
Source: The author (2022).

Caption: The Boxplot and violin plot of mineralogic composition of X–Ray diffraction, in weight total percent for Calcite (CAL), Ca–dolomite/Ankerite (CDA), Magnesium calcite (CMG), Dolomite (DOL), Halite (HAL), Barite (BAR), Pyrite (PIR), Dawsonite (DAW), Magnesite (MAG), K–feldspar (KFD), Plagioclase (PLG), Dolomite/Ca–dolomite (DCD), Apatite (APT), Fluorite (FLU), Clay minerals (ClayMin), Cristobalite (CRT), Corundum (COR), Tunisite (TUN) and Svanbergite/Goyazite (SGO) minerals, applied to core–plugs samples of the SPS–77 well.

In addition, we observed that the dolostones and silexites samples along the borehole wall correlate with the increase of the values in density and PE well–logs, which is displayed as cross–over area shading as red color in FIGURE 24. In general, a percentage above 20 wt.% for dolomite and 10 wt.% for quartz are observed in these locations.

The accessory minerals paragenesis are found usually below 5 wt.%. They comprise minerals as Dawsonite (DAW), Fluorite (FLU), Magnesite (MAG), Pyrite (PIR), Barite (BAR), Corundum (COR), Tunisite (TUN), Cristobalite (CRT), which are found sparse along the UBVF zones (TABLE 2 and FIGURE 23). The undifferentiated groups of Clays (ClayMin), Svanbergite/Goyazite (SGO) minerals also appear scattered along the upper BVF zones, as well as K–Feldspar (KFD) and Plagioclase (PLG). Finally, Dawsonite and K–Feldspar have been found concentrated below the UBVF–5 (FIGURE 24).

FIGURE 24 – COMPOSITE WELL–LOGGING AND X–RAY DIFFRACTION MINERALS (XRD), FOR SPS–77 WELL
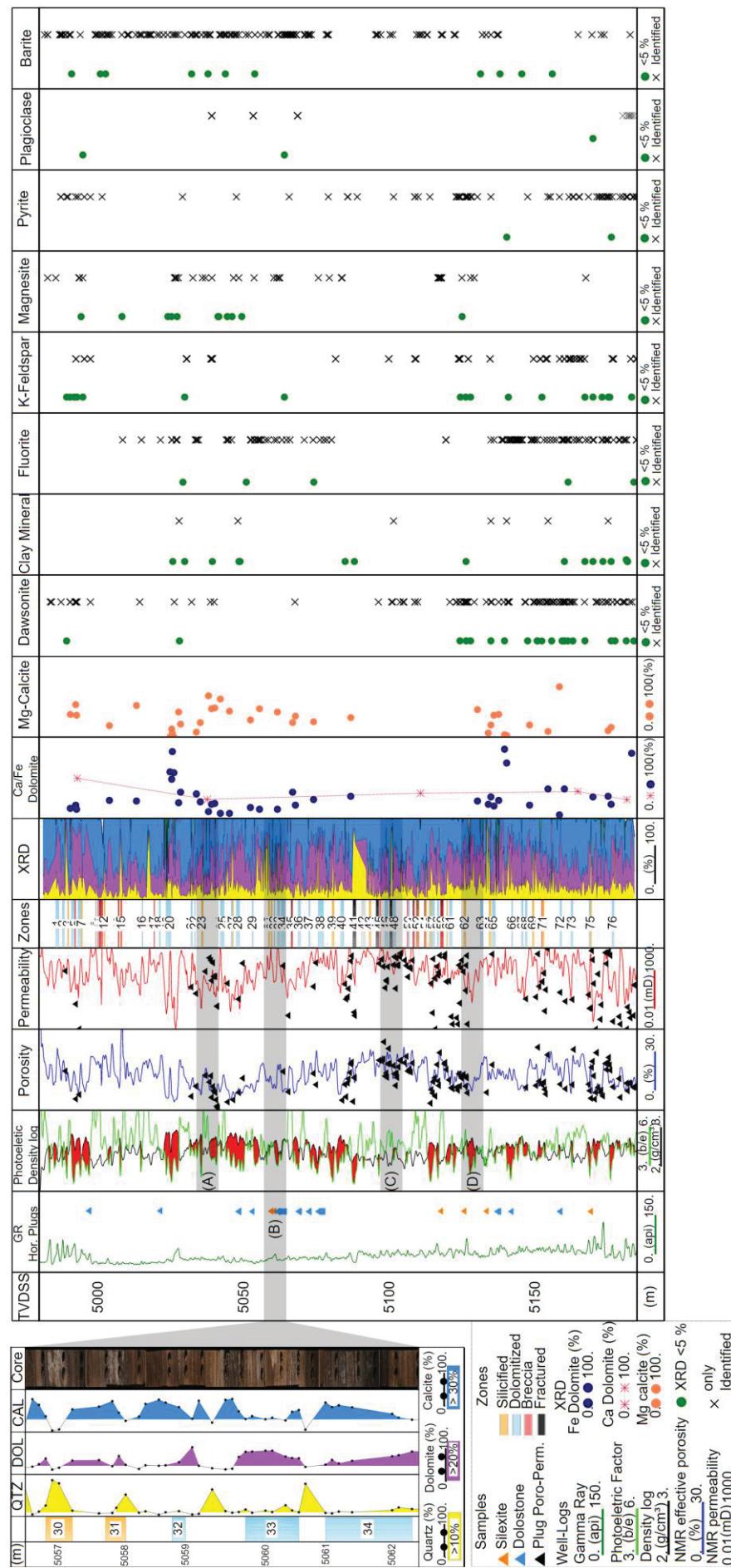
Source: The author (2022).

Caption: SPS77 well. Composite well–logs: gamma ray, photoelectric factor, density, effective porosity, and permeability. X-ray diffraction (wt.%) of calcite–quartz–dolomite composition is showed cumulatively, followed by the mineral fraction of Ca/Fe Dolomite, Mg–Calcite. Dawsonite, Clay minerals, Fluorite, Magnesite, Pyrite, Plagioclase, and Barite, respectively. (A) Example of silicified zone showing reduction of porosity and permeability logs, and core–plugs measurements. (B) A zoom–in section showing the identification of the number of pervasive zones, and the XRD (w.t%) fraction of quartz, dolomite, and

calcite, and core photography example, respectively. (C) Dolomite–rich interval showing the increase on effective porosity and permeability measurements. (D) Alternation between pervasive zones, creating intervals with high and low reservoir quality.

TABLE 2 – SPS77 WELL SUMMARIZED RESULTS OF THE X–RAY DIFFRACTION FOR THE SECONDARY MINERAL PARAGENESIS

Weight Total wt (%)	BAR	DAW	KFD	MAG	ClayMin	FLU	PIR	DCD	HAL	PLG	TUN	CRT	COR	SGO	APT
Samples	120.00	99.00	63.00	57.00	48.00	45.00	15.00	11.00	11.00	5.00	4.00	2.00	2.00	1.00	1.00
Min	1.00	1.00	1.00	1.00	1.00	1.00	1.00	11.00	1.00	1.00	1.00	27.20	1.06	1.00	1.00
Max	22.44	17.56	7.00	31.21	7.00	3.00	1.00	83.00	1.00	2.00	4.84	35.33	1.34	1.00	1.00
Sum	190.64	151.66	147.83	240.77	88.58	52.42	15.00	387.00	11.00	6.00	9.89	62.53	2.40	1.00	1.00
Mean	1.59	1.53	2.35	4.22	1.85	1.16	1.00	35.18	1.00	1.20	2.47	31.27	1.20	1.00	1.00
Std. Error	0.27	0.18	0.18	0.88	0.18	0.07	0.00	6.06	0.00	0.20	0.93	4.07	0.14	0.00	0.00
Variance	8.72	3.21	2.13	43.84	1.48	0.21	0.00	403.56	0.00	0.20	3.43	33.05	0.04	0.00	0.00
Std. Dev	2.95	1.79	1.46	6.62	1.21	0.46	0.00	20.09	0.00	0.45	1.85	5.75	0.20	0.00	0.00
Median	1.00	1.00	2.00	1.72	1.15	1.00	1.00	33.00	1.00	1.00	2.03	31.27	1.20	1.00	1.00
25th percentile	1.00	1.00	1.00	1.00	1.00	1.00	1.00	23.00	1.00	1.00	1.00	27.20	1.06	1.00	1.00
75th percentile	1.00	1.55	3.00	3.31	2.32	1.00	1.00	45.00	1.00	1.50	4.39	35.33	1.34	1.00	1.00

Source: The author (2022).

The FIGURE 25A shows the XRD ternary calcite–dolomite–quartz mineral chart for shrubs-rich, spherulite-rich, grainstone samples. It is possible to observe a broad distribution of the dataset, with unclear observation of clusters or tendencies. This is mostly because all these facies have dolomite and quartz in their composition. In general, the mineral association may suggest an incipient to very intense contribution of dolomite and quartz in these facies, that we observed partially dolomitized or silicified.

FIGURE 25 – SPS–77 WELL X–RAY DIFFRACTION TERNARY PLOT FOR CARBONATES
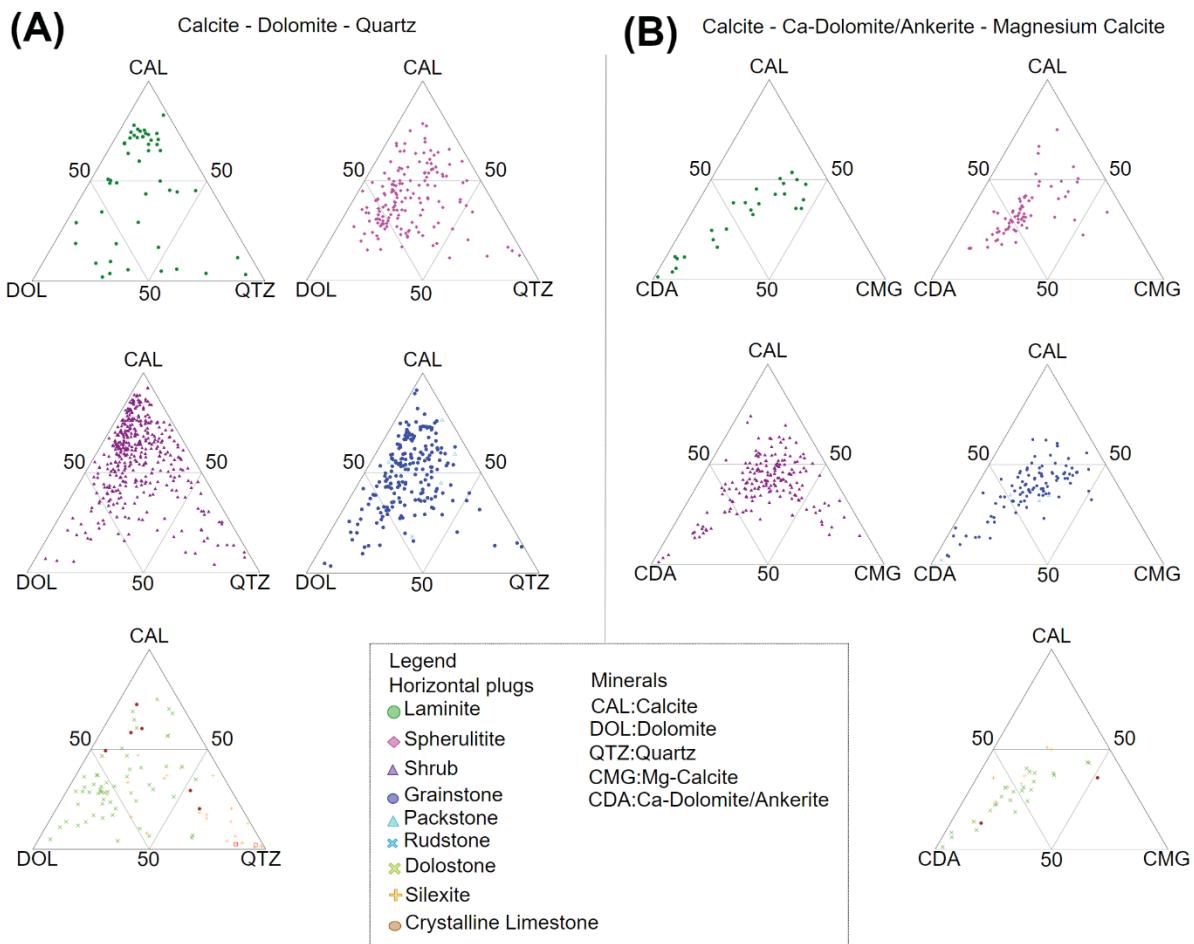
Source: The author (2022).

Caption: The X–Ray diffraction ternary plot for carbonates facies, for SPS–77 well. (A) Calcite–Dolomite–Quartz; (B) Calcite–Ca–Dolomite/Ankerite–Mg–Calcite.

On the other hand, laminite samples are seen divided in three groups, each one above 50 wt.% for each mineral corner (FIGURE 25A). In addition, we noticed

that samples described as dolostone and silexites, indeed follow dolomite and quartz corners.

Finally, on the ternary plot which comprises calcite and ferric–magnesium–rich calcites (FIGURE 25B), all the facies present richer composition of CAL and CDA. The presence of the CMG higher than 50 wt.% is clearly seen only for the shrub-rich carbonate, and for the remaining facies this mineral concentration less than 50 wt.%.

3.5.4   RCAL and FZI analysis

The computed routine core analysis (RCAL) results are grain density, porosity, and permeability measurements from core–plugs and SWC samples. TABLE 3 shows the summarized results of RCAL separated by facies, considering the structural high, and TABLE 4 for the basinward wells. Most of the petrophysical dataset is concentrated in the structural high wells (624 samples), in comparison with those wells located at the basinward area of the field (134 samples).

TABLE 3 – PETROPHYSICAL RESULTS OF ROUTINE CORE ANALYSIS PRESENTED FOR EACH FACIES FOR ALL OF THE WELLS LOCATED AT THE STRUCTURAL HIGH

| Facies | Wells located at the structural high | | | | | | | | |
| | Density (g/cm³) | | | Porosity (%) | | | Permeability (mD) | | |
	Samples	Mean	Min	Max	Mean	Min	Max	Mean	Min	Max
Dolostone	27.00	2.74	2.62	2.82	10.23	2.20	19.20	4.42	0.02	660.00
Rec. Limestone	4.00	2.74	2.69	2.77	9.25	6.50	14.30	4.74	0.71	81.40
Silexite	10.00	2.66	2.59	2.78	9.46	3.23	18.00	1.00	0.00	455.00
Breccia	1.00	2.65	2.65	2.65	4.20	4.20	4.20	0.35	0.35	0.35
Mudstone	4.00	2.74	2.71	2.77	12.85	2.10	25.50	6.34	0.01	2100.00
Spherulitite	127.00	2.73	2.58	2.82	9.87	0.20	22.90	5.24	0.00	645.00
Laminite	13.00	2.72	2.55	2.80	7.07	0.30	26.40	0.16	0.00	473.00
Shrub-rich	215.00	2.71	2.57	2.81	13.60	1.90	25.63	36.44	0.00	4360.00
Grainstone	180.00	2.72	2.63	2.81	14.55	0.80	25.80	19.62	0.00	4018.00
Rudstone	9.00	2.71	2.69	2.73	12.40	5.50	18.00	11.96	0.11	349.00
Packstone	29.00	2.72	2.69	2.77	11.94	3.70	23.30	17.88	0.11	2920.00
Wackestone	5.00	2.74	2.70	2.76	12.70	0.40	23.20	24.17	1.98	104.00
All Facies	624.00	-	-	-	-	-	-	-	-	-

Source: The author (2022).

TABLE 4 – PETROPHYSICAL RESULTS OF ROUTINE CORE ANALYSIS SEPARATED FOR EACH FACIES FOR ALL OF THE WELLS LOCATED AT THE BASINWARD AREA

Facies	Wells located at basinward area								
	Density (g/cm³)			Porosity (%)			Permeability (mD)		
	Samples	Mean	Min	Max	Mean	Min	Max	Mean	Min	Max
Dolostone	3.00	2.75	2.71	2.79	14.22	4.99	26.12	0.9495	0.0567	222.00
Rec. Limestone	1.00	2.65	2.65	2.65	4.80	4.80	4.80	0.0001	0.0001	0.00
Silexite	4.00	2.64	2.61	2.68	6.23	1.97	12.59	0.075	0.0001	11.76
Breccia	-	-	-	-	-	-	-	-	-	-
Mudstone	1.00	2.68	2.68	2.68	1.93	1.93	1.93	0.0001	0.0001	0.00
Spherulitite	25.00	2.70	2.59	2.81	7.43	0.01	17.75	0.0383	0.0001	34.28
Laminite	20.00	2.69	2.50	2.77	5.45	0.53	13.70	0.0032	0.0001	32.38
Shrub-rich	47.00	2.72	2.66	2.78	8.39	0.12	21.75	0.0622	0.0001	2936.00
Grainstone	27.00	2.73	2.67	2.78	10.26	0.01	19.02	0.2019	0.0001	157.90
Rudstone	6.00	2.73	2.71	2.75	13.47	2.79	18.59	1.843	0.0001	133.20
Packstone	-	-	-	-	-	-	-	-	-	-
Wackestone	-	-	-	-	-	-	-	-	-	-
All Facies	134.00	-	-	-	-	-	-	-	-	-

Source: The author (2022).

In general, the facies types found in the structural high and in basinward areas mainly encompass shrub-rich, spherulite-rich, and grain–supported facies (FIGURE 19 and FIGURE 22). Subordinately, we found matrix–supported, recrystallized limestone, dolostones, and silexite samples that appeared in smaller proportion. The grain density values varied between 2.61 to 2.82 g/cm³, with a mean value of 2.72 g/cm³. Additionally, a variable range of gas porosity ($\varnothing_{gas}$) and absolute permeability (K_{abs}) are observed for different facies (TABLE 3 and TABLE 4), which can be also observed in stratigraphic logs in the BVF (FIGURE 19, FIGURE 22, and FIGURE 24). Moreover, to analyze the contribution of the different facies found in the BVF reservoir quality we calculate Hydraulic Flow Units (HFU) to evaluate the porosity and permeability properties in these carbonates (FIGURE 26).

FIGURE 26 – HYDRAULIC FLOW UNITS
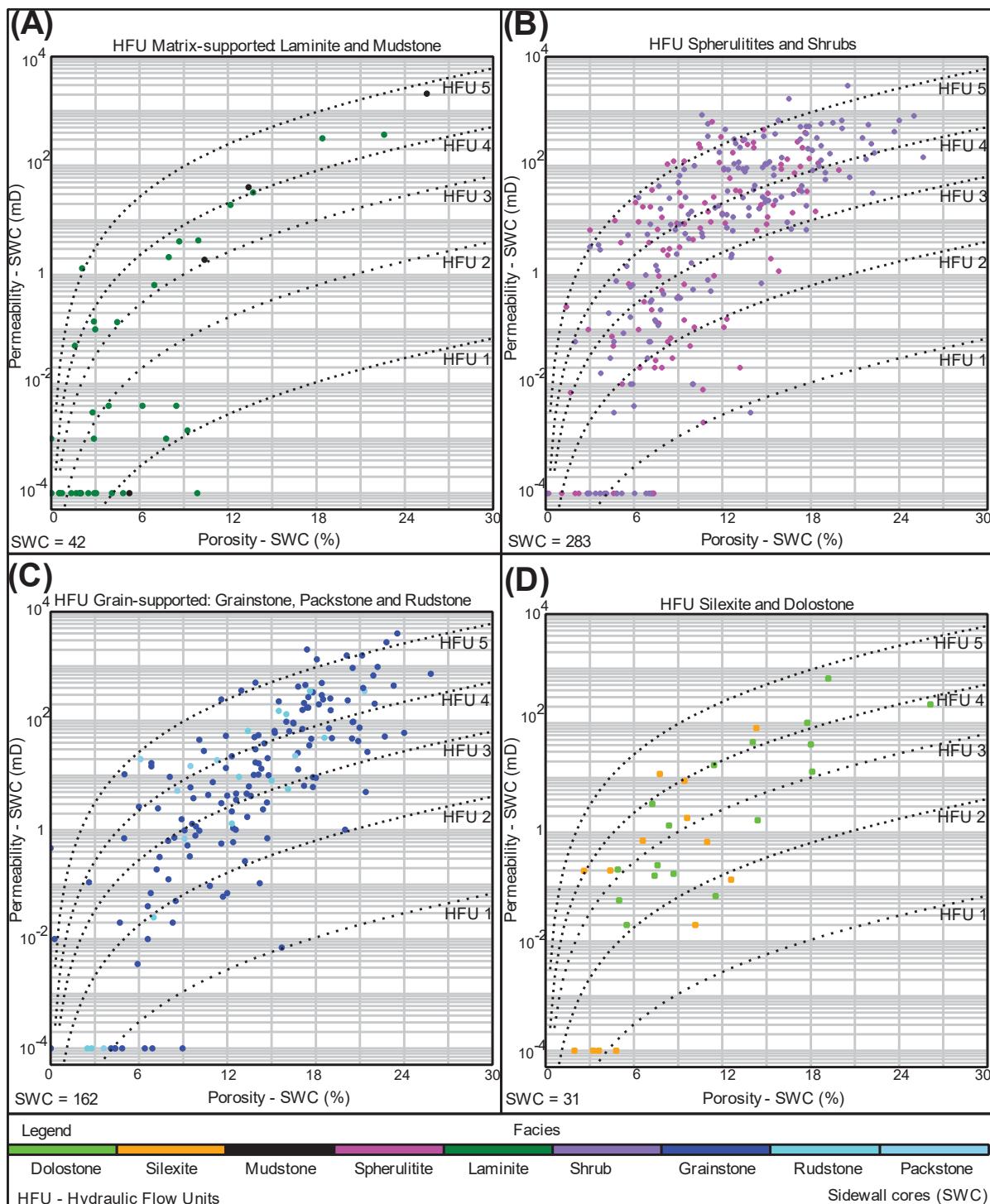
Source: The author (2022).

Caption: gas porosity (Ø$_{gas}$) x absolute permeability (K$_{abs}$) scatter plots with the 5 hydraulic flow units (HFU 1–5) using data from structural high and basinward area wells. Each one of the graphs display the results of sidewall core (SWC) samples separated by facies with a wide variable range of results among all facies. (A) HFU matrix–supported, comprising 42 samples of Laminites and Mudstones. (B) HFU Spherulites-rich and Shrubs-rich facies totalizing 283 samples. (C) HFU grain–supported facies with 162 samples, including Grainstones, Rudstones, and Packstones carbonates. (D) HFU Dolostone and Silexites, composed of 31 samples.

The HFU calculation was performed using only SWC samples available, considering all the well's extension in the structural high and basinward zones. We assured a random selection of samples retrieved from the borehole wall for all wells, not limiting any of the core intervals. Therefore, the HFU evaluates all of the sections of BVF trying to decrease a sample selection bias from core–samples, mostly taken from the UBVF in the Pre–salt wells. Lastly, the crystalline limestone samples were not included in this analysis, because these samples were only found in core–plugs.

We identified five HFU within the BVF, in which a diverse distribution of $\emptyset_{gas}$ and K_{abs} is noticed (FIGURE 26). In general, the samples within the HFU 3 and 5 indicate that $\emptyset_{gas}$ starts to increase above 6 %, and K_{abs} above 1mD. A less representative group of samples show low permeability values and are found between HFU 1 and 2, composed of $\emptyset_{gas}$ < 6 % and K_{abs} < 0.01 mD, observed in all carbonate facies.

Moreover, samples from the matrix–supported facies are mainly composed of laminites. These are found in a smaller proportion (42 samples) within the BVF reservoir when compared to the other lithofacies (FIGURE 26A). Additionally, we observed two isolated groups in the matrix–supported HFU, the first one presents lower values of $\emptyset_{gas}$ (3–10 %) and K_{abs} (0.0001–0.005 mD), and a second follows the HFU 3 and 5, with K_{abs} higher than 0.05 mD.

Shrubs–rich and grain–supported lithofacies are found in all of the five HFU, but mostly within the HFU 3 to 5, usually presenting $\emptyset_{gas}$ > 6 % and K_{abs} > 0.1 mD. Furthermore, for these facies we also observed samples with higher values of porosity varying between 18 to 24%, and permeability measurements higher than 100 mD (FIGURE 26B and C). In addition, SWC comprises the HFU 1 to 2 were observed for these facies, with lower values of porosity and permeability, in general presenting $\emptyset_{gas}$ < 6 % and K_{abs} < 0.01 mD. Lastly, the spherulitite facies appeared in all of the five HFU with a broad distribution of porosity and permeability, likewise shrubs–rich and grain–supported samples (FIGURE 26B).

Furthermore, the pervasive dolostones and silexite samples also appeared distributed in a variable range within the five HFU (FIGURE 26D). The dolostone samples in HFU 2 and 3 present ranges between 3–10% in porosity and 0.01–2 mD of absolute permeability. Additionally, the HFU 3 and 4 usually present higher reservoir quality ranges, with $\emptyset_{gas}$ above 12 % and K_{abs} above 10mD, with similar distribution as found for shrubs–rich and grain–supported facies. Lastly, the silexite

are mainly concentrated in HFU 2 to 4; however, these samples generally not reached $\emptyset_{gas}$ higher than 15 %, and K_{abs} higher than 100 mD.

The results suggest that a single hydraulic flow unit is constituted by several facies and seems to be related to the wide distribution of porosity and permeability along the BVF. Afterwards, we present the integration of the HFU analysis at well–logging scale in the petrophysical evaluation section. This analysis uses the flow limits found in the SWC samples found in this section, and are upscaled to the borehole extension, assisted by the NMR porosity and permeability values logged in the BVF.

3.5.5 PCA results

To evaluate the influence of carbonate constituents in the petrophysical framework, we reviewed the photomicrographs of thin sections, the XRD for mineral evaluation, and the information of RCAL horizontal plugs. We performed the PCA analysis to obtain a qualitative evaluation due to the substantial number of samples. This evaluation used the most significant mineral composition provided by the XRD minerals (e.g., CAL, DOL, QTZ, CMG and CDA) and the RCAL ($\emptyset_{gas}$, K_{abs} and grain density) measurements.

The PCA analysis used 445 horizontal core–plugs, in which all features contained the information needed without missing values. First, we performed the standardization transformation for each feature in the dataset, following the PCA workflow. As result, we reached seven principal components (PC), which represented 0.992 of accumulated variance, and 0.043 of component variance of the dataset (FIGURE 27A). Finally, the output data displayed in the PC1–PC2 scatter plot (FIGURE 27B) was separated by facies groups and visualized using linear projections, allowing to investigate the lithofacies samples in multivariate axes, which represented each examined feature (FIGURE 27C).

FIGURE 27 – PRINCIPAL COMPONENT ANALYSIS
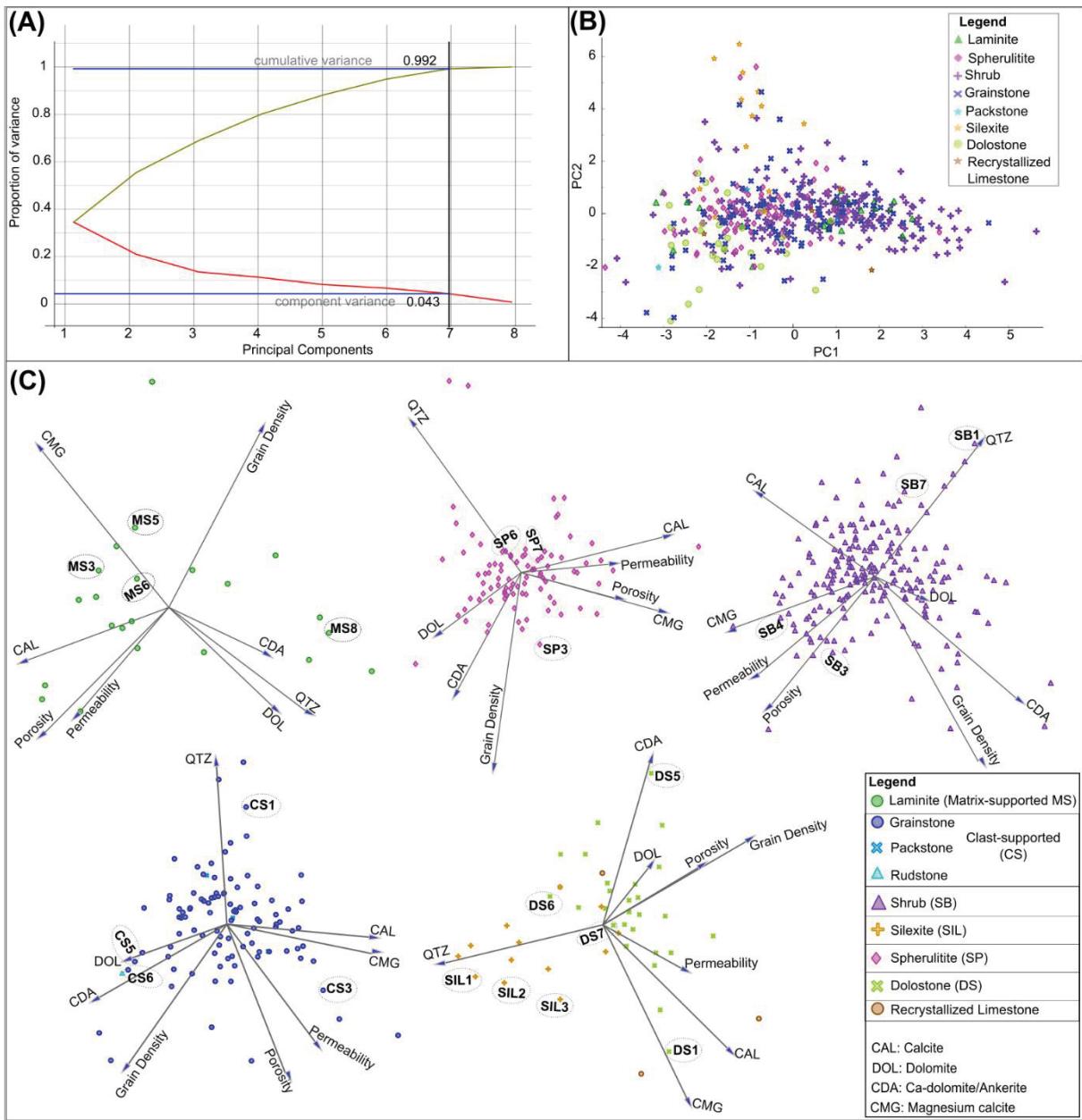
Source: The author (2022).

Caption: Principal component analysis results using main minerals (Calcite–Dolomite–Quartz–Calcite–Ca–Dolomite/Ankerite–Mg–Calcite) and laboratory petrophysical measurements (gas porosity, absolute permeability, and grain density). (A) Scree–plot, in which seven principal components reached 0.992 of cumulative variance, and 0.043 of component variance. (B) The PC1 and PC2 scatter plot. (C) Linear projection view individualizing each carbonate facies. The samples presented for each group of facies are referred to the thin section photomicrographs of FIGURE 20 and FIGURE 21.

The linear projection of PCA results showed that for carbonate facies (matrix–supported, grain–supported, spherulitites, shrubs–rich, dolostones–silexites), there is influence of the mineral composition in the petrophysical properties. This is clearly displayed by the position of the samples into the direction of each eigenvector

(FIGURE 27C). Furthermore, it is noticed that as further the samples align to the eigenvectors, more influence these elements have on that respective PC, and consequently, higher the impact of that feature on the sample petrophysical measurement.

In general, samples with a significant composition of calcite, magnesium–rich calcite, and dolomite eigenvectors, followed the direction of petrophysical eigenvectors; suggesting that they are key elements controlling the petrophysical framework, especially for the shrubs–rich, spherulitites–rich, grainstones and dolostone samples. Moreover, the grain density eigenvector is displayed in between the calcite and dolomite vectors, suggested a significant contribution of these minerals in the carbonate composition. Finally, another important observation is about the increase of quartz eigenvector, that in general presented an opposed linear projection when compared to the porosity and permeability eigenvectors in all samples, but best evidenced in silexites samples.

Additionally, the projection of the matrix–supported carbonate samples has not shown clear observations, or it followed the same patterns found in the other facies, especially because most samples are aligned in between the CMG and CAL eigenvectors. However, a partial distribution of calcite and dolomite may be inferred, because few samples are aligned to the porosity and permeability eigenvectors.

Lastly, the review of photomicrographs showed that some samples presented closed inter–particle pore spaces. In general, these samples are mainly filled by microcrystalline quartz displayed in FIGURE 20 (e.g., SB1 and SB7, SP6 and SP9, CS1, SIL1–SIL3), as well as it is noticed the presence of rhombohedral dolomite in open and connected pores (e.g, SB3, SB4, CS2, DS5).

3.5.6   Petrophysical Evaluation

The petrophysical evaluation of the BVF was performed for all wells located the structural high and at the basinward area. This analysis was assisted by the well–logs, thin–section, XRD, RCAL information presented in the previous sections.

The correlation for the wells located in the structural high is presented in FIGURE 19, FIGURE 24, and FIGURE 28A. In general, these wells are characterized by shrubs–rich, spherulitites–rich, and grain–supported log–facies. These carbonates

facies dominantly present higher porosity and permeability values, as shown by the NMR well–logs and assisted by the RCAL measurements. Furthermore, few intervals of matrix–supported log–facies occur within the BVF, are usually observed associated with grainstones in the UBFV1, and more frequently with spherulitites facies in clay-rich intervals of the wells located at the basinward area of the Sapinhoá field.

FIGURE 28 – COMPOSITE WELL–LOG CORRELATION FOLLOWING THE SW–NE DIRECTION
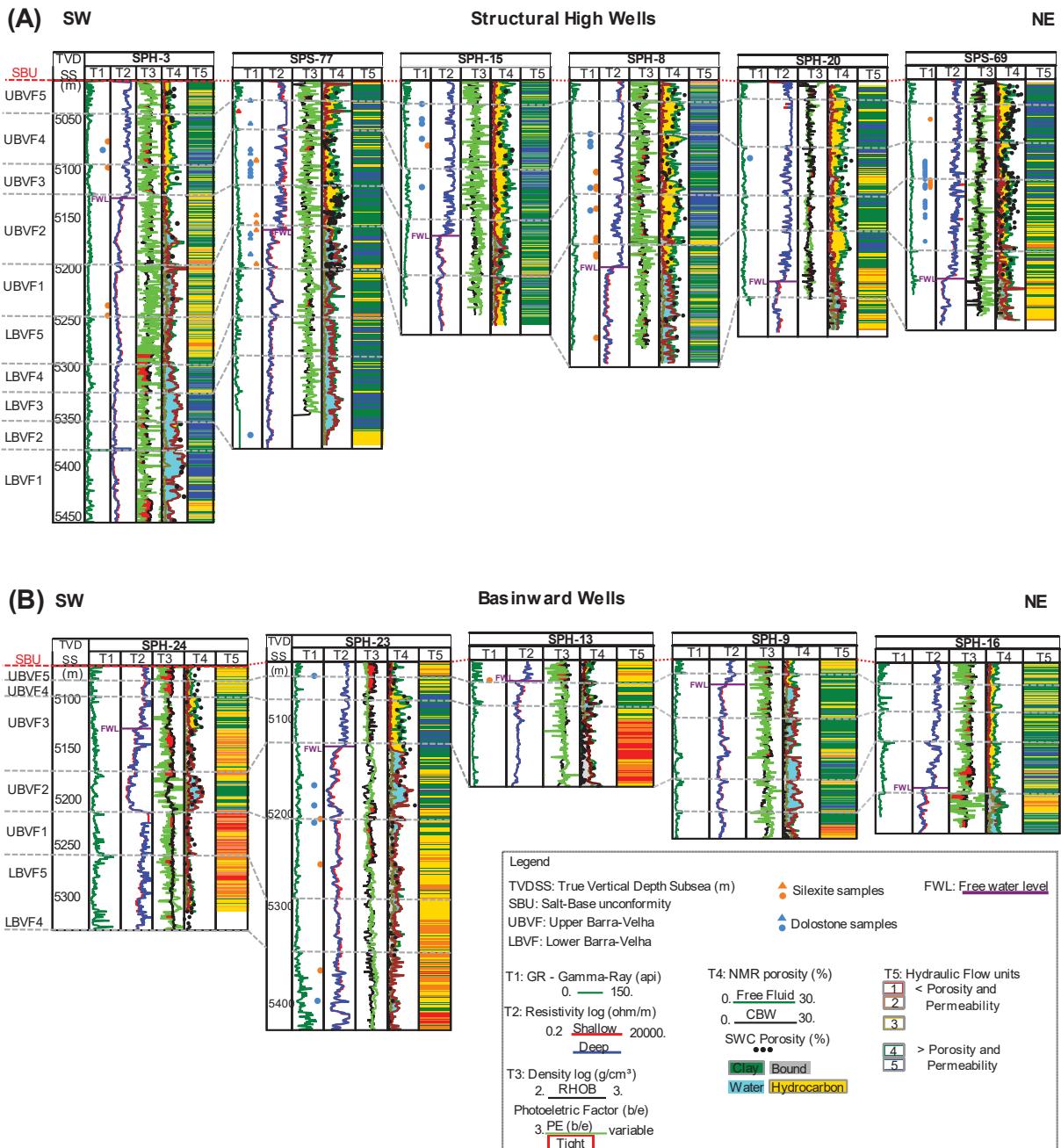
Source: The author (2022).

Caption: Well-correlation within the divisions of Barra Velha Formation (BVF). Samples of silexites, dolostones and pervasive zones are showed in several positions of BVF. Well logs displayed: gamma–ray log, resistivity logs, density-log, photoelectric factor, nuclear magnetic resonance log with gas porosity from side–wall cores. Last track shows the Hydraulic flow units (HFU) 1–5 covering all BVF. (A) Production wells located at the structural high. (B) Injection wells located at the basinward area. Additionally, tight intervals (HFU 1–2) are commonly observed in the basinward area, and production wells usually presented better flow units (HFU 3–4–5).

Another important observation about the reservoir quality found is that in the structural high wells, the NMR well–logs easily reached the highest readings in free fluid porosity along all the UBVF zones. Moreover, most of the UBVF zones are fully saturated with light hydrocarbons, as seen in production wells such as SPH–15 and SPH–8 (FIGURE 28A). Additionally, the free water level (FWL) was identified in all wells, generally through the inflection of resistivity well–logs, nearly 200 meters bellow of the sub–salt unconformity, as exemplified at SPS–69 and SPH–20 wells (FIGURE 19 and FIGURE 28).

Although most of the total porosity is characterized as free fluid porosity, distinguished capillary water and clay bound porosities distribution are observed in the wells of the structural high. In general, both of these porosities presented a varied range in the NMR readings. Moreover, a trend of increment is noticed starting from UBVF–1 zone in direction of the bottom well.

Lastly, for all wells in the structural high, we identified intervals presenting alternation between high porosity–permeability zones with tight intervals. This behavior is predominantly associated either with dolomite–rich or silica–rich intervals (FIGURE 24A and D) seen in well-logging or in RCAL measurements (FIGURE 24B).

Dolomitization process, is associated with high petrophysical conditions (FIGURE 24C and D). Rhombohedral dolomite crystals are seen opening and/or connecting pore spaces in thin–section micrography (FIGURE 21E, DS1 and DS5 samples), also distinguished patterns of pervasive textures in the cores, core–plugs and SWC samples analyzed, especially for the SPS–69 and SPS–77 wells located in the structural high. Furthermore, in some zones of dolomite–rich composition, a reduction in porosity–permeability values were noticed caused by rhombohedral dolomite closing the pore space and decreasing the pore connectivity (FIGURE 21A, DS7 sample).

Silicified zones usually presented reduction in the reservoir quality (e.g., FIGURE 21B, SIL1–2 samples), and most of the samples presented a pervasive

texture. In general, totally silicified intervals present porosity filled by microcrystalline quartz, which decreases the pore connectivity. In partially silicified zones alternations of high to low petrophysical measurements are observed, since the porosity and permeability were not entirely obliterated (FIGURE 24D).

Furthermore, wells located at basinward area of Sapinhoá field are injection wells. These wells presented similar patterns of porosity distribution in comparison with the well located on the structural high. They also presented the reduction of the free fluid porosity in direction to the bottom well, as well as the increase of capillary water and clay bound water porosities (FIGURE 28B).

Likewise, the tight zones of the basinward wells present similar patterns of well-logs found in the structural high (FIGURE 28B), with the increased of density and PE well–logs readings. In addition, the SWC samples present pervasive textures, commonly silicified or dolomitized.

The FWL in the basinward wells also presented the inflection of resistivity log measurements. However, differently from the wells found in the structural high, the oil saturation column varies within the BVF units (FIGURE 28B). For instance, the SPH–09 and SPH–13 injection wells present approximately 30 meters of hydrocarbon saturation, while in the SPH 16, 23, and 24 wells, the hydrocarbon intervals reach 100–200 meters.

The flow unit analysis applied to all wells indicates that HFU 1 and 2 are affected by the increase of clay/bound porosities and decrease in free fluid. These are commonly observed associated to the wells located in the basinward area, with zones richer in capillary bound–clay water porosity (e.g., FIGURE 28B of the SPH–13 well). In addition, the HFU–3 is found in all of the BVF units, this flow unit appears usually below the UBVF–3 in the structural high. Furthermore, in the basinward wells the HFU–3 is observed between UBVF 1 and UBVF 2 zones.

In addition, the HFU 4 and HFU 5 were observed in all wells of the structural high. Another important feature noted is that these flow units comprise most of the UBVF zones, usually saturated of hydrocarbons above the FWL. Furthermore, the petrophysical properties evaluated nearby these intervals affected by dolomitization presented higher values of porosity and permeability. The silicification presented low readings of porosity and permeability (FIGURE 28A) indicating that these processes may respectively enhance or decrease the reservoir quality in the Pre–Salt carbonates.

Moreover, another distinguished feature observed in these carbonates are stratabound dissolution features, which also presented an important role in the reservoir quality observed in all wells, because they frequently appear as vugs found in the BHI log (FIGURE 29). In general, several sparse vugs appear along the borehole wall, and with the increase of the dissolution process, these vugs appear connected; and they are found entirely distributed along all of the BVF (FIGURE 29A and B). In addition, when stratabound vugs are highly connected (FIGURE 29C) they may create channeled porosity zones reaching more than 1 meter of extension; as well as collapsed zones (i.e., caves) or breccias are observed, either in BHI logs or in cores analyzed.

Finally, the observed dissolution features may also be correlated with the NMR log porosity, in which a noticeable repetitive pattern of vugs are observed. This pattern grades from major to minor concentration of perceptible vugs in the BHI log (FIGURE 29A) in a few meters. Moreover, these repetitive patterns can be noticed along all of the BVF, including in zones located nearby dolomitized/silicified carbonates. Therefore, it indicates the effect of dissolution, silicification and dolomitization in the petrophysical framework of BVF.

FIGURE 29 – THE DISSOLUTION EFFECTS OBSERVED ACROSS THE SAPINHOÁ FIELD
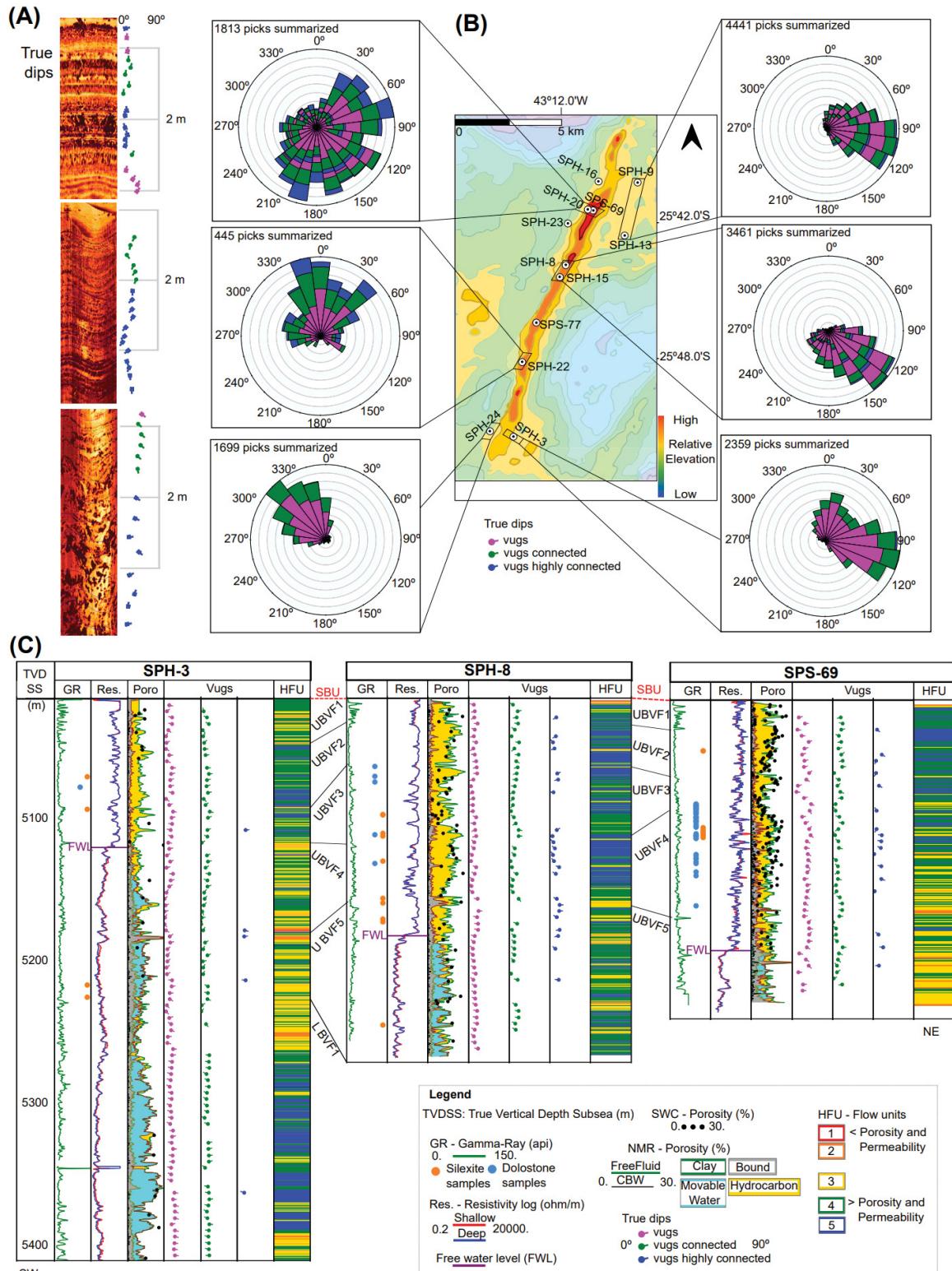
Source: The author (2022).

Caption: The dissolution effects observed in the BHI logs presented along the structural high and basinward area. Well-logs: gamma–ray, resistivity, nuclear magnetic resonance with gas porosity from side–wall cores. (A) Examples of orientation of laminations (dips) affected by dissolution processes in 2 meters interval: stratabound vug porosity (fuchsia), connected vugs (green), and highly connected vugs (blue) following the sedimentary laminations/beddings. (B) Summarized overview of the stratabound dips, individualizing the types of vug porosity. (C) Correlation wells applied for SPH3–

SPH8–SPS69 wells. The SPH–8/SPS–69 wells example shows highly connected vugs found at the same position of dolomitized or silicified zones. Last track shows the Hydraulic flow units 1–5.

3.6 DISCUSSIONS

3.6.1 Controls on the reservoir quality

The Brazilian Pre–Salt carbonates present heterogeneities and a wide variation of porosity and permeability distribution, which is associated with intense diagenetic processes, modifying vertically and laterally the petrophysical characteristics of these rocks (Herlinger et al., 2017; Lima et al., 2020). Moreover, the influence of dissolution, silicification and dolomitization processes are relevant elements that control the reservoir quality.

In general, the reduction of petrophysical measurements is caused by the presence of minerals partially or totally filling the interparticle porosity; and additionally, the blocking the connections between the pores. In all facies microcrystalline quartz and dolomite, partially or entirely replacing calcite are presented, and the dissolution of unstable clays, similarly as found in other Brazilian and African Aptian deep–water Pre–Salt carbonates are common (Wright and Barnett, 2015; Saller et al., 2016; and Lima & De Ros, 2019).

The abundant dissolution evidence presented at the same locations of pervasive dolomitized features certainly suggests that both processes may be key elements that enhance the petrophysical quality within the BVF reservoir (FIGURE 19, FIGURE 24, and FIGURE 29), particularly when integrated to BHI, NMR log and laboratory measurements.

The pervasive dissolution of carbonates may be related to dissolution of Mg–clays, as suggested by previous studies in the Pre–Salt reservoirs (Wright & Barnett 2015; Herlinger et al., 2017; Lima and De Ros, 2019). However, the characterization of Mg–clay using logging data is a complex task; mostly because wireline tools present limitations to correctly identify unstable clays in the Pre–Salt (Herlinger et al., 2020).

Moreover, the best tool available to suggest the presence of clay–rich intervals is indeed the NMR clay bound log, which provides a quantitative measure of clay bound porosity; consisting in a qualitative indicator of clay–rich zones. This

association is observed in this study, and for instance, the wells located at the structural high (i.e., the main producing zones) have inexpressive clay–bound water porosity distributed along the BVF (FIGURE 19 and FIGURE 28A), suggesting that most of the total porosity measurements found are not associated with Mg–clays, due the intense clay dissolution during the diagenesis of the Pre-Salt carbonates (Tosca & Wright, 2015). On the other hand, the wells located at the basinward area presented clay–rich zones (FIGURE 28B), where the NMR clay–bound log showed contributions on the total porosity of the injection wells.

Nevertheless, our results showed the presence of the dissolution process in several instances and locations along the borehole extension for all Sapinhoá field wells. The observations of larger vugs, regardless of the scale, indeed exemplifies that a reasonable amount of porosity and permeability found within these carbonates are not entirely depositional.

Another relevant control in the reservoir quality is the dolomitization and silicification contribution. The presence of intervals containing enrichment of silica and dolomite could be partially explained due to hydrothermal alteration in Aptian Pre–Salt carbonates, as exemplified in studies from Campos Basin (Viera de Luca et al., 2017; Lima & De Ros, 2019; Lima et al., 2020) and Kwanza Basin (Saller et al. 2016; Teboul et al. 2016). Furthermore, considering this hypothesis, the hydrothermal fluids reacted with the rock fabric, replacing the original mineral components and either obliterate or create pores as response of the fluid composition, pressure, and temperature (e.g., hydrothermal silicification in carbonate – Menezes et al., 2019; hydrothermal dolomitization in carbonates – Li et al., 2016). As observed in this study, the petrophysical evaluation of dolostones and silexites presented either extremely porous and permeable or tight porous carbonates, respectively (e.g., FIGURE 24 and FIGURE 28); and we aim to investigate a possible hydrothermal contribution in a next publication.

Moreover, since dolomite–rich and silica–rich intervals are also find nearby fractures and breccia zones (FIGURE 24), a possible contribution of hydrothermal fluids driven through fault systems in carbonate reservoirs (Davies & Smith., 2006; Li et al., 2016; Lima et al. 2020) needs to be further investigated; especially due to the association of deep faults observed in seismic scale (Faria et al., 2017; Lima et al., 2020) that surround the carbonate build–up structures and the structural high of the Pre–Salt play.

However, the dolostone and silexites SWC samples found along uncored wells may be inferred as dolomitization/silicification intervals and not implied exclusively as hydrothermal, particularly due the similarities of the pervasive characteristic and logging response. As Lima and De Ros (2019) observed, the Pre–Salt reservoir, carbonates may present silicification as result of syndepositional, early and/or late burial diagenesis, hydrothermal silicification, as well as the combination of all of these processes.

The presence of traces minerals like svanbergite–goyazite, were described in the Campos Basin using XRD (Herlinger et al., 2017; Lima & De Ros, 2019); suggest that they are associated with the silicification and dolomitization processes. In addition, the presence of barite and fluorite are possibly related to fluid reaction, carried by faults and fractures in the Pre–Salt carbonates of Campos Basin (Herlinger et al., 2017).

Furthermore, the petrophysical properties of the Pre–Salt carbonates display a complex link between heterogenous facies distribution and high–quality reservoirs. Gomes et al. (2020) emphasize a scale–dependency factor when the proportion of facies distribution in centimeter scale is upscaled, which may induce losses in facies proportions and subsequently depositional and diagenetic information. However, for the overall reservoir petrophysics characterization, our analysis suggests that the main trends of reservoir characteristics are consistent in a field scale, and relevant input data to the reservoir modeling.

Nevertheless, a more complete characterization could be implemented by additional analytical techniques to improve the petrophysical evaluation, integrating core–plug NMR data with mercury intrusion capillary pressure measures, and tomography measurements applied to rock samples in multiscale to better address the scale factor of facies and diagenesis impact on the petrophysical evaluation (Alabi et al., 2014; Chitale et al., 2015; Basso et al., 2020; Haagsma et al., 2021). Furthermore, although the post–depositional processes play a key role in the reservoir quality, a better understanding of facies distribution may help the prediction of zones with preferential alteration (i.e., dolomitized/vug–prone zones).

Finally, additional investigations in the characterization of diagenetic, post–depositional and possible hydrothermal processes need to be evaluated for better comprehension of these impacts in the reservoir quality petrophysical framework. Therefore, the reconstruction of the carbonate paleoenvironment may contribute to

improve the prediction of the reservoir quality within mature fields and analogue areas.

3.6.2 Reservoir heterogeneities and flow barriers

The presence of heterogeneities controlling the reservoir quality may create barriers for fluid flow and affect the displacement of hydrocarbons in the reservoir. The stratigraphic variation and the influence of dissolution, silicification and dolomitization effects described in this study seems to corroborate that the BVF presents highly heterogeneous reservoir quality controls. The variation of porosity and permeability addressed in previous studies of the Brazilian Pre–Salt carbonates indicated that the petrophysical properties can be diagenetically enhanced or reduced (Rezende and Pope, 2015; Herlinger et al., 2017; Basso et al., 2020; Belila et al., 2020).

In addition, NMR data showed that the Pre–Salt porosity is mainly comprised of free fluid porosity, associated with dissolution, silicification and dolomitization effects, which represents a key factor in the reservoir petrophysical quality, at the Sapinhoá field. The definition of an accurate NMR T2–cutoff is another important subject to be addressed, because higher values of T2 cutoffs were described in a study of the BVF based a small core–plug dataset (Belila et al., 2020). Therefore, we recommend a laboratorial T2 cutoff evaluation valuation based on a substantial number of rock samples, to better calibrate the partitions of NMR porosity logs to better address the petrophysical heterogeneities presented in the BVF.

Results presented in this research indicated a wide range of porosity and permeability distribution in the BVF; and in all facies we could observe important variation in high flow unit distribution (HFU 3 to 5), as well as flow units with less porosity and permeability ranges (HFU 1 and 2). The wide range of porosity and permeability suggests a non–preferential lithological constraint controlling the BVF interval, because a single flow unit is composed by several facies, differently from typically seen in siliciclastic reservoir types where a single facies usually represented a flow unit (e.g., Radwan et al., 2021). Furthermore, similar results were described in the Mero field at Santos Basin for the BVF (Penna and Lupinacci, 2020), in which several facies constrain a singular flow unit. In that case, the lithology was generically

addressed as carbonate reservoir, non–reservoir, and microporous sediments in flow unit evaluation.

The presence of multiple carbonate facies comprising a single flow unit corroborate that the heterogeneities found on the reservoir quality are products of the complex diagenetic history of the BVF. Although tight zones are found within the analyzed BVF wells, as shown in the well–logs and RCAL porosity, apparently these intervals display no significant impact in production wells located in the structural high. However, additional investigations must be addressed at the field production scale, and formation testers and production logging analysis can provide useful insights for the hydrocarbon production of Sapinhoá field.

Lastly, the variation in petrophysical distribution presented in this study, showed that best flow unit zones (HFU 4 and 5) are usually found in the intervals above the FWL, which maximizes the hydrocarbon production in the BVF. The key element found is the presence of elevated porosity and permeability ranges, that generate quality flow units, in which the presence of enhanced porosity processes has a meaningful impact in this carbonate reservoir.

3.7 CONCLUSIONS

An overview of the formation evaluation of the Pre–Salt carbonate reservoir was carried–out in the Sapinhoá field, integrating multiscale data supported by well–logging, cores, core–plugs, side–wall cores, and thin section information.

Evidence of dissolution processes appears at micro and macro scales, and intensive degree dissolution processes is a relevant element that may connect the pore space. The interparticle porosity connection may create vugs, and additionally, highly porous zones. Moreover, repetitive patterns of secondary porosity were identified occurring in all wells. This feature mainly appeared as stratabound vug features easily identified at cores and BHI, also suggesting the enhancement in the free fluid porosity of the BVF lacustrine carbonates.

In addition, the dolomitized intervals are associated with the enhancement of the reservoir quality, and silicified intervals presented lower values of porosity and permeability. The dolomitization and silicification processes can also create tight zones within the BVF, as they partially impact these carbonates. Such diagenetic

processes can appear in isolated lateral intervals on field scale, that possibly represent no significant flow barrier. However, some of the tight dolomitized/silicified intervals still possess good petrophysical properties, because previous porosity is not entirely obliterated, and they are found in intermediary flow units. In general, the injection wells located in the basinward area, presented tighter zones, which are usually richer in capillary bound porosity.

Additionally, the presence of dolomitized and silicified intervals close to fractures and breccias intervals, as well as the presence of unusual minerals (like barite and fluorite) even in few concentrations, may be a hint of the contribution of hydrothermal heated fluids, migrated through fault focusing mechanism on the Brazilian Pre–Salt carbonates.

In conclusion, the main key factor that affects the reservoir quality is the secondary porosity, which appears enhanced through dissolution, and dolomitization processes creating and connecting the pore spaces of the Pre-Salt reservoir. These processes generated flow units of higher porosity and permeability within the hydrocarbon saturated intervals along the structural high, in which several facies contributes to the composition of each one of the flow units. In addition, a high contribution of pervasive silicification and dolomitization processes can either reduce or obliterate the reservoir quality of these rocks decreasing the porosity and permeability, as well as create tighter zones on the wells located at the basinward area.

3.8 ACKNOWLEDGEMENTS

3.9 CREDIT AUTHOR STATEMENT

Hugo Tamoto: Conceptualization, Methodology, Investigation, Software, Writing – original draft. André Luiz Silva Pestilho: Formal Analysis, Writing – review & editing, Anelize Bahniuk: Supervision, Writing – review & editing.

3.10 REFERENCES OF THE MANUSCRIPT SUBMITED, ACCORDING TO THE AAPG JOURNAL STYLE

Alabi, G., R. Kasten, V. Chitale, S. Yadavalli, L. Piccoli, and B. P. Brazil, 2014, THE VALUE OF PETROPHYSICAL MEASUREMENTS ACROSS MULTIPLE SCALES – A LACUSTRINE CARBONATE EXAMPLE FROM CAMPOS BASIN , BRAZIL, *in* SPWLA 55th Annual Logging Symposium 2014: Society of Petrophysicists and Well Log Analysts, p. 12.

Amaefule, J. O., M. Altunbay, D. Tiab, D. G. Kersey, and D. K. Keelan, 1993, Enhanced reservoir description: using core and log data to identify hydraulic (flow) units and predict permeability in uncored intervals/ wells: Proceedings - SPE Annual Technical Conference and Exhibition, v. Omega, no. c, p. 205–220, doi:10.2523/26436-ms.

Baouche, R., S. Sen, S. S. Ganguli, and H. A. Feriel, 2021, Petrophysical, geomechanical and depositional environment characterization of the Triassic TAGI reservoir from the Hassi Berkine South field, Berkine Basin, Southeastern Algeria: Journal of Natural Gas Science and Engineering, v. 92, no. April, p. 104002, doi:10.1016/j.jngse.2021.104002.

Basso, M., A. M. P. Belila, G. F. Chinelatto, J. P. da P. Souza, and A. C. Vidal, 2021, Sedimentology and petrophysical analysis of pre-salt lacustrine carbonate reservoir from the Santos Basin, southeast Brazil: International Journal of Earth Sciences, v. 110, no. 7, p. 2573–2595, doi:10.1007/s00531-020-01932-7.

Belila, A. M. P., M. Basso, G. F. Chinelatto, M. C. Kuroda, and A. C. Vidal, 2020, Pore typing using nuclear magnetic resonance, an example with samples from cretaceous pre-salt lacustrine carbonates in the Santos Basin, Brazil: Journal of

Petroleum Science and Engineering, v. 190, no. February, p. 107079, doi:10.1016/j.petrol.2020.107079.

Bigelow, E. L., 1993, Petrophysical and geological impact of borehole images, in Society of Petroleum Engineers Western Regional Meeting: p. 345–354, doi:10.2523/26064-ms.

Bize-Forest, N., R. Centeno, E. Bize, R. Polinski, A. Boyd, R. Oliveira, A. He, and I. Le Nir, 2014, Vug porosity estimation using acoustic images in oil or water-based mud systems, in EAGE Borehole Geology Workshop: Optimising the Use of Your Borehole Image Data.: p. 3, doi:10.3997/2214-4609.20142320.

Bize-Forest, N., L. Laura, V. Baines, A. Boyd, F. Abbots, and A. Barnett, 2018, Using Machine-Learning for Depositional Facies Prediction in a Complex Carbonate Reservoir, in SPWLA 59th Annual Logging Symposium: Society of Petrophysicists and Well Log Analysts, p. 11.

Boyd, A., A. Souza, G. Carneiro, V. Machado, W. Trevizan, B. Santos, P. Netto, R. Bagueira, R. Polinski, and A. Bertolini, 2015, Presalt Carbonate Evaluation for Santos Basin, Offshore Brazil: Petrophysics, v. 56, no. 06, p. 577–591.

Brelaz, L., M. Ribeiro, and I. Mendes, 2019, Análise petrofísica dos reservatórios carbonáticos microbiais da Formação Barra Velha, Pré-sal da Bacia de Santos, Brasil, in Proceedings of the 16th International Congress of the Brazilian Geophysical Society&Expogef: Brazilian Geophysical Society, p. 1–6, doi:10.22564/16cisbgf2019.047.

Carminatti, M., B. Wolff, and L. Gamboa, 2008, New Exploratory Frontiers In Brazil, in 19th World Petroleum Congress: OnePetro.

Chang, H. K., R. O. Kowsmann, F. A. M. Figueiredo, and A. A. Bender, 1992, Tectonics and stratigraphy of the East Brazil Rift system: an overview: Tectonophysics, v. 213, no. 1–2, p. 97–138, doi:10.1016/0040-1951(92)90253-3.

Chitale, V. D. V, G. Alabi, P. Gramin, S. Lepley, and L. Piccoli, 2015, Reservoir Characterization Challenges Due to the Multiscale Spatial Heterogeneity in the Presalt Carbonate Sag Formation, North Campos Basin, Brazil: PETROPHYSICS, v. 56, no. 6, p. 552–576.

Coates, G. R., L. Xiao, and M. G. Prammer, 1999, NMR Logging Principles and Applications: Elsevier Science, 260 p.

Davies, G. R., and L. B. Smith, 2006, Structurally controlled hydrothermal dolomite reservoir facies: An overview: AAPG Bulletin, v. 90, no. 11, p. 1641–1690, doi:10.1306/05220605164.

Demšar, J. et al., 2013, Orange: Data Mining Toolbox in Python: Journal of Machine Learning Research, v. 14, p. 2349–2353.

Dunham, R. J., 1962, Classification of Carbonate Rocks According to Depositional Texture: AAPG Symposium, v. 1, p. 108–121.

Ehigie, S. O., 2010, NMR-openhole log integration: Making the most of NMR data deliverables, *in* 34th Annual SPE International Conference and Exhibition held in Tinapa – Calabar, Nigeria: p. 203–213, doi:10.2118/136971-ms.

Ellis, D. V., and J. M. Singer, 2007, Nuclear Magnetic Logging, *in* Well Logging for Earth Scientists: Springer Netherlands, p. 415–478, doi:10.1007/978-1-4020-4602-5_16.

Embry, A. F., and J. E. Klovan, 1971, A LATE DEVONIAN REEF TRACT ON NORTHEASTERN BANKS ISLAND, N.W.T.: Bulletin of Canadian Petroleum Geology, v. 19, no. 4, p. 730–781, doi:10.35767/GSCPGBULL.19.4.730.

Fan, H., J. Shi, T. Fan, Zhiqian Gao, Y. Gu, Ze Gao, T. Zhang, Y. Li, and B. Li, 2021, Sedimentary microfacies analysis of carbonate formation based on FMI and conventional logs: A case study from the ordovician in the Tahe Oilfield, Tarim Basin,

China: Journal of Petroleum Science and Engineering, v. 203, no. March, p. 15, doi:10.1016/j.petrol.2021.108603.

Faria, D. L. de P., A. Tadeu dos Reis, and O. Gomes de Souza, 2017, Three-dimensional stratigraphic-sedimentological forward modeling of an Aptian carbonate reservoir deposited during the sag stage in the Santos basin, Brazil: Marine and Petroleum Geology, v. 88, p. 676–695, doi:10.1016/j.marpetgeo.2017.09.013.

Farias, F., P. Szatmari, A. Bahniuk, and A. B. França, 2019, Evaporitic carbonates in the pre-salt of Santos Basin – Genesis and tectonic implications: Marine and Petroleum Geology, v. 105, p. 251–272, doi:10.1016/j.marpetgeo.2019.04.020.

Gomes, J. P., R. B. Bunevich, L. R. Tedeschi, M. E. Tucker, and F. F. Whitaker, 2020, Facies classification and patterns of lacustrine carbonate deposition of the Barra Velha Formation, Santos Basin, Brazilian Pre-salt: Marine and Petroleum Geology, v. 113, no. 104176, p. 21, doi:10.1016/j.marpetgeo.2019.104176.

Haagsma, A., M. Scharenberg, L. Keister, J. Schuetter, and N. Gupta, 2021, Secondary porosity prediction in complex carbonate reefs using 3D CT scan image analysis and machine learning: Journal of Petroleum Science and Engineering, v. 207, no. October 2020, p. 18, doi:10.1016/j.petrol.2021.109087.

Hemenway, M. A., and S. E. Kaczmarek, 2021, High-resolution chemostratigraphy in carbonate mudstones: Salina A-1 carbonate (Silurian), Michigan Basin, U.S.A.: Marine and Petroleum Geology, v. 126, no. 104918, p. 18, doi:10.1016/j.marpetgeo.2021.104918.

Herlinger, R., G. Do Nascimento Freitas, C. D. W. Dos Anjos, and L. F. De Ros, 2020, Petrological and petrophysical implications of magnesian clays in brazilian pre-salt deposits, in SPWLA 61st Annual Logging Symposium: Society of Petrophysicists and Well Log Analysts (SPWLA), p. 13, doi:10.30632/SPWLA-5004.

Herlinger, R., and B. C. C. Dos Santos, 2018, The impact of pore type on NMR T2 and micp in bioclastic carbonate reservoirs, *in* SPWLA 59th Annual Logging Symposium 2018: Society of Petrophysicists and Well Log Analysts (SPWLA), p. 10.

Herlinger, R., E. E. Zambonato, and L. F. De Ros, 2017, Influence of Diagenesis On the Quality of Lower Cretaceous Pre-salt Lacustrine Carbonate Reservoirs from Northern Campos Basin, Offshore Brazil: Journal of Sedimentary Research, v. 87, no. 12, p. 1285–1313, doi:10.2110/jsr.2017.70.

Koren, Y., and L. Carmel, 2003, Visualization of labeled data using linear transformations: Proceedings - IEEE Symposium on Information Visualization, INFO VIS, p. 121–130, doi:10.1109/infvis.2003.1249017.

Lai, J. et al., 2018, A review on the applications of image logs in structural analysis and sedimentary characterization: Marine and Petroleum Geology, v. 95, no. May, p. 139–166, doi:10.1016/j.marpetgeo.2018.04.020.

Lai, J., X. Pang, Q. Xiao, Y. Shi, H. Zhang, T. Zhao, J. Chen, G. Wang, and Z. Qin, 2019, Prediction of reservoir quality in carbonates via porosity spectrum from image logs: Journal of Petroleum Science and Engineering, v. 173, p. 197–208, doi:10.1016/j.petrol.2018.10.022.

LI, J., Y. WANG, C. LIU, D. DONG, and Z. GAO, 2016, Hydrothermal fluid activity and the quantitative evaluation of its impact on carbonate reservoirs: A case study of the Lower Paleozoic in the west of Dongying sag, Bohai Bay Basin: Petroleum Exploration and Development, v. 43, no. 3, p. 395–403, doi:10.1016/S1876-3804(16)30046-5.

Lima, B. E. M., and L. F. De Ros, 2019, Deposition, diagenetic and hydrothermal processes in the Aptian Pre-Salt lacustrine carbonate reservoirs of the northern Campos Basin, offshore Brazil: Sedimentary Geology, v. 383, p. 55–81, doi:10.1016/j.sedgeo.2019.01.006.

Lima, B. E. M., L. R. Tedeschi, A. L. S. Pestilho, R. V. Santos, J. C. Vazquez, J. V. P. Guzzo, and L. F. De Ros, 2020, Deep-burial hydrothermal alteration of the Pre-Salt carbonate reservoirs from northern Campos Basin, offshore Brazil: Evidence from petrography, fluid inclusions, Sr, C and O isotopes: Marine and Petroleum Geology, v. 113, no. 104143, p. 25, doi:10.1016/j.marpetgeo.2019.104143.

Menezes, C. P., F. H. R. Bezerra, F. Balsamo, M. Mozafari, M. M. Vieira, N. K. Srivastava, and D. L. de Castro, 2019, Hydrothermal silicification along faults affecting carbonate-sandstone units and its impact on reservoir quality, Potiguar Basin, Brazil: Marine and Petroleum Geology, v. 110, p. 198–217, doi:10.1016/j.marpetgeo.2019.07.018.

Mohriak, W. U., L. V. Perdomo, D. M. Plucenio, and J. L. Saad, 2015, Challenges for petrophysical characterization of presalt carbonate reservoirs, *in* 14th International Congress of the Brazilian Geophysical Society: SBGf, p. 623–627, doi:10.1190/sbgf2015-123.

Moreira, J. L. P., C. V Madeira, J. A. Gil, and M. A. P. Machado, 2007, Santos basin: Boletim de Geociencias da Petrobras, v. 15, no. 2, p. 531–549.

Muniz, M. C., and D. W. J. Bosence, 2015, Pre-salt microbialites from the Campos Basin (offshore Brazil): image log facies, facies model and cyclicity in lacustrine carbonates, *in* D. W. J. Bosence, K. A. Gibbons, D. P. Le Heron, W. A. Morgan, and B. A. Pritchard, T.& Vining, eds., Microbial Carbonates in Space and Time: Implications for Global Exploration and Production.: London, Geological Society, London, Special Publications, doi:10.1144/SP418.10.

Pedregosa, F. et al., 2011, Scikit-learn: Machine Learning in Python: Journal of Machine Learning Research, v. 12, p. 2825–2830.

Penna, R., and W. M. Lupinacci, 2020, Decameter-scale flow-unit classification in Brazilian presalt carbonates: SPE Reservoir Evaluation and Engineering, v. 23, no. 4, p. 1420–1439, doi:10.2118/201235-PA.

Radwan, A. A., B. S. Nabawy, A. Abdelmaksoud, and A. Lashin, 2021, Integrated sedimentological and petrophysical characterization for clastic reservoirs: A case study from New Zealand: Journal of Natural Gas Science and Engineering, v. 88, no. 103797, p. 25, doi:10.1016/j.jngse.2021.103797.

Rezende, M. F., and M. C. Pope, 2015, Importance of depositional texture in pore characterization of subsalt microbialite carbonates, offshore Brazil: Geological Society Special Publication, v. 418, no. 1, p. 193–207, doi:10.1144/SP418.2.

Rider, M. H., 2011, Geological Interpretation of Well Logs: Sutherland, Rider-French Consulting Limite, 440 p.

Sabato Ceraldi, Teresa, and D. Green, 2017, Evolution of the South Atlantic lacustrine deposits in response to Early Cretaceous rifting, subsidence and lake hydrology, in T. Sabato Ceraldi, R. A. Hodgkinson, and G. Backe, eds., Petroleum Geoscience of the West Africa Margin.: The Geological Society of London, p. 77–98, doi:10.1144/SP438.10.

Saller, A., S. Rushton, L. Buambua, K. Inman, R. McNeil, and J. A. D. (Tony) Dickson, 2016, Presalt stratigraphy and depositional systems in the Kwanza Basin, offshore Angola: AAPG Bulletin, v. 100, no. 07, p. 1135–1164, doi:10.1306/02111615216.

Teboul, P.-A., J.-M. Kluska, N. C. M. Marty, M. Debure, C. Durlet, A. Virgone, and E. C. Gaucher, 2016, Volcanic rock alterations of the Kwanza Basin, offshore Angola - Insights from an integrated petrological, geochemical and numerical approach: Marine and Petroleum Geology, v. 80, p. 394–411, doi:10.1016/j.marpetgeo.2016.12.020.

Terra, G. G. S. et al., 2010, Classificação de rochas carbonáticas aplicável às bacias sedimentares brasileiras.: Boletim de Geociencias da Petrobras, v. 18, p. 9–29.

Tosca, N. J., and V. P. Wright, 2015, Diagenetic pathways linked to labile Mg-clays in lacustrine carbonate reservoirs: A model for the origin of secondary porosity in the

Cretaceous pre-salt Barra Velha Formation, offshore Brazil, *in* P. J. Armitage, A. R. Butcher, J. M. Churchill, A. E. Csoma, C. Hollis, R. H. Lander, J. E. Omma, and R. H. Worden, eds., Reservoir Quality of Clastic and Carbonate Rocks: Analysis, Modelling and Prediction.: London, The Geological Society of London, p. 33–46, doi:10.1144/SP435.1.

Valle, B., P. F. Dal' Bó, J. Santos, L. Aguiar, P. Coelho, J. Favoreto, M. Arena, H. N. Santos, C. Ribeiro, and L. Borghi, 2021, A new method to improve the NMR log interpretation in drilling mud-invaded zones: A case study from the Brazilian Pre-salt: Journal of Petroleum Science and Engineering, v. 203, no. 108692, p. 14, doi:10.1016/j.petrol.2021.108692.

Viera de Luca, P. H. et al., 2017, Breaking barriers and paradigms in presalt exploration: The pão de açúcar discovery (Offshore Brazil), *in* R. K. Merrill, and C. A. Sternbach, eds., Giant fields of the decade 2000–2010: AAPG Memoir 113: The American Association of Petroleum Geologists, p. 177–193, doi:10.1306/13572007M1133686.

Williams, P. D., R. H. Maddock, A. K. Sapru, and M. J. F. Lawrence, 2000, Analysis of a fractured carbonate reservoir (thamama group) using borehole images from an horizontal well, offshore UAE: Society of Petroleum Engineers - Abu Dhabi International Petroleum Exhibition and Conference 2000, ADIPEC 2000, v. 1, no. iii, p. 1–9.

Worden, R. H., P. J. Armitage, A. R. Butcher, J. M. Churchill, A. E. Csoma, C. Hollis, R. H. Lander, and J. E. Omma, 2018, Petroleum reservoir quality prediction: Overview and contrasting approaches from sandstone and carbonate communities, *in* R. H. Armitage, P. J., Butcher, A. R., Churchill, J. M., Csoma, A. E., Hollis, C., Lander, R. H., Omma,J.E.& Worden, ed., Geological Society Special Publication: London, The Geological Society of London, p. 1–31, doi:10.1144/SP435.21.

Wright, V. P., 2020, The mantle, CO 2 and the giant Aptian chemogenic lacustrine carbonate factory of the South Atlantic: Some carbonates are made, not born: Sedimentology, p. 27, doi:10.1111/sed.12835.

Wright, V. P., and A. J. Barnett, 2015, An abiotic model for the development of textures in some South Atlantic early Cretaceous lacustrine carbonates: Geological Society, London, Special Publications, v. 418, no. 1, p. 209–219, doi:10.1144/SP418.3.

Zalán, P., K. Rodriguez, and M. Cvetkovic, 2019, Extraordinary Remaining Potential in the Pre-Salt of Santos Basin, *in* 16th International Congress of the Brazilian Geophysical Society: SBGf, p. 1–8, doi:10.22564/16cisbgf2019.128.

4 CONSIDERAÇÕES FINAIS

Uma visão geral da avaliação dos carbonatos da Formação Barra velha do Pré-Sal foi realizada no campo de Sapinhoá, integrando dados em diferentes escalas, utilizando informações de perfilagem de poços, testemunhos, plugues de testemunho, amostras laterais e de seções delgadas.

Evidências de processos de dissolução de argila magnesiana aparecem em escala micro e macro, e em intenso grau. Esses elementos são relevantes, pois ocorrem em toda seção da Formação Barra Velha e conectam os espaços porosos. A conexão de porosidade entre as partículas pode criar *vugs* e, adicionalmente, intervalos/zonas altamente porosas. Além disso, padrões repetitivos de porosidade secundária foram identificados ocorrendo em todos os poços estudados, que aparecem principalmente em camadas/estratos com claras evidências de porosidade vugular, vistos nas amostras e em perfil de imagem; sugerindo também o aumento da porosidade tipo fluido livre nesses carbonatos lacustres.

Adicionalmente, foi observado que os intervalos dolomitizados estão associados à melhoria da qualidade do reservatório, e os silicificados, à diminuição de valores de porosidade e permeabilidade. No entanto, esses processos também podem criam zonas fechadas/apertadas dentro da Formação Barra Velha, quando impactam as rochas de forma parcial; tal impacto pode aparecer localmente como intervalos lateralmente isolados e, possivelmente, não representam barreiras de fluxo significativa, pois o espaço poroso e sua conectividade não estão totalmente obliterados. Ainda assim, algumas zonas fechadas/apertadas dolomitizados/silicificados podem possuir boas propriedades de porosidade e permeabilidade, e compreendem unidades de fluxo intermediárias. Em geral, os poços injetores localizados nos flancos da estrutura principal do campo de Sapinhoá apresentaram zonas mais fechadas, geralmente mais ricas em intervalos de porosidade tipo capilar.

Ademais, foram identificados a presença de intervalos dolomitizados e silicificados próximos a fraturas e brechas, bem como a de minerais incomuns, como barita e fluorita. Mesmo que em pouca concentração, no contexto dos reservatórios da Formação Barra Velha; sugerem indícios da contribuição de fluidos hidrotermais aquecidos, migrados através do mecanismo de focalização de falhas.

Em conclusão, o principal fator-chave que controla a qualidade do reservatório é a porosidade secundária, gerada por meio de processos de dissolução e de argila magnesiana e dolomitização criando conectividade entre os espaços porosos dos carbonatos da Formação Barra Velha. Esses processos geraram zonas de fluxo de altas porosidade e permeabilidades compreendendo os intervalos saturados por hidrocarbonetos dentro ao longo do alto estrutural; nota-se ainda que várias litofácies contribuem na composição individual das cinco unidades de fluxo. Adicionalmente, a alta contribuição de silicificação pervasiva pode reduzir ou obliterar a qualidade do reservatório diminuindo a porosidade e permeabilidade; assim como gerar zonas fechadas/apertadas nos poços localizados nos flancos da estrutura principal do campo de Sapinhoá.

REFERÊNCIAS DE ACORDO COM AS NORMAS DO PROGRAMA DE PÓS-GRADUAÇÃO EM GEOLOGIA

Alabi, G., R. Kasten, V. Chitale, S. Yadavalli, L. Piccoli, and B. P. Brazil, 2014, THE VALUE OF PETROPHYSICAL MEASUREMENTS ACROSS MULTIPLE SCALES – A LACUSTRINE CARBONATE EXAMPLE FROM CAMPOS BASIN , BRAZIL, *in* SPWLA 55th Annual Logging Symposium 2014: Society of Petrophysicists and Well Log Analysts, p. 12.

Amaefule, J. O., M. Altunbay, D. Tiab, D. G. Kersey, and D. K. Keelan, 1993, Enhanced reservoir description: using core and log data to identify hydraulic (flow) units and predict permeability in uncored intervals/ wells: Proceedings - SPE Annual Technical Conference and Exhibition, v. Omega, no. c, p. 205–220, doi:10.2523/26436-ms.

API, 1998, Recommended practices for core analysis: Washington, D.C, American Petroleum Institute.

Baouche, R., S. Sen, S. S. Ganguli, and H. A. Feriel, 2021, Petrophysical, geomechanical and depositional environment characterization of the Triassic TAGI reservoir from the Hassi Berkine South field, Berkine Basin, Southeastern Algeria: Journal of Natural Gas Science and Engineering, v. 92, no. April, p. 104002, doi:10.1016/j.jngse.2021.104002.

Barnett, A. J., V. P. Wright, V. S. Chandra, and V. Jain, 2018, Distinguishing between eogenetic, unconformity-related and mesogenetic dissolution: A case study from the Panna and Mukta fields, offshore Mumbai, India: Geological Society Special Publication, v. 435, no. 1, p. 67–84, doi:10.1144/SP435.12.

Basso, M., A. M. P. Belila, G. F. Chinelatto, J. P. da P. Souza, and A. C. Vidal, 2021, Sedimentology and petrophysical analysis of pre-salt lacustrine carbonate reservoir from the Santos Basin, southeast Brazil: International Journal of Earth Sciences, v. 110, no. 7, p. 2573–2595, doi:10.1007/s00531-020-01932-7.

Belila, A. M. P., M. Basso, G. F. Chinelatto, M. C. Kuroda, and A. C. Vidal, 2020, Pore typing using nuclear magnetic resonance, an example with samples from cretaceous pre-salt lacustrine carbonates in the Santos Basin, Brazil: Journal of Petroleum Science and Engineering, v. 190, no. February, p. 107079, doi:10.1016/j.petrol.2020.107079.

Bigelow, E. L., 1993, Petrophysical and geological impact of borehole images, *in* Society of Petroleum Engineers Western Regional Meeting: p. 345–354, doi:10.2523/26064-ms.

Bize-Forest, N., R. Centeno, E. Bize, R. Polinski, A. Boyd, R. Oliveira, A. He, and I. Le Nir, 2014, Vug porosity estimation using acoustic images in oil or water-based mud systems, *in* EAGE Borehole Geology Workshop: Optimising the Use of Your Borehole Image Data.: p. 3, doi:10.3997/2214-4609.20142320.

Bize-Forest, N., L. Laura, V. Baines, A. Boyd, F. Abbots, and A. Barnett, 2018, Using Machine-Learning for Depositional Facies Prediction in a Complex Carbonate Reservoir, *in* SPWLA 59th Annual Logging Symposium: Society of Petrophysicists and Well Log Analysts, p. 11.

Boyd, A., A. Souza, G. Carneiro, V. Machado, W. Trevizan, B. Santos, P. Netto, R. Bagueira, R. Polinski, and A. Bertolini, 2015, Presalt Carbonate Evaluation for Santos Basin, Offshore Brazil: Petrophysics, v. 56, no. 06, p. 577–591.

Brelaz, L., M. Ribeiro, and I. Mendes, 2019, Análise petrofísica dos reservatórios carbonáticos microbiais da Formação Barra Velha, Pré-sal da Bacia de Santos, Brasil, *in* Proceedings of the 16th International Congress of the Brazilian Geophysical Society&Expogef: Brazilian Geophysical Society, p. 1–6, doi:10.22564/16cisbgf2019.047.

Carminatti, M., B. Wolff, and L. Gamboa, 2008, New Exploratory Frontiers In Brazil, *in* 19th World Petroleum Congress: OnePetro.

Chang, H. K., R. O. Kowsmann, F. A. M. Figueiredo, and A. A. Bender, 1992, Tectonics and stratigraphy of the East Brazil Rift system: an overview: Tectonophysics, v. 213, no. 1–2, p. 97–138, doi:10.1016/0040-1951(92)90253-3.

Chitale, V. D. V, G. Alabi, P. Gramin, S. Lepley, and L. Piccoli, 2015, Reservoir Characterization Challenges Due to the Multiscale Spatial Heterogeneity in the Presalt Carbonate Sag Formation, North Campos Basin, Brazil: PETROPHYSICS, v. 56, no. 6, p. 552–576.

Chitale, V., G. Alabi, R. Kasten, A. Taylor, and P. Hoenmans, 2014, Learning from deployment of a variety of modern petrophysical formation evaluation technologies and techniques for characterization of a pre-salt carbonate reservoir: Case study from campos basin, brazil: SPWLA 55th Annual Logging Symposium 2014. Coates, G. R., L. Xiao, and M. G. Prammer, 1999, NMR Logging Principles and Applications: Elsevier Science, 260 p.

Davies, G. R., and L. B. Smith, 2006, Structurally controlled hydrothermal dolomite reservoir facies: An overview: AAPG Bulletin, v. 90, no. 11, p. 1641–1690, doi:10.1306/05220605164.

Demšar, J. et al., 2013, Orange: Data Mining Toolbox in Python: Journal of Machine Learning Research, v. 14, p. 2349–2353.

Dowsett, M., R. Wiesinger, and M. Adriaens, 2021, Chapter 6 - X-ray diffraction: Elsevier Inc., 161–207 p., doi:10.1016/B978-0-12-818860-6.00011-8.

Dunham, R. J., 1962, Classification of Carbonate Rocks According to Depositional Texture: AAPG Symposium, v. 1, p. 108–121.

Ehigie, S. O., 2010, NMR-openhole log integration: Making the most of NMR data deliverables, *in* 34th Annual SPE International Conference and Exhibition held in Tinapa – Calabar, Nigeria: p. 203–213, doi:10.2118/136971-ms.

Ellis, D. V., and J. M. Singer, 2007a, Nuclear Magnetic Logging, *in* Well Logging for Earth Scientists: Springer Netherlands, p. 415–478, doi:10.1007/978-1-4020-4602-5_16.

Ellis, D. V., and J. M. Singer, 2007b, Well Logging for Earth Scientists: Dordrecht, Springer Netherlands, 708 p., doi:10.1007/978-1-4020-4602-5.

Embry, A. F., and J. E. Klovan, 1971, A LATE DEVONIAN REEF TRACT ON NORTHEASTERN BANKS ISLAND, N.W.T.: Bulletin of Canadian Petroleum Geology, v. 19, no. 4, p. 730–781, doi:10.35767/GSCPGBULL.19.4.730.

Fan, H., J. Shi, T. Fan, Zhiqian Gao, Y. Gu, Ze Gao, T. Zhang, Y. Li, and B. Li, 2021, Sedimentary microfacies analysis of carbonate formation based on FMI and conventional logs: A case study from the ordovician in the Tahe Oilfield, Tarim Basin, China: Journal of Petroleum Science and Engineering, v. 203, no. March, p. 15, doi:10.1016/j.petrol.2021.108603.

Faria, D. L. de P., A. Tadeu dos Reis, and O. Gomes de Souza, 2017, Three-dimensional stratigraphic-sedimentological forward modeling of an Aptian carbonate reservoir deposited during the sag stage in the Santos basin, Brazil: Marine and Petroleum Geology, v. 88, p. 676–695, doi:10.1016/j.marpetgeo.2017.09.013.

Farias, F., P. Szatmari, A. Bahniuk, and A. B. França, 2019, Evaporitic carbonates in the pre-salt of Santos Basin – Genesis and tectonic implications: Marine and Petroleum Geology, v. 105, p. 251–272, doi:10.1016/j.marpetgeo.2019.04.020. Gomes, J. P., R. B. Bunevich, L. R. Tedeschi, M. E. Tucker, and F. F. Whitaker, 2020, Facies classification and patterns of lacustrine carbonate deposition of the Barra Velha Formation, Santos Basin, Brazilian Pre-salt: Marine and Petroleum Geology, v. 113, no. 104176, p. 21, doi:10.1016/j.marpetgeo.2019.104176.

Haagsma, A., M. Scharenberg, L. Keister, J. Schuetter, and N. Gupta, 2021, Secondary porosity prediction in complex carbonate reefs using 3D CT scan image analysis and machine learning: Journal of Petroleum Science and Engineering, v. 207, no. October 2020, p. 18, doi:10.1016/j.petrol.2021.109087.

Hasiuk, F. J., and S. E. Kaczmarek, 2015, SEM-Evidence of Biotic Influence in Brazilian Pre-Salt Carbonates: AAPG Annual Conference and Exhibition, v. 51190, p. 2015.

Hemenway, M. A., and S. E. Kaczmarek, 2021, High-resolution chemostratigraphy in carbonate mudstones: Salina A-1 carbonate (Silurian), Michigan Basin, U.S.A.: Marine and Petroleum Geology, v. 126, no. 104918, p. 18, doi:10.1016/j.marpetgeo.2021.104918.

Herlinger, R., G. Do Nascimento Freitas, C. D. W. Dos Anjos, S. A. Petróleo Brasileiro, and L. F. De Ros, 2020, Petrological and petrophysical implications of magnesian clays in brazilian pre-salt deposits, *in* SPWLA 61st Annual Logging Symposium: Society of Petrophysicists and Well Log Analysts (SPWLA), p. 13, doi:10.30632/SPWLA-5004.

Herlinger, R., and B. C. C. Dos Santos, 2018, The impact of pore type on NMR T2 and micp in bioclastic carbonate reservoirs, *in* SPWLA 59th Annual Logging Symposium 2018: Society of Petrophysicists and Well Log Analysts (SPWLA), p. 10.

Herlinger, R., E. E. Zambonato, and L. F. De Ros, 2017, Influence of Diagenesis On the Quality of Lower Cretaceous Pre-salt Lacustrine Carbonate Reservoirs from Northern Campos Basin, Offshore Brazil: Journal of Sedimentary Research, v. 87, no. 12, p. 1285–1313, doi:10.2110/jsr.2017.70.

Jenkins, R., and R. Snyder, 2012, Introduction to X-Ray Powder Diffractometry.: Wiley-Interscience, 428 p.

Koren, Y., and L. Carmel, 2003, Visualization of labeled data using linear transformations: Proceedings - IEEE Symposium on Information Visualization, INFO VIS, p. 121–130, doi:10.1109/infvis.2003.1249017.

Lai, J. et al., 2018, A review on the applications of image logs in structural analysis and sedimentary characterization: Marine and Petroleum Geology, v. 95, no. May, p. 139–166, doi:10.1016/j.marpetgeo.2018.04.020.

Lai, J., X. Pang, Q. Xiao, Y. Shi, H. Zhang, T. Zhao, J. Chen, G. Wang, and Z. Qin, 2019, Prediction of reservoir quality in carbonates via porosity spectrum from image logs: Journal of Petroleum Science and Engineering, v. 173, p. 197–208, doi:10.1016/j.petrol.2018.10.022.

Lai, J., G. Wang, Z. Fan, Z. Wang, J. Chen, Z. Zhou, S. Wang, and C. Xiao, 2017, Fracture detection in oil-based drilling mud using a combination of borehole image and sonic logs: Marine and Petroleum Geology, v. 84, p. 195–214, doi:10.1016/j.marpetgeo.2017.03.035.

Li, J., Y. Wang, C. Liu, D. Dong, and Z. Gao, 2016, Hydrothermal fluid activity and the quantitative evaluation of its impact on carbonate reservoirs: A case study of the Lower Paleozoic in the west of Dongying sag, Bohai Bay Basin: Petroleum Exploration and Development, v. 43, no. 3, p. 395–403, doi:10.1016/S1876-3804(16)30046-5.

Li, Q., X. You, Z. Jiang, S. Wu, and R. Zhang, 2020, Lithofacies and reservoir characterization of a source-controlled carbonate succession in a lacustrine rift basin, the Shulu Sag of Bohai Bay Basin, East China: Journal of Petroleum Science and Engineering, v. 192, no. September 2019, p. 107180, doi:10.1016/j.petrol.2020.107180.

Lima, B. E. M., and L. F. De Ros, 2019, Deposition, diagenetic and hydrothermal processes in the Aptian Pre-Salt lacustrine carbonate reservoirs of the northern Campos Basin, offshore Brazil: Sedimentary Geology, v. 383, p. 55–81, doi:10.1016/j.sedgeo.2019.01.006.

Lima, B. E. M., L. R. Tedeschi, A. L. S. Pestilho, R. V. Santos, J. C. Vazquez, J. V. P. Guzzo, and L. F. De Ros, 2020, Deep-burial hydrothermal alteration of the Pre-Salt carbonate reservoirs from northern Campos Basin, offshore Brazil: Evidence from

petrography, fluid inclusions, Sr, C and O isotopes: Marine and Petroleum Geology, v. 113, no. 104143, p. 25, doi:10.1016/j.marpetgeo.2019.104143.

Madrucci, V., A. R. Spadini, C. W. D. Dos Anjos, D. B. Alves, and S. M. C. Dos Anjos, 2013, Authigenic Magnesian Clays in Carbonate Reservoirs in Brazil, *in* International Meeting of Carbonate Sedimentologists: p. 1.

Makeen, Y. M., X. Shan, H. A. Ayinla, E. J. Adepehin, N. E. Ayuk, N. A. Yelwa, J. Yi, O. M. A. Elhassan, and D. Fan, 2021, Sedimentology, petrography, and reservoir quality of the Zarga and Ghazal formations in the Keyi oilfield, Muglad Basin, Sudan: Scientific Reports, v. 11, no. 1, p. 1–22, doi:10.1038/s41598-020-80831-y.

Menezes, C. P., F. H. R. Bezerra, F. Balsamo, M. Mozafari, M. M. Vieira, N. K. Srivastava, and D. L. de Castro, 2019, Hydrothermal silicification along faults affecting carbonate-sandstone units and its impact on reservoir quality, Potiguar Basin, Brazil: Marine and Petroleum Geology, v. 110, p. 198–217, doi:10.1016/j.marpetgeo.2019.07.018.

Mercedes-Martín, R., C. Ayora, J. Tritlla, and M. Sánchez-Román, 2019, The hydrochemical evolution of alkaline volcanic lakes: a model to understand the South Atlantic Pre-salt mineral assemblages: Earth-Science Reviews, v. 198, p. 102938, doi:10.1016/j.earscirev.2019.102938.

Mohriak, W. U., L. V. Perdomo, D. M. Plucenio, and J. L. Saad, 2015, Challenges for petrophysical characterization of presalt carbonate reservoirs, *in* 14th International Congress of the Brazilian Geophysical Society: SBGf, p. 623–627, doi:10.1190/sbgf2015-123.

Moreira, J. L. P., C. V Madeira, J. A. Gil, and M. A. P. Machado, 2007, Santos basin: Boletim de Geociencias da Petrobras, v. 15, no. 2, p. 531–549.
Muniz, M. C., and D. W. J. Bosence, 2018, Lacustrine carbonate platforms: Facies, cycles, and tectonosedimentary models for the presalt Lagoa Feia Group (Lower Cretaceous), Campos Basin, Brazil: AAPG Bulletin, v. 102, no. 12, p. 2569–2597, doi:10.1306/0511181620617087.

Muniz, M. C., and D. W. J. Bosence, 2015, Pre-salt microbialites from the Campos Basin (offshore Brazil): image log facies, facies model and cyclicity in lacustrine carbonates, *in* D. W. J. Bosence, K. A. Gibbons, D. P. Le Heron, W. A. Morgan, and B. A. Pritchard, T.& Vining, eds., Microbial Carbonates in Space and Time: Implications for Global Exploration and Production.: London, Geological Society, London, Special Publications, doi:10.1144/SP418.10.

Pedregosa, F. et al., 2011, Scikit-learn: Machine Learning in Python: Journal of Machine Learning Research, v. 12, p. 2825–2830.

Penna, R., and W. M. Lupinacci, 2020, Decameter-scale flow-unit classification in Brazilian presalt carbonates: SPE Reservoir Evaluation and Engineering, v. 23, no. 4, p. 1420–1439, doi:10.2118/201235-PA.

Petersohn, E., and M. Abelha, 2013, Libra Geological assessment report: <https://www.gov.br/anp/pt-br/rodadas-anp/rodadas-concluidas/partilha-de-producao/1a-rodada-partilha-producao-pre-sal/arquivos/seminarios/partilha1_tecnico_ambiental_ingles.pdf/view> (accessed October 12, 2021).

Pietzsch, R., D. M. Oliveira, L. R. Tedeschi, J. V Queiroz Neto, M. F. Figueiredo, J. C. Vazquez, and R. S. de Souza, 2018, Palaeohydrology of the Lower Cretaceous pre-salt lacustrine system, from rift to post-rift phase, Santos Basin, Brazil: Palaeogeography, Palaeoclimatology, Palaeoecology, v. 507, p. 60–80, doi:10.1016/j.palaeo.2018.06.043.

Pietzsch, R., L. R. Tedeschi, D. M. Oliveira, C. W. D. dos Anjos, J. C. Vazquez, and M. F. Figueiredo, 2020, Environmental conditions of deposition of the Lower Cretaceous lacustrine carbonates of the Barra Velha Formation, Santos Basin (Brazil), based on stable carbon and oxygen isotopes: A continental record of pCO2 during the onset of the Oceanic Anoxic Event: Chemical Geology, v. 535, p. 119457, doi:10.1016/j.chemgeo.2019.119457.

Radwan, A. A., B. S. Nabawy, A. Abdelmaksoud, and A. Lashin, 2021, Integrated sedimentological and petrophysical characterization for clastic reservoirs: A case study from New Zealand: Journal of Natural Gas Science and Engineering, v. 88, no. 103797, p. 25, doi:10.1016/j.jngse.2021.103797.

Rezende, M. F., and M. C. Pope, 2015, Importance of depositional texture in pore characterization of subsalt microbialite carbonates, offshore Brazil: Geological Society Special Publication, v. 418, no. 1, p. 193–207, doi:10.1144/SP418.2. Rider, M. H., 2011, Geological Interpretation of Well Logs: Sutherland, Rider-French Consulting Limite, 440 p.

Rios, E. H., P. F. de O. Ramos, A. L. M. Compan, R. Surmas, H. V. R. Camargo, D. A. Cruz, R. Skinner, V. de F. Machado, I. Figueiredo, and G. C. Stael, 2012, Petrofísica laboratorial no suporte à exploração e caracterização de reservatórios: p. cp-341-00098, doi:10.3997/2214-4609-PDB.341.99.

Sabato Ceraldi, Teresa, and D. Green, 2017, Evolution of the South Atlantic lacustrine deposits in response to Early Cretaceous rifting, subsidence and lake hydrology, in T. Sabato Ceraldi, R. A. Hodgkinson, and G. Backe, eds., Petroleum Geoscience of the West Africa Margin.: The Geological Society of London, p. 77–98, doi:10.1144/SP438.10.

Saller, A., S. Rushton, L. Buambua, K. Inman, R. McNeil, and J. A. D. (Tony) Dickson, 2016, Presalt stratigraphy and depositional systems in the Kwanza Basin, offshore Angola: AAPG Bulletin, v. 100, no. 07, p. 1135–1164, doi:10.1306/02111615216.

Schön, J. H., 2015, Pore Space Properties: p. 21–84, doi:10.1016/B978-0-08-100404-3.00002-0.

Souza, R. S. et al., 2018, Petrology of the Hydrothermal and Evaporitic Continental Cretaceous (Aptian) Pre-Salt Carbonates and Associated Rocks, South Atlantic Santos Basin, Offshore Brazil: AAPG ACE.

Teboul, P.-A., J.-M. Kluska, N. C. M. Marty, M. Debure, C. Durlet, A. Virgone, and E. C. Gaucher, 2016, Volcanic rock alterations of the Kwanza Basin, offshore Angola - Insights from an integrated petrological, geochemical and numerical approach: Marine and Petroleum Geology, v. 80, p. 394–411, doi:10.1016/j.marpetgeo.2016.12.020.

Terra, G. G. S. et al., 2010, Classificação de rochas carbonáticas aplicável às bacias sedimentares brasileiras.: Boletim de Geociencias da Petrobras, v. 18, p. 9–29.
Tiab, D., and E. C. Donaldson, 2016, Porosity and Permeability, *in* Petrophysics: Elsevier, p. 67–186, doi:10.1016/B978-0-12-803188-9.00003-6.

Tosca, N. J., and V. P. Wright, 2015, Diagenetic pathways linked to labile Mg-clays in lacustrine carbonate reservoirs: A model for the origin of secondary porosity in the Cretaceous pre-salt Barra Velha Formation, offshore Brazil, *in* P. J. Armitage, A. R. Butcher, J. M. Churchill, A. E. Csoma, C. Hollis, R. H. Lander, J. E. Omma, and R. H. Worden, eds., Reservoir Quality of Clastic and Carbonate Rocks: Analysis, Modelling and Prediction.: London, The Geological Society of London, p. 33–46, doi:10.1144/SP435.1.

Valle, B., P. F. Dal' Bó, J. Santos, L. Aguiar, P. Coelho, J. Favoreto, M. Arena, H. N. Santos, C. Ribeiro, and L. Borghi, 2021, A new method to improve the NMR log interpretation in drilling mud-invaded zones: A case study from the Brazilian Pre-salt: Journal of Petroleum Science and Engineering, v. 203, no. 108692, p. 14, doi:10.1016/j.petrol.2021.108692.

Viera de Luca, P. H. et al., 2017, Breaking barriers and paradigms in presalt exploration: The pão de açúcar discovery (Offshore Brazil), *in* R. K. Merrill, and C. A. Sternbach, eds., Giant fields of the decade 2000–2010: AAPG Memoir 113: The American Association of Petroleum Geologists, p. 177–193, doi:10.1306/13572007M1133686.

Williams, P. D., R. H. Maddock, A. K. Sapru, and M. J. F. Lawrence, 2000, Analysis of a fractured carbonate reservoir (thamama group) using borehole images from an horizontal well, offshore UAE: Society of Petroleum Engineers - Abu Dhabi International Petroleum Exhibition and Conference 2000, ADIPEC 2000, v. 1, no. iii, p. 1–9.

Worden, R. H., P. J. Armitage, A. R. Butcher, J. M. Churchill, A. E. Csoma, C. Hollis, R. H. Lander, and J. E. Omma, 2018, Petroleum reservoir quality prediction: Overview and contrasting approaches from sandstone and carbonate communities, *in* R. H. Armitage, P. J., Butcher, A. R., Churchill, J. M., Csoma, A. E., Hollis, C., Lander, R. H., Omma,J.E.& Worden, ed., Geological Society Special Publication: London, The Geological Society of London, p. 1–31, doi:10.1144/SP435.21.

Wright, V. P., 2020, The mantle, CO 2 and the giant Aptian chemogenic lacustrine carbonate factory of the South Atlantic: Some carbonates are made, not born: Sedimentology, p. 27, doi:10.1111/sed.12835.

Wright, V. Paul, and A. J. Barnett, 2015, An abiotic model for the development of textures in some South Atlantic early Cretaceous lacustrine carbonates, *in* D. W. J. Bosence, K. A. Gibbons, D. P. Le Heron, W. A. Morgan, and B. A. Pritchard, T.& Vining, eds., Microbial Carbonates in Space and Time: Implications for Global Exploration and Production.: London, The Geological Society of London, p. 209–219, doi:10.1144/SP418.3.

Wright, V Paul, and A. J. Barnett, 2015, An abiotic model for the development of textures in some South Atlantic early Cretaceous lacustrine carbonates: Geological Society, London, Special Publications, v. 418, no. 1, p. 209–219, doi:10.1144/SP418.3.

Wright, V. P., and A. J. Barnett, 2019, The textural evolution and ghost matrices of the Cretaceous Barra Velha Formation carbonates from the Santos Basin, offshore Brazil: Facies, v. 66, no. 1, p. 7, doi:10.1007/s10347-019-0591-2.

Zalán, P., K. Rodriguez, and M. Cvetkovic, 2019, Extraordinary Remaining Potential in the Pre-Salt of Santos Basin, *in* 16th International Congress of the Brazilian Geophysical Society: SBGf, p. 1–8, doi:10.22564/16cisbgf2019.128.

REFERÊNCIAS DE ACORDO COM AS NORMAS DE NORMALIZAÇÃO DE REFERÊNCIAS DA UNIVERSIDADE FEDERAL DO PARANÁ

Na página http://www.portal.ufpr.br/normalizacao estão disponíveis modelos de referências.

ALABI, G.; KASTEN, R.; CHITALE, V.; et al. THE VALUE OF PETROPHYSICAL MEASUREMENTS ACROSS MULTIPLE SCALES – A LACUSTRINE CARBONATE EXAMPLE FROM CAMPOS BASIN , BRAZIL. SPWLA 55th Annual Logging Symposium 2014. **Anais...** . p.12, 2014. Abu Dhabi, United Arab Emirates: Society of Petrophysicists and Well Log Analysts.

AMAEFULE, J. O.; ALTUNBAY, M.; TIAB, D.; KERSEY, D. G.; KEELAN, D. K. Enhanced reservoir description: using core and log data to identify hydraulic (flow) units and predict permeability in uncored intervals/ wells. **Proceedings - SPE Annual Technical Conference and Exhibition**, v. Omega, n. c, p. 205–220, 1993.

API. **Recommended practices for core analysis**. Washington, D.C: American Petroleum Institute, 1998.

BAOUCHE, R.; SEN, S.; GANGULI, S. S.; FERIEL, H. A. Petrophysical, geomechanical and depositional environment characterization of the Triassic TAGI reservoir from the Hassi Berkine South field, Berkine Basin, Southeastern Algeria. **Journal of Natural Gas Science and Engineering**, v. 92, n. April, p. 104002, 2021.

Elsevier B.V. Disponível em: <https://doi.org/10.1016/j.jngse.2021.104002>. . BARNETT, A. J.; WRIGHT, V. P.; CHANDRA, V. S.; JAIN, V. Distinguishing between eogenetic, unconformity-related and mesogenetic dissolution: A case study from the Panna and Mukta fields, offshore Mumbai, India. **Geological Society Special Publication**, v. 435, n. 1, p. 67–84, 2018.

BASSO, M.; BELILA, A. M. P.; CHINELATTO, G. F.; SOUZA, J. P. DA P.; VIDAL, A. C. Sedimentology and petrophysical analysis of pre-salt lacustrine carbonate reservoir from the Santos Basin, southeast Brazil. **International Journal of Earth Sciences**, v. 110, n. 7, p. 2573–2595, 2021. Springer Berlin Heidelberg. Disponível em: <https://doi.org/10.1007/s00531-020-01932-7>. .

BELILA, A. M. P.; BASSO, M.; CHINELATTO, G. F.; KURODA, M. C.; VIDAL, A. C. Pore typing using nuclear magnetic resonance, an example with samples from cretaceous pre-salt lacustrine carbonates in the Santos Basin, Brazil. **Journal of Petroleum Science and Engineering**, v. 190, n. February, p. 107079, 2020. Elsevier B.V. Disponível em: <https://doi.org/10.1016/j.petrol.2020.107079>. .

BIGELOW, E. L. Petrophysical and geological impact of borehole images. Society of Petroleum Engineers Western Regional Meeting. **Anais...** . p.345–354, 1993. Alaska.

BIZE-FOREST, N.; CENTENO, R.; BIZE, E.; et al. Vug porosity estimation using acoustic images in oil or water-based mud systems. EAGE Borehole Geology Workshop: Optimising the Use of Your Borehole Image Data. **Anais...** . p.3, 2014. Dubai, UAE.

BIZE-FOREST, N.; LAURA, L.; BAINES, V.; et al. Using Machine-Learning for Depositional Facies Prediction in a Complex Carbonate Reservoir. SPWLA 59th Annual Logging Symposium. **Anais...** . p.11, 2018. London: Society of Petrophysicists and Well Log Analysts. Disponível em: <https://onepetro.org/SPWLAALS/proceedings-abstract/SPWLA18/4-SPWLA18/D043S009R013/28806>. Acesso em: 20/6/2021.

BOYD, A.; SOUZA, A.; CARNEIRO, G.; et al. Presalt Carbonate Evaluation for Santos Basin, Offshore Brazil. **Petrophysics**, v. 56, n. 06, p. 577–591, 2015. BRELAZ, L.; RIBEIRO, M.; MENDES, I. Análise petrofísica dos reservatórios carbonáticos microbiais da Formação Barra Velha, Pré-sal da Bacia de Santos, Brasil. Proceedings of the 16th International Congress of the Brazilian Geophysical Society&Expogef. **Anais...** . p.1–6, 2019. Brazilian Geophysical Society. Disponível em: <https://sbgf.org.br/mysbgf/eventos/expanded_abstracts/16th_CISBGf/Análise petrofísica dos reservatórios carbonáticos microbiais da Formação Barra Velha, Pré-sal da Bacia de Santos, Brasil.pdf>. Acesso em: 28/5/2021.

CARMINATTI, M.; WOLFF, B.; GAMBOA, L. New Exploratory Frontiers In Brazil. 19th World Petroleum Congress. **Anais...** , 2008. Madrid, Spain: OnePetro. Disponível em: <https://onepetro.org/WPCONGRESS/proceedings/WPC19/All-WPC19/WPC-19-2802/172850>. .

CHANG, H. K.; KOWSMANN, R. O.; FIGUEIREDO, F. A. M.; BENDER, A. A. Tectonics and stratigraphy of the East Brazil Rift system: an overview. **Tectonophysics**, Geodynamics of Rifting, Volume II Case History Studies on Rifts: North and South America and Africa., v. 213, n. 1–2, p. 97–138, 1992. Disponível em: <https://www.sciencedirect.com/science/article/pii/0040195192902533>. .

CHITALE, V.; ALABI, G.; KASTEN, R.; TAYLOR, A.; HOENMANS, P. Learning from deployment of a variety of modern petrophysical formation evaluation technologies and techniques for characterization of a pre-salt carbonate reservoir: Case study from campos basin, brazil. **SPWLA 55th Annual Logging Symposium 2014**, 2014.

CHITALE, V. D. V; ALABI, G.; GRAMIN, P.; LEPLEY, S.; PICCOLI, L. Reservoir Characterization Challenges Due to the Multiscale Spatial Heterogeneity in the Presalt Carbonate Sag Formation, North Campos Basin, Brazil. **PETROPHYSICS**, v. 56, n. 6, p. 552–576, 2015.

COATES, G. R.; XIAO, L.; PRAMMER, M. G. **NMR Logging Principles and Applications**. Elsevier Science, 1999.

DAVIES, G. R.; SMITH, L. B. Structurally controlled hydrothermal dolomite reservoir facies: An overview. **AAPG Bulletin**, v. 90, n. 11, p. 1641–1690, 2006.

DEMŠAR, J.; CURK, T.; ERJAVEC, A.; et al. Orange: Data Mining Toolbox in Python. **Journal of Machine Learning Research**, v. 14, p. 2349–2353, 2013. Disponível em: <http://jmlr.org/papers/v14/demsar13a.html>. .

DOWSETT, M.; WIESINGER, R.; ADRIAENS, M. **Chapter 6 - X-ray diffraction**. Elsevier Inc., 2021.

DUNHAM, R. J. Classification of Carbonate Rocks According to Depositional Texture. **AAPG Symposium**, v. 1, p. 108–121, 1962. Disponível em: <https://scirp.org/reference/referencespapers.aspx?referenceid=1995622>. .

EHIGIE, S. O. NMR-openhole log integration: Making the most of NMR data deliverables. 34th Annual SPE International Conference and Exhibition held in Tinapa – Calabar, Nigeria. **Anais...** . v. 1, p.203–213, 2010.

ELLIS, D. V.; SINGER, J. M. **Well Logging for Earth Scientists**. 2º ed. Dordrecht: Springer Netherlands, 2007a.

ELLIS, D. V.; SINGER, J. M. Nuclear Magnetic Logging. **Well Logging for Earth Scientists**. p.415–478, 2007b. Springer Netherlands.

EMBRY, A. F.; KLOVAN, J. E. A LATE DEVONIAN REEF TRACT ON NORTHEASTERN BANKS ISLAND, N.W.T. **Bulletin of Canadian Petroleum Geology**, v. 19, n. 4, p. 730–781, 1971. GeoScienceWorld.

FAN, H.; SHI, J.; FAN, T.; et al. Sedimentary microfacies analysis of carbonate formation based on FMI and conventional logs: A case study from the ordovician in the Tahe Oilfield, Tarim Basin, China. **Journal of Petroleum Science and Engineering**, v. 203, n. March, p. 15, 2021.

FARIA, D. L. DE P.; TADEU DOS REIS, A.; GOMES DE SOUZA, O. Three-dimensional stratigraphic-sedimentological forward modeling of an Aptian carbonate reservoir deposited during the sag stage in the Santos basin, Brazil. **Marine and Petroleum Geology**, v. 88, p. 676–695, 2017. Elsevier Ltd. Disponível em: <https://doi.org/10.1016/j.marpetgeo.2017.09.013>. .

FARIAS, F.; SZATMARI, P.; BAHNIUK, A.; FRANÇA, A. B. Evaporitic carbonates in the pre-salt of Santos Basin – Genesis and tectonic implications. **Marine and Petroleum Geology**, v. 105, p. 251–272, 2019. Disponível em: <https://www.sciencedirect.com/science/article/pii/S0264817219301709>. .

GOMES, J. P.; BUNEVICH, R. B.; TEDESCHI, L. R.; TUCKER, M. E.; WHITAKER, F. F. Facies classification and patterns of lacustrine carbonate deposition of the Barra Velha Formation, Santos Basin, Brazilian Pre-salt. **Marine and Petroleum Geology**, v. 113, n. 104176, p. 21, 2020. Elsevier Ltd.

HAAGSMA, A.; SCHARENBERG, M.; KEISTER, L.; SCHUETTER, J.; GUPTA, N. Secondary porosity prediction in complex carbonate reefs using 3D CT scan image analysis and machine learning. **Journal of Petroleum Science and Engineering**, v. 207, n. October 2020, p. 18, 2021. Elsevier B.V. Disponível em: <https://doi.org/10.1016/j.petrol.2021.109087>. .

HASIUK, F. J.; KACZMAREK, S. E. SEM-Evidence of Biotic Influence in Brazilian Pre-Salt Carbonates. **AAPG Annual Conference and Exhibition**, v. 51190, p. 2015, 2015.

HEMENWAY, M. A.; KACZMAREK, S. E. High-resolution chemostratigraphy in carbonate mudstones: Salina A-1 carbonate (Silurian), Michigan Basin, U.S.A. **Marine and Petroleum Geology**, v. 126, n. 104918, p. 18, 2021. Elsevier Ltd. Disponível em: <https://doi.org/10.1016/j.marpetgeo.2021.104918>. .

HERLINGER, R.; DO NASCIMENTO FREITAS, G.; DOS ANJOS, C. D. W.; PETRÓLEO BRASILEIRO, S. A.; DE ROS, L. F. Petrological and petrophysical implications of magnesian clays in brazilian pre-salt deposits. SPWLA 61st Annual Logging Symposium. **Anais...** . p.13, 2020. Society of Petrophysicists and Well Log Analysts (SPWLA).

HERLINGER, R.; DOS SANTOS, B. C. C. The impact of pore type on NMR T2 and micp in bioclastic carbonate reservoirs. SPWLA 59th Annual Logging Symposium 2018. **Anais...** . p.10, 2018. London: Society of Petrophysicists and Well Log Analysts (SPWLA).

HERLINGER, R.; ZAMBONATO, E. E.; DE ROS, L. F. Influence of Diagenesis On the Quality of Lower Cretaceous Pre-salt Lacustrine Carbonate Reservoirs from Northern Campos Basin, Offshore Brazil. **Journal of Sedimentary Research**, v. 87, n. 12, p. 1285–1313, 2017. Disponível em: <https://pubs.geoscienceworld.org/sepm/jsedres/article-abstract/87/12/1285/525035/Influence-of-Diagenesis-On-the-Quality-of-Lower>. .

JENKINS, R.; SNYDER, R. **Introduction to X-Ray Powder Diffractometry.** Wiley-Interscience, 2012.

KOREN, Y.; CARMEL, L. Visualization of labeled data using linear transformations. **Proceedings - IEEE Symposium on Information Visualization, INFO VIS**, p. 121–130, 2003.

LAI, J.; PANG, X.; XIAO, Q.; et al. Prediction of reservoir quality in carbonates via porosity spectrum from image logs. **Journal of Petroleum Science and Engineering**, v. 173, p. 197–208, 2019. Elsevier B.V. Disponível em: <https://doi.org/10.1016/j.petrol.2018.10.022>. .

LAI, J.; WANG, G.; FAN, Z.; et al. Fracture detection in oil-based drilling mud using a combination of borehole image and sonic logs. **Marine and Petroleum Geology**, v. 84, p. 195–214, 2017. Elsevier Ltd. Disponível em: <https://doi.org/10.1016/j.marpetgeo.2017.03.035>. .

LAI, J.; WANG, G.; WANG, S.; et al. A review on the applications of image logs in structural analysis and sedimentary characterization. **Marine and Petroleum Geology**, v. 95, n. May, p. 139–166, 2018. Elsevier. Disponível em: <https://doi.org/10.1016/j.marpetgeo.2018.04.020>. .

LI, J.; WANG, Y.; LIU, C.; DONG, D.; GAO, Z. Hydrothermal fluid activity and the quantitative evaluation of its impact on carbonate reservoirs: A case study of the Lower Paleozoic in the west of Dongying sag, Bohai Bay Basin. **Petroleum Exploration and Development**, v. 43, n. 3, p. 395–403, 2016. Disponível em: <https://linkinghub.elsevier.com/retrieve/pii/S1876380416300465>. .

LI, Q.; YOU, X.; JIANG, Z.; WU, S.; ZHANG, R. Lithofacies and reservoir characterization of a source-controlled carbonate succession in a lacustrine rift basin, the Shulu Sag of Bohai Bay Basin, East China. **Journal of Petroleum Science and Engineering**, v. 192, n. September 2019, p. 107180, 2020. Elsevier B.V. Disponível em: <https://doi.org/10.1016/j.petrol.2020.107180>. .

LIMA, B. E. M.; DE ROS, L. F. Deposition, diagenetic and hydrothermal processes in the Aptian Pre-Salt lacustrine carbonate reservoirs of the northern Campos Basin, offshore Brazil. **Sedimentary Geology**, v. 383, p. 55–81, 2019. Disponível em: <https://www.sciencedirect.com/science/article/pii/S0037073819300156>. .

LIMA, B. E. M.; TEDESCHI, L. R.; PESTILHO, A. L. S.; et al. Deep-burial hydrothermal alteration of the Pre-Salt carbonate reservoirs from northern Campos Basin, offshore Brazil: Evidence from petrography, fluid inclusions, Sr, C and O isotopes. **Marine and Petroleum Geology**, v. 113, n. 104143, p. 25, 2020. Disponível em:
<https://www.sciencedirect.com/science/article/pii/S0264817219305951>. .

MADRUCCI, V.; SPADINI, A. R.; ANJOS, C. W. D. DOS; ALVES, D. B.; ANJOS, S. M. C. DOS. Authigenic Magnesian Clays in Carbonate Reservoirs in Brazil. International Meeting of Carbonate Sedimentologists. **Anais...** . p.1, 2013. Bathurst Meeting Mallorca.

MAKEEN, Y. M.; SHAN, X.; AYINLA, H. A.; et al. Sedimentology, petrography, and reservoir quality of the Zarga and Ghazal formations in the Keyi oilfield, Muglad Basin, Sudan. **Scientific Reports**, v. 11, n. 1, p. 1–22, 2021. Nature Publishing Group UK. Disponível em: <https://doi.org/10.1038/s41598-020-80831-y>. .

MENEZES, C. P.; BEZERRA, F. H. R.; BALSAMO, F.; et al. Hydrothermal silicification along faults affecting carbonate-sandstone units and its impact on reservoir quality, Potiguar Basin, Brazil. **Marine and Petroleum Geology**, v. 110, p. 198–217, 2019. Elsevier.

MERCEDES-MARTÍN, R.; AYORA, C.; TRITLLA, J.; SÁNCHEZ-ROMÁN, M. The hydrochemical evolution of alkaline volcanic lakes: a model to understand the South Atlantic Pre-salt mineral assemblages. **Earth-Science Reviews**, v. 198, p. 102938, 2019. Disponível em:
<https://www.sciencedirect.com/science/article/pii/S0012825218307414>. .

MOHRIAK, W. U.; PERDOMO, L. V.; PLUCENIO, D. M.; SAAD, J. L. Challenges for petrophysical characterization of presalt carbonate reservoirs. 14th International Congress of the Brazilian Geophysical Society. **Anais...** . p.623–627, 2015. Rio de Janeiro, RJ: SBGf.

MOREIRA, J. L. P.; MADEIRA, C. V; GIL, J. A.; MACHADO, M. A. P. Santos basin. **Boletim de Geociencias da Petrobras**, v. 15, n. 2, p. 531–549, 2007. Disponível em: <http://files/196/display.html>. .

MUNIZ, M. C.; BOSENCE, D. W. J. Pre-salt microbialites from the Campos Basin (offshore Brazil): image log facies, facies model and cyclicity in lacustrine carbonates. In: D. W. J. Bosence; K. A. Gibbons; D. P. Le Heron; W. A. Morgan; B. A. Pritchard, T.& Vining (Orgs.); **Microbial Carbonates in Space and Time: Implications for Global Exploration and Production.**, 2015. London: Geological Society, London, Special Publications. Disponível em: <https://pubs.geoscienceworld.orghttps//pubs.geoscienceworld.org/books/book/1789/chapter/107690175/Pre-salt-microbialites-from-the-Campos-Basin>. .

MUNIZ, M. C.; BOSENCE, D. W. J. Lacustrine carbonate platforms: Facies, cycles, and tectonosedimentary models for the presalt Lagoa Feia Group (Lower Cretaceous), Campos Basin, Brazil. **AAPG Bulletin**, v. 102, n. 12, p. 2569–2597, 2018. Disponível em: <https://pubs.geoscienceworld.org/aapgbull/article-abstract/102/12/2569/566695/Lacustrine-carbonate-platforms-Facies-cycles-and>. .

PEDREGOSA, F.; VAROQUAUX, G.; GRAMFORT, A.; et al. Scikit-learn: Machine Learning in Python. **Journal of Machine Learning Research**, v. 12, p. 2825–2830, 2011.

PENNA, R.; LUPINACCI, W. M. Decameter-scale flow-unit classification in Brazilian presalt carbonates. **SPE Reservoir Evaluation and Engineering**, v. 23, n. 4, p. 1420–1439, 2020.

PETERSOHN, E.; ABELHA, M. Libra Geological assessment report. Disponível em: <https://www.gov.br/anp/pt-br/rodadas-anp/rodadas-concluidas/partilha-de-producao/1a-rodada-partilha-producao-pre-sal/arquivos/seminarios/partilha1_tecnico_ambiental_ingles.pdf/view>. Acesso em: 12/10/2021.

PIETZSCH, R.; OLIVEIRA, D. M.; TEDESCHI, L. R.; et al. Palaeohydrology of the Lower Cretaceous pre-salt lacustrine system, from rift to post-rift phase, Santos Basin, Brazil. **Palaeogeography, Palaeoclimatology, Palaeoecology**, v. 507, p. 60–80, 2018. Disponível em: <https://www.sciencedirect.com/science/article/pii/S0031018218300142>. .

PIETZSCH, R.; TEDESCHI, L. R.; OLIVEIRA, D. M.; et al. Environmental conditions of deposition of the Lower Cretaceous lacustrine carbonates of the Barra Velha Formation, Santos Basin (Brazil), based on stable carbon and oxygen isotopes: A continental record of pCO2 during the onset of the Oceanic Anoxic Event. **Chemical Geology**, v. 535, p. 119457, 2020. Disponível em: <https://www.sciencedirect.com/science/article/pii/S0009254119305868>. .

RADWAN, A. A.; NABAWY, B. S.; ABDELMAKSOUD, A.; LASHIN, A. Integrated sedimentological and petrophysical characterization for clastic reservoirs: A case study from New Zealand. **Journal of Natural Gas Science and Engineering**, v. 88, n. 103797, p. 25, 2021. Elsevier B.V. Disponível em: <https://doi.org/10.1016/j.jngse.2021.103797>. .

REZENDE, M. F.; POPE, M. C. Importance of depositional texture in pore characterization of subsalt microbialite carbonates, offshore Brazil. **Geological Society Special Publication**, v. 418, n. 1, p. 193–207, 2015.

RIDER, M. H. **Geological Interpretation of Well Logs**. 3rd Revise ed. Sutherland: Rider-French Consulting Limite, 2011.

RIOS, E. H.; RAMOS, P. F. DE O.; COMPAN, A. L. M.; et al. Petrofísica laboratorial no suporte à exploração e caracterização de reservatórios. , p. cp-341-00098, 2012. European Association of Geoscientists & Engineers. Disponível em: <https://www.earthdoc.org/content/papers/10.3997/2214-4609-pdb.341.99>. Acesso em: 21/5/2021.

SABATO CERALDI, TERESA; GREEN, D. Evolution of the South Atlantic lacustrine deposits in response to Early Cretaceous rifting, subsidence and lake hydrology. In: T. Sabato Ceraldi; R. A. Hodgkinson; G. Backe (Orgs.); **Petroleum Geoscience of the West Africa Margin.** v. 438, p.77–98, 2017. The Geological Society of London. SALLER, A.; RUSHTON, S.; BUAMBUA, L.; et al. Presalt stratigraphy and depositional systems in the Kwanza Basin, offshore Angola. **AAPG Bulletin**, v. 100, n. 07, p. 1135–1164, 2016. American Association of Petroleum Geologists. Disponível em: <http://archives.datapages.com/data/bulletns/2016/07jul/BLTN15216/bltn15216.html >. Acesso em: 20/5/2021.

SCHÖN, J. H. Pore Space Properties. . p.21–84, 2015. Disponível em: <https://linkinghub.elsevier.com/retrieve/pii/B9780081004043000020>. .

SOUZA, R. S.; ARIENTI, L. M.; VIANA, S. M.; et al. Petrology of the Hydrothermal and Evaporitic Continental Cretaceous (Aptian) Pre-Salt Carbonates and Associated Rocks, South Atlantic Santos Basin, Offshore Brazil. , 2018. Salt Lake City, Utah,: AAPG ACE. Disponível em: <https://www.searchanddiscovery.com/abstracts/html/2018/ace2018/abstracts/28356 91.html>. .

TEBOUL, P.-A.; KLUSKA, J.-M.; MARTY, N. C. M.; et al. Volcanic rock alterations of the Kwanza Basin, offshore Angola - Insights from an integrated petrological, geochemical and numerical approach. **Marine and Petroleum Geology**, v. 80, p.

394–411, 2016. Elsevier Ltd. Disponível em:
<https://linkinghub.elsevier.com/retrieve/pii/S0264817216304494>. Acesso em:
20/5/2021.

TERRA, G. G. S.; SPADINI, A. R.; FRANCA, A. B.; et al. Classificação de rochas
carbonáticas aplicável às bacias sedimentares brasileiras. **Boletim de Geociencias
da Petrobras**, v. 18, p. 9–29, 2010.

TIAB, D.; DONALDSON, E. C. Porosity and Permeability. **Petrophysics**. p.67–186,
2016. Elsevier. Disponível em:
<https://linkinghub.elsevier.com/retrieve/pii/B9780128031889000036>. .

TOSCA, N. J.; WRIGHT, V. P. Diagenetic pathways linked to labile Mg-clays in
lacustrine carbonate reservoirs: A model for the origin of secondary porosity in the
Cretaceous pre-salt Barra Velha Formation, offshore Brazil. In: P. J. Armitage; A. R.
Butcher; J. M. Churchill; et al. (Orgs.); **Reservoir Quality of Clastic and Carbonate
Rocks: Analysis, Modelling and Prediction.** v. 435, p.33–46, 2015. London: The
Geological Society of London.

VALLE, B.; DAL' BÓ, P. F.; SANTOS, J.; et al. A new method to improve the NMR
log interpretation in drilling mud-invaded zones: A case study from the Brazilian Pre-
salt. **Journal of Petroleum Science and Engineering**, v. 203, n. 108692, p. 14,
2021. Disponível em:
<https://www.sciencedirect.com/science/article/pii/S0920410521003521>. .

VIERA DE LUCA, P. H.; MATIAS, H.; CARBALLO, J.; et al. Breaking barriers and
paradigms in presalt exploration: The pão de açúcar discovery (Offshore Brazil). In:
R. K. Merrill; C. A. Sternbach (Orgs.); **Giant fields of the decade 2000–2010: AAPG
Memoir 113**. v. 113, p.177–193, 2017. The American Association of Petroleum
Geologists.

WILLIAMS, P. D.; MADDOCK, R. H.; SAPRU, A. K.; LAWRENCE, M. J. F. Analysis
of a fractured carbonate reservoir (thamama group) using borehole images from an
horizontal well, offshore UAE. **Society of Petroleum Engineers - Abu Dhabi
International Petroleum Exhibition and Conference 2000, ADIPEC 2000**, v. 1, n.
iii, p. 1–9, 2000.

WORDEN, R. H.; ARMITAGE, P. J.; BUTCHER, A. R.; et al. Petroleum reservoir
quality prediction: Overview and contrasting approaches from sandstone and
carbonate communities. In: R. H. Armitage, P. J., Butcher, A. R., Churchill, J. M.,
Csoma, A. E., Hollis, C., Lander, R. H., Omma,J.E.& Worden (Org.); **Geological
Society Special Publication**. v. 435, p.1–31, 2018. London: The Geological Society
of London.

WRIGHT, V. P. The mantle, CO 2 and the giant Aptian chemogenic lacustrine carbonate factory of the South Atlantic: Some carbonates are made, not born. (J. I. Baceta, Org.)**Sedimentology**, p. 27, 2020. Disponível em: <https://onlinelibrary.wiley.com/doi/10.1111/sed.12835>. .

WRIGHT, V. PAUL; BARNETT, A. J. An abiotic model for the development of textures in some South Atlantic early Cretaceous lacustrine carbonates. In: D. W. J. Bosence; K. A. Gibbons; D. P. Le Heron; W. A. Morgan; B. A. Pritchard, T.& Vining (Orgs.); **Microbial Carbonates in Space and Time: Implications for Global Exploration and Production.** v. 418, p.209–219, 2015. London: The Geological Society of London.

WRIGHT, V PAUL; BARNETT, A. J. An abiotic model for the development of textures in some South Atlantic early Cretaceous lacustrine carbonates. **Geological Society, London, Special Publications**, v. 418, n. 1, p. 209–219, 2015. Disponível em: <https://pubs.geoscienceworld.orghttps//pubs.geoscienceworld.org/books/book/1789/ chapter/107689738/An-abiotic-model-for-the-development-of-textures>. .

WRIGHT, V. P.; BARNETT, A. J. The textural evolution and ghost matrices of the Cretaceous Barra Velha Formation carbonates from the Santos Basin, offshore Brazil. **Facies**, v. 66, n. 1, p. 7, 2019. Disponível em: <https://doi.org/10.1007/s10347-019-0591-2>. .

ZALÁN, P.; RODRIGUEZ, K.; CVETKOVIC, M. Extraordinary Remaining Potential in the Pre-Salt of Santos Basin. 16th International Congress of the Brazilian Geophysical Society. **Anais...** . p.1–8, 2019. Rio de Janeiro, RJ: SBGf.

ANEXO 1 – CLASSIFICAÇÃO DE ROCHAS CARBONÁTICAS

FIGURA 30 – CLASSIFICAÇÃO DE ROCHAS CARBONÁTICAS DE DUNHAM (1962).

FONTE: (Terra et al., 2010).

FIGURA 31 – CLASSIFICAÇÃO DE ROCHAS CARBONÁTICAS DE EMBRY & KLOVAN (1971).


FONTE: (Terra et al., 2010).

FIGURA 32 – CLASSIFICAÇÃO DE ROCHAS CARBONÁTICAS TERRA *et al*. (2010).

Classificação de Rochas Carbonáticas Aplicável às Bacias Sedimentares Brasileiras

NOMENCLATURA PRINCIPAL	TEXTURA	DEFINIÇÃO	NOMENCLATURA COMPLEMENTAR	REFERÊNCIA OU MODIFICADO DE	TERMOS CORRELATOS	TEXTURAS MODIFICADORAS	TAMANHO MÉDIO DOS ELEMENTOS EM CORTE VERTICAL E EMPACOTAMENTO	FORMA EXTERNA (escala de testemunhos)
MUDSTONE		Rocha suportada pela matriz com **menos** de 10% de grãos (tamanho areia ou maior).	COM (Caso ocorram grãos) oolitos, oncolitos, pelóides, peloides fecais, intraclastos, bioclastos, esferulitos ou **CALCILUTITO A BIRDSEYES**= rocha suportada pela matriz com porosidade fenestral ou lentes de calcita espática.	Dunham (1962)	Calcilutito, Dismicrito, mudstone a birdseyes.	C/ feições de exposição; Com feições pedogenéticas; Bioturbado; Dolomitizado; Silicificado, Com *Hardgrounds*; etc.		
WACKESTONE		Rocha suportada pela matriz com **mais** de 10% de grãos (tamanho areia ou maior).	COM (para os grãos) - oolitos, oncolitos, pelóides, peloides fecais, intraclastos, bioclastos, esferulitos.	Dunham (1962)				
PACKSTONE		Rocha suportada pelos grãos com matriz.	"+" (composição principal): oolítico, oncolítico, peloidal, peloidal fecal, intraclástico, bioclástico, esferulítico; com fragmentos de estromatolitos, trombolitos, laminitos, leiolito, dendrolito.	Dunham (1962)	Calcarenito, oomicrito, biomicrito, pelmicrito, intramicrito.			
GRAINSTONE		Rocha suportada pelos grãos, sem matriz (< 5% de matriz).	"+" (composição principal): oolítico, oncolítico, peloidal, peloidal fecal, intraclástico, bioclástico, esferulítico; com fragmentos de estromatolitos, trombolitos, laminitos, leiolito, dendrolito.	Dunham (1962)	Calcarenito, ooespatito, pelespatito, intraespatito			
FLOATSTONE		Rocha suportada pela matriz com mais de 10% dos grãos maiores que 2 mm	COM (para os grãos) - oolitos, oncolitos, pelóides, peloides fecais, intraclastos, bioclastos, esferulitos. Com fragmentos de estromatolitos, trombolitos, laminitos, leiolito, dendrolito.	Embry&Klowan (1971)				
RUDSTONE		Rocha suportada pelos grãos com mais de 10% dos grãos maiores que 2 mm.	"+" (composição principal): oolítico, oncolítico, peloidal, peloidal fecal, intraclástico, bioclástico, esferulítico; com fragmentos de estromatolito, trombolito, laminito, leiolito, dendrolito, esferulitito.	Embry e Klowan (1971)	Brecha			
BIOACUMULADO		Rocha constituída pela dominância de um tipo de organismo sem retrabalhamento (*in situ*) e granulometria areia ou maior.	"+" organismo formador: ex. ostracodes, bivalvos, macroforaminíferos, crinóides, etc...	Carozzi (1972)	Coquina			
BRECHA		Rocha suportada pelos grãos com mais de 50% dos grãos angulosos maiores que 2 mm.	"+" (composição principal): intraclástica; com fragmentos de estromatolito, trombolito, laminito, leiolito, dendrolito, esferulitito.	Flügel (2004); Pettijohn (1974)	Brecha de Colapso, Breccia, Rudstone com clastos angulosos			
BOUNDSTONE		Rocha formada *in situ* cujos componentes da trama original (fábrica original) foram ligados durante a deposição.	"+" principais organismos formadores: ex. coralgal, a rudistas, a estromatoporóides, etc..	Dunham (1962)	Biolitito, Bafflestone, Bindstone, Framestone.	C/ feições de exposição; C/ feições pedogenéticas; Bioturbado; Dolomitizado, Silicificado, etc		
ESTROMATOLITO Depósito de estrutura laminada e, em geral, convexa, podendo apresentar feições de crescimento/ramificações internas para o topo. Na maioria das vezes de origem microbial Pode ser observado em diferentes escalas.		ESTROMATOLITO					Muito pequeno: < 0,2 cm; Pequeno: 0,2-0,5 cm; Médio: 0,51-1,5 cm; Grande= 1,5 cm; Denso: todos os elementos se tocam; Normal: alguns elementos se tocam; Aberto: raros ou nenhum dos elementos se tocam	Finamente laminado; Levente dômico; Dômico; Tabular; Colunar; Conforme
		ESTROMATOLITO ARBORESCENTE - os componentes internos se organizam de forma ramificada divergente e possuem comprimento maior que a largura.		Riding (2000)		Mosqueado (*mottled*) Bioturbado; C/ feições de Exposição; C/ feições pedogenéticas; Dolomitizado; Silicificado, etc		
		ESTROMATOLITO ARBUSTIFORME – os componentes internos se ramificam ou não desde a base e a razão altura/largura é aproximadamente 1:1.						
		ESTROMATOLITO DENDRIFORME - os componentes internos se organizam de forma intensamente ramificada divergente em que o comprimento é muito maior que a largura.						
TROMBOLITO		Depósito com textura macroscópica **coagulada (clotted)**, maciça e dômica. Na maioria das vezes de origem microbial.						Levente dômico, Dômico, Colunar
DENDROLITO		Depósito microbial de estrutura dendrítica formada por cianobactérias esqueletais.						Levente dômico, Dômico
LEIOLITO		Carbonato microbial dômico, sem laminação ou coágulos.						Levente dômico, Dômico
ESFERULITITO		Rocha composta por partículas de formas esféricas ou subesféricas com contornos lisos ou lobados (esferulitos) de tamanho geralmente inferior a 2 mm e que podem ocorrer de forma amalgamada ou isolados.	Esferulito-suportado com argila (>10%)= ESFERULITITO COM ARGILA; Argila-suportado, com esferulitos= ARGILITO COM ESFERULITOS; No caso da argila ocorrer em lamelas= ARGILITO LAMELAR COM ESFERULITOS	Este trabalho				
TRAVERTINO & (TUFA)		Rocha carbonática bandeada formada pela precipitação em superfície de soluções concentradas em $CaCO_3$ ao redor de fontes (em geral quentes) devido a perda de CO_2 por evaporação. A variedade mais esponjosa e menos compacta é denominada **TUFA**.		Riding (2000); Pettijohn (1957)				
LAMINITO		Rocha carbonática de granulação fina (lamosa e/ou peloidal) formada pela recorrência de laminações delgadas. As laminações tendem a ser plano-paralelas, com superfície lisa (origem microbial ou não) ou crenulada (origem microbial).	LISO / CRENULADO	Demicco (1994)	Esteira, esteira microbial, tapete microbial, esteira algal, laminito microbial, biolaminito			
CALCÁRIO CRISTALINO		Rocha carbonática totalmente recristalizada não sendo possível identificar sua textura original (deposicional). CALCÁRIO MICROCRISTALINO: cristais entre 5 e 50 µm		Folk (1962); Dunham (1962)	Espatito, Microespatito			
DOLOMITO		Rocha carbonática totalmente dolomitizada não sendo possível identificar sua textura original (deposicional). MICRODOLOMITO: cristais entre 5 e 50 µm			Doloespatito, Microdoloespatito			

Elementos não ligados durante a formação — *Elementos ligados durante a formação - in situ* — *Elementos ligados ou não* — *Textura original não reconhecível*

FONTE: (Terra et al., 2010).

ANEXO 2 – RCAL MEASUREMENTS BOX PLOT

FIGURE 33 – RCAL MEASUREMENTS FOR GRAIN SIZE, POROSITY, AND PERMEABITY USING SIDE-WALL CORES, IN WELLS LOCATED AT THE STRUCTURAL HIGH
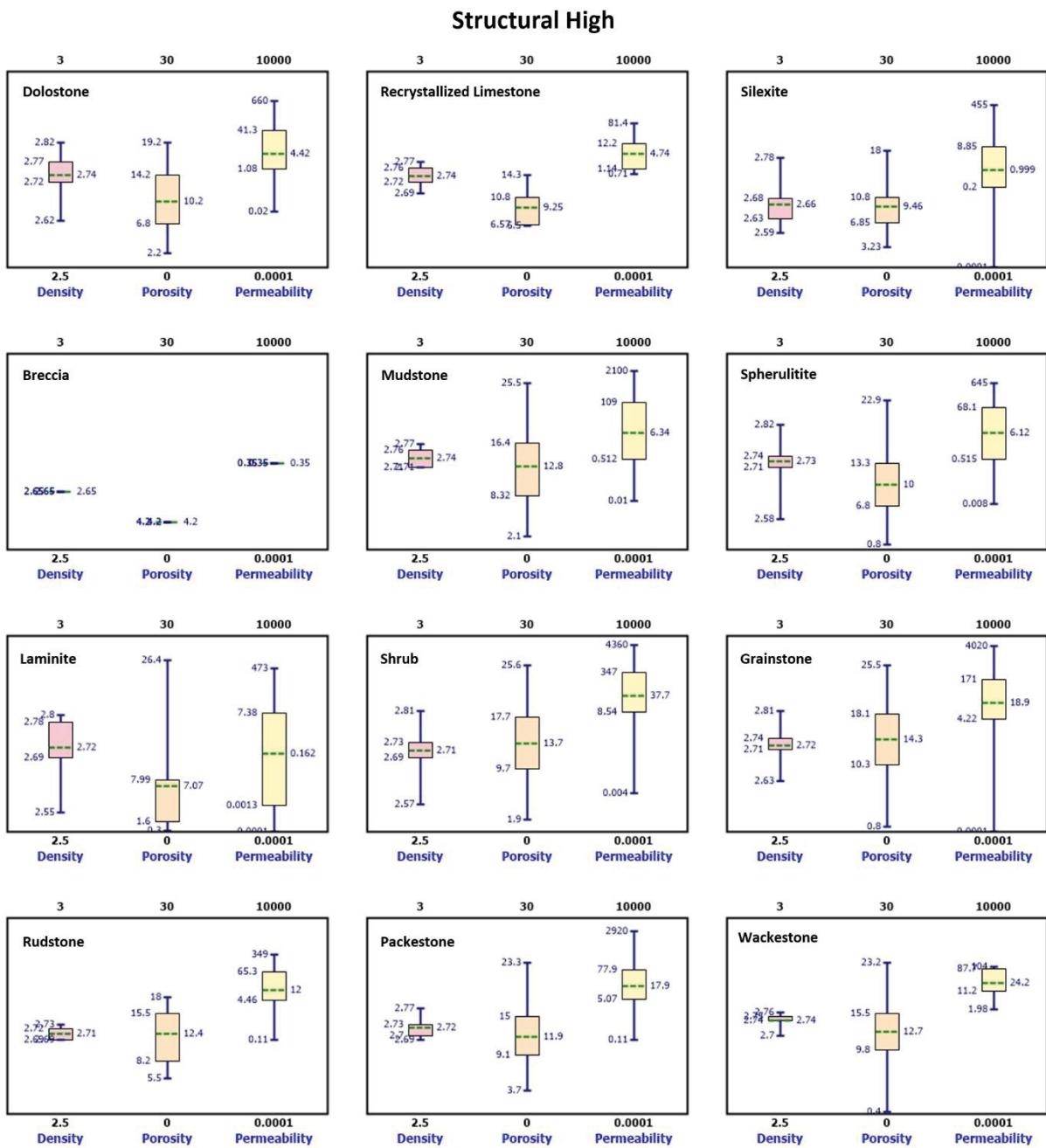

Source: The author (2022).

FIGURE 34 – RCAL MEASUREMENTS FOR GRAIN SIZE, POROSITY, AND PERMEABITY USING SIDE-WALL CORES, IN THE WELLS LOCATED AT THE BASINWARD AREA
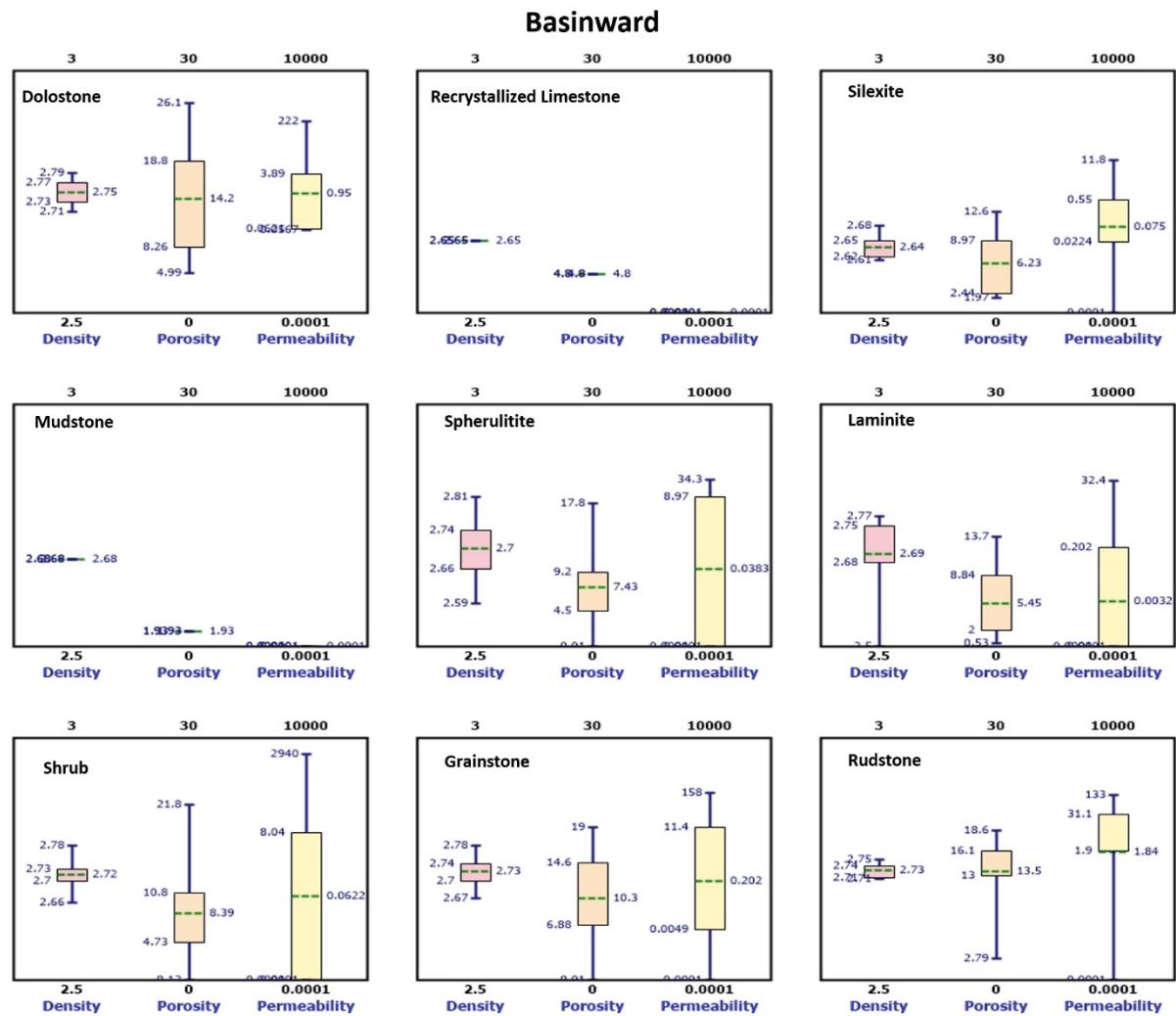

Source: The author (2022).

ANEXO 3 – PC1-PC2 RESULTS, SUPPLEMENTARY PLOTS

FIGURE 35 – PC1-PC2 SCATTER PLOT FOR MATRIX–SUPPORTED SAMPLES
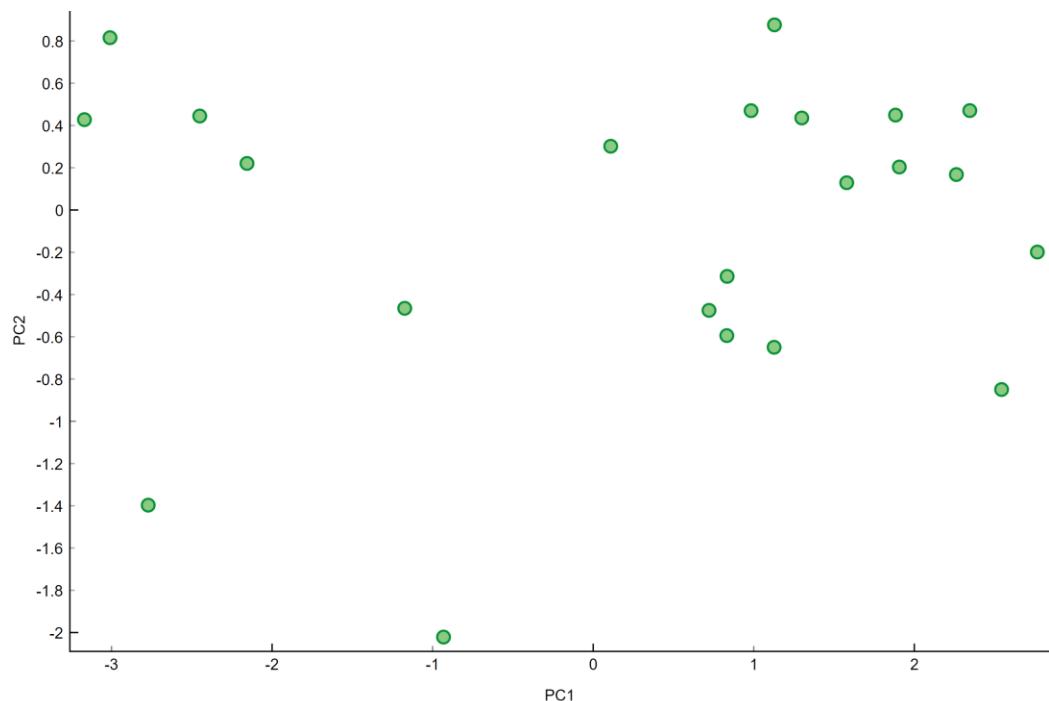
Source: The Author (2022).

FIGURE 36 – PC1-PC2 SCATTER PLOT FOR SPHERULITITE SAMPLES
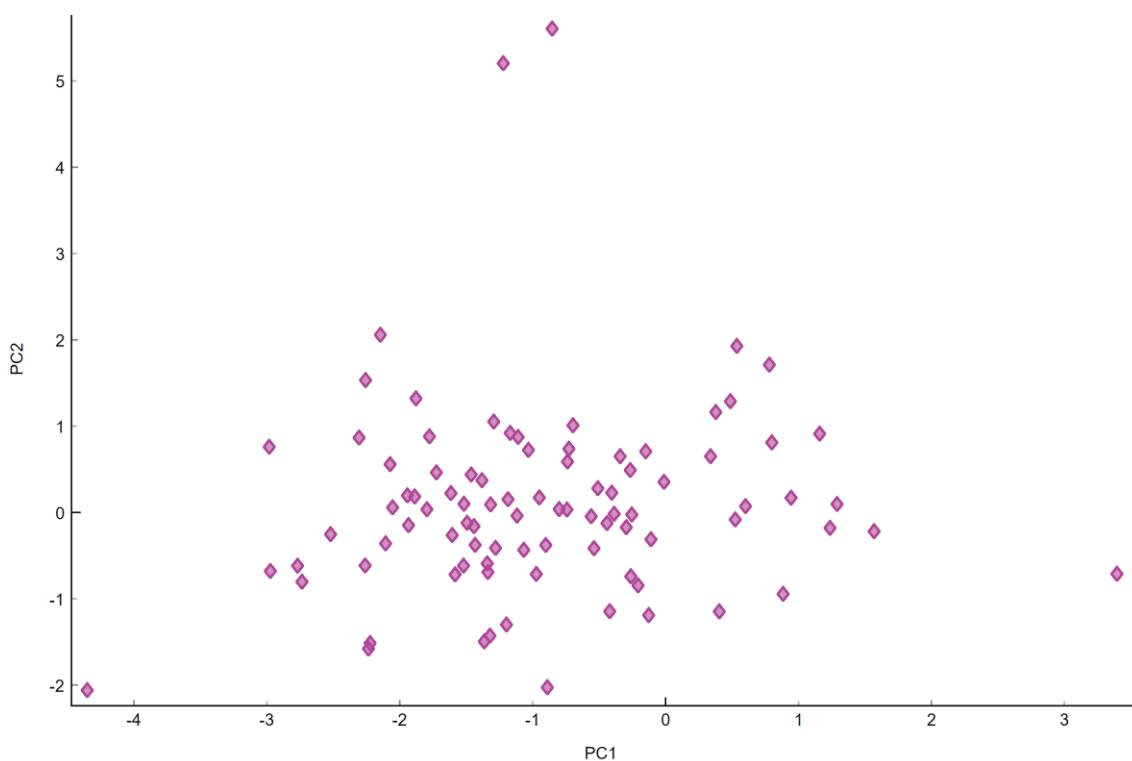
Source: The Author (2022).

FIGURE 37 – PC1-PC2 SCATTER PLOT FOR SHRUB SAMPLES
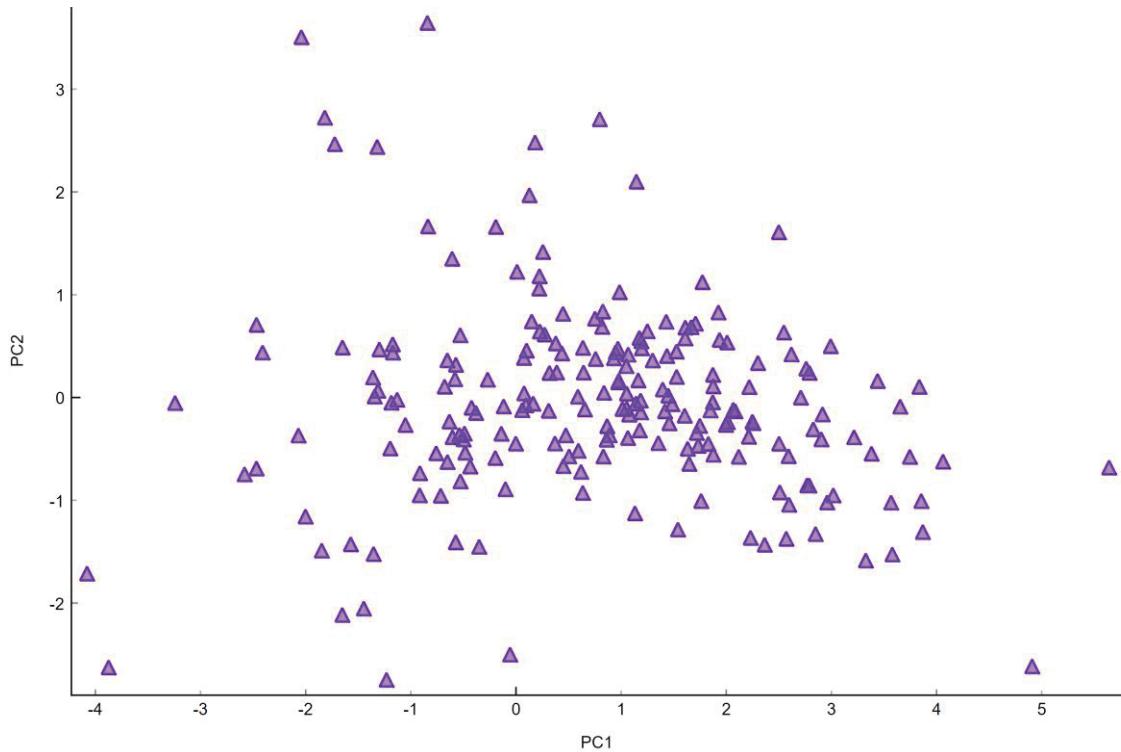

Source: The Author (2022).

FIGURE 38 – PC1-PC2 SCATTER PLOT FOR GRAIN–SUPPORTED SAMPLES
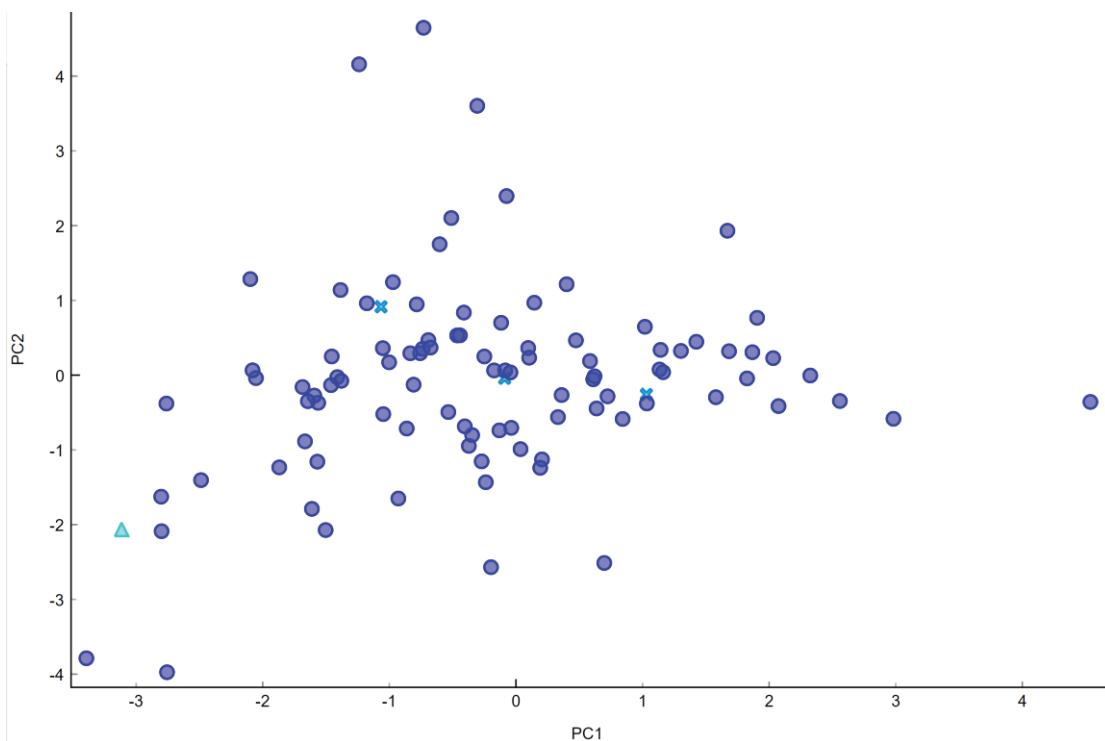
Source: The Author (2022).

FIGURE 39 – PC1-PC2 SCATTER PLOT FOR DOLOSTONE, SILEXITES, AND RECRYSTALIZED LIMESTONE SAMPLES
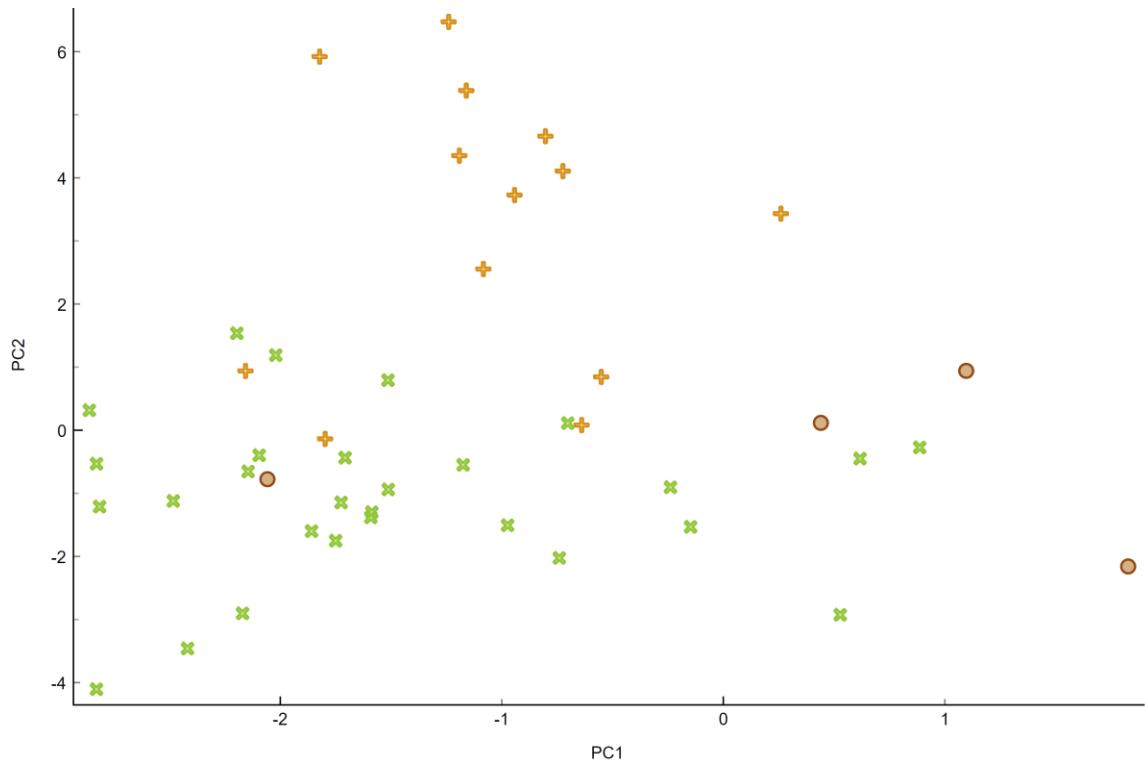

Source: The Author (2022).

ANEXO 4 – LINEAR PROJECTION PCA, ADDITIONAL PLOT

FIGURE 40 – LINEAR PROJECTION ADDITIONAL PLOT CONSIDERING ALL SAMPLES, WITHOUT LABELLING THE FACIES.
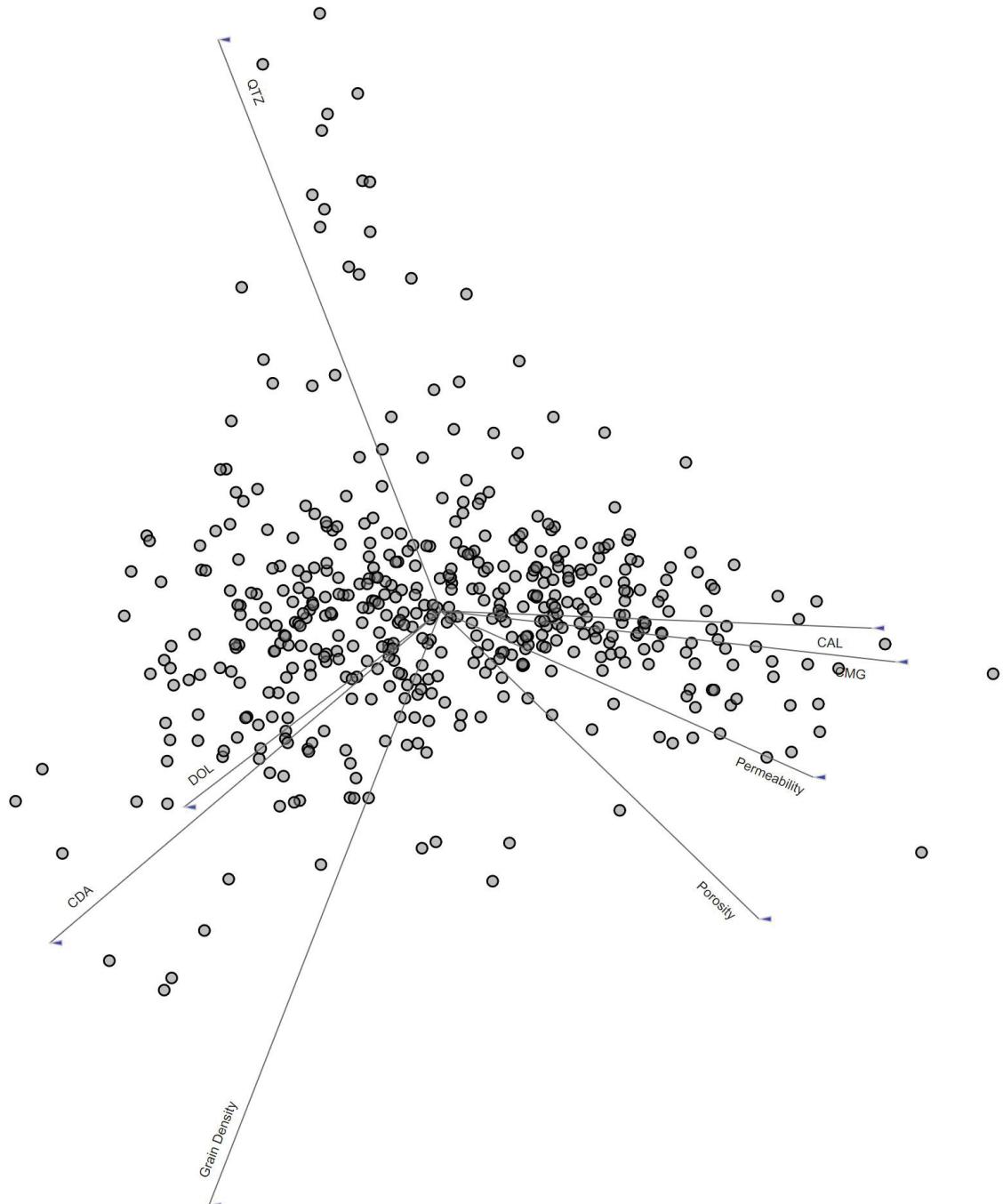
Source: The author (2022).

# ANEXO 5 – TERNARY-PLOT, SUPPLEMENTARY PLOTS

FIGURE 41 – THE X–RAY DIFFRACTION TERNARY PLOT DIFFERENTIATING CARBONATES FACIES, SUPPLEMENTARY PLOT
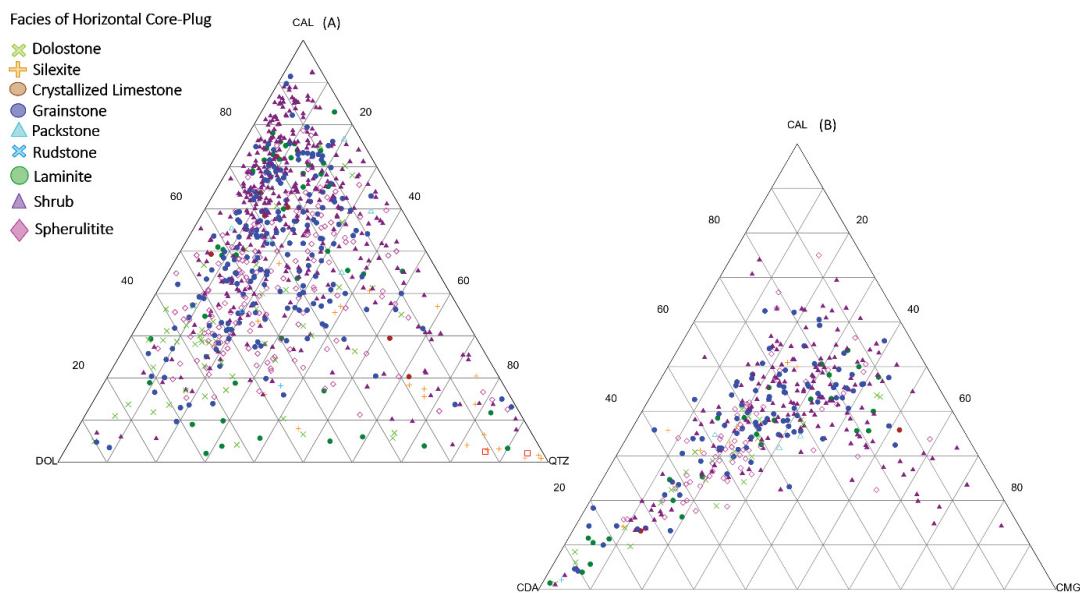
Source: The author (2022).

Caption: (A) Calcite–Dolomite–Quartz; (B) Calcite–Ca–Dolomite/Ankerite–Mg–Calcite.

FIGURE 42 – THE X–RAY DIFFRACTION TERNARY PLOT, CALCITE-DOLOMITE-QUARTZ, DIFFERENTIATING CARBONATES FACIES, SUPPLEMENTARY PLOT
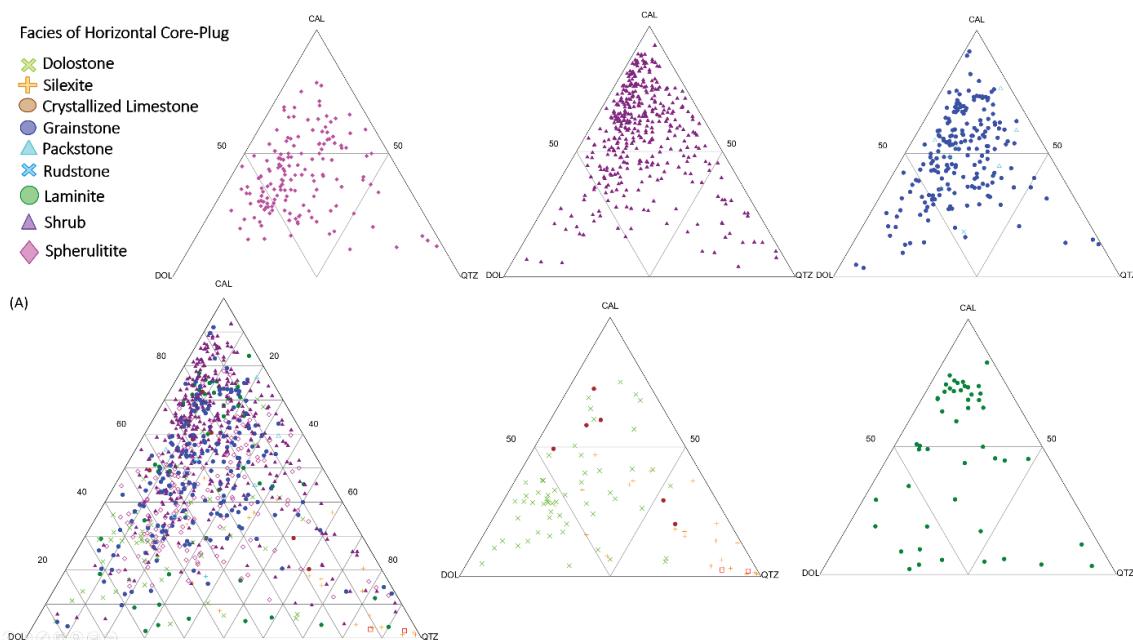
Source: The author (2022).

Caption: (A) Calcite–Dolomite–Quartz.

FIGURE 43 – THE X–RAY DIFFRACTION TERNARY PLOT, CALCITE–CA–DOLOMITE/ANKERITE–
MG–CALCITE, DIFFERENTIATING CARBONATES FACIES, SUPPLEMENTARY PLOT
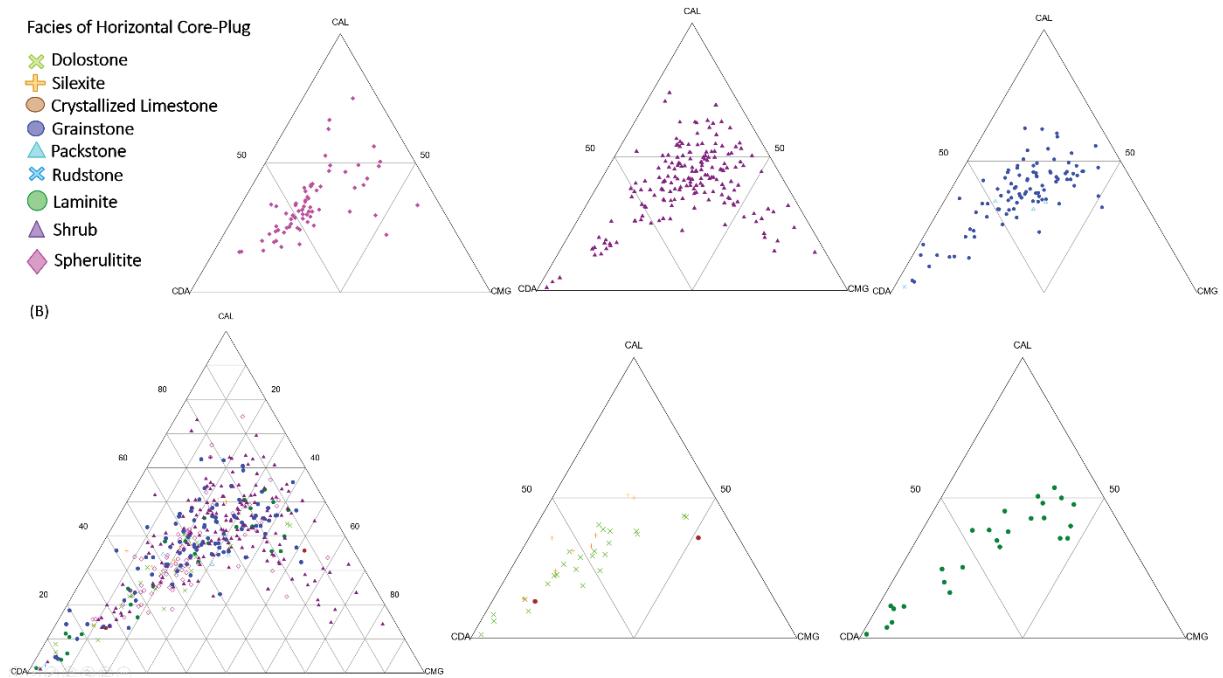
Source: The author (2022).

Caption: (B) Calcite–Ca–Dolomite/Ankerite–Mg–Calcite.